1992

An Investigation Of Protein Crystal Growth By Laser Light Scattering.

John Bradford Bishop
University of Alabama at Birmingham

Recommended Citation

Bishop, John Bradford, "An Investigation Of Protein Crystal Growth By Laser Light Scattering." (1992). *All ETDs from UAB*. 4531.
https://digitalcommons.library.uab.edu/etd-collection/4531

INFORMATION TO USERS

This manuscript has been reproduced from the microfilm master. UMI films the text directly from the original or copy submitted. Thus, some thesis and dissertation copies are in typewriter face, while others may be from any type of computer printer.

The quality of this reproduction is dependent upon the quality of the copy submitted. Broken or indistinct print, colored or poor quality illustrations and photographs, print bleedthrough, substandard margins, and improper alignment can adversely affect reproduction.

In the unlikely event that the author did not send UMI a complete manuscript and there are missing pages, these will be noted. Also, if unauthorized copyright material had to be removed, a note will indicate the deletion.

Oversize materials (e.g., maps, drawings, charts) are reproduced by sectioning the original, beginning at the upper left-hand corner and continuing from left to right in equal sections with small overlaps. Each original is also photographed in one exposure and is included in reduced form at the back of the book.

Photographs included in the original manuscript have been reproduced xerographically in this copy. Higher quality 6" x 9" black and white photographic prints are available for any photographs or illustrations appearing in this copy for an additional charge. Contact UMI directly to order.

U·M·I

University Microfilms International
A Bell & Howell Information Company
300 North Zeeb Road. Ann Arbor. MI 48106-1346 USA
313/761-4700 800/521-0600

Order Number 9234723

An investigation of protein crystal growth by laser light scattering

Bishop, John Bradford, Ph.D.

University of Alabama at Birmingham, 1992

U·M·I
300 N. Zeeb Rd.
Ann Arbor, MI 48106

AN INVESTIGATION OF PROTEIN CRYSTAL GROWTH BY LASER LIGHT SCATTERING

by

JOHN B. BISHOP

A DISSERTATION

Submitted in partial fulfillment of the requirements for the degree of
Doctor of Philosophy in the Department of Physics in the Graduate School,
The University of Alabama at Birmingham

BIRMINGHAM, ALABAMA

1992

ABSTRACT OF DISSERTATION
GRADUATE SCHOOL, UNIVERSITY OF ALABAMA AT BIRMINGHAM

Degree Doctor of Philosophy Major Subject Physics

Name of Candidate John B. Bishop

Title An Investigation of Protein Crystal Growth by Laser Light Scattering

Laser light scattering is utilized here to unobtrusively probe the submicroscopic, macromolecular events within solutions from which protein crystals grow. Lysozyme and protamine insulin were studied. In this study the formation of a precrystalline aggregate is distinguished from that of an amorphous precipitant by photon correlation spectroscopy and by classical absolute scattering intensity measurements. A slight decrease in diffusion and a slight increase in intensity are shown to mark isothermal lysozyme nucleation. Light scattering is not typically done on supersaturated solutions, so before drawing conclusions, photon correlation with multiple scattering vectors (multi-q) was used to investigate interparticle interactions within "monomeric" lysozyme solutions. The concentration and temperature dependence of the effective hydrodynamic diameter of monomeric lysozyme were determined.

In the supersaturated solutions the effective hydrodynamic diameter of the quasiequilibrium state is seen to vary with the degree of supersaturation. In the monomeric solutions the influence of hydrodynamic interactions is shown to predominate that of the thermodynamic interactions. It is concluded that, although interparticle interactions affect the measurement of the effective diameter, small order aggregates are forming within the scattering volume during nucleation. Qualitative size distributions are presented, and scattering parameters for monitoring dynamically controlled lysozyme nucleation are offered.

Abstract Approved by: Committee Chairman William M. Rosenblum

Program Director

Date 6/17/92 Dean of Graduate School W. A. Sibley

DEDICATION

This work is dedicated in loving memory of my father, John Liebert deWeese Bishop. On many occasions, I long for his counsel.

ACKNOWLEDGEMENTS

This work was continuously supported by NASA funds through committee member, Dr. Lawrence DeLucas of the UAB Center for Macromolecular Crystallography and would not have been possible otherwise. Substantial support was also received in 1990-1991 as a fellowship with the Alabama Space Grant Consortium (NGT-40010). Initial funding was received from NASA grant NAG8-733 through committee chairman, Dr. William Rosenblum. I would also like to thank the others who served on my committee, Dr. James Martin, Dr. Michael Lewis, Dr. Jimmy Mays, Dr. Tom Nordlund, Dr. Fred Suddath, and Dr. John Young.

There were many who contributed to the work at UAB. My thanks to: Dr. Bill Christens-Barry, Mr. Jerry Stewart, Mr. Ken Norris, Mr. Jake Matlock, Dr. Marianna Long, and Mr. Tobin Fisher. I also wish to thank the Physics Dept. Chairman, Dr. David Shealy for his constant support.

The invitation to use UAH facilities was graciously extended by Dr. Franz Rosenberger of the UAH Center for Microgravity Materials Research. Guidance was received from Dr. William Fredericks. Interaction with Dr. Tsutomu Sawada proved invaluable as did the assistance of Mrs. Sandra Howard and Mrs. Jennifer Sowers.

The loving support of my wife and family sustained me. I couldn't have done it without you Sue. Thank you Clay, Christine, Rachel, Bobbie, and Ellie.

TABLE OF CONTENTS

Page

ABSTRACT ii

DEDICATION iv

ACKNOWLEDGEMENTS v

LIST OF TABLES viii

LIST OF FIGURES ix

I. INTRODUCTION 1
  - A. Background 1
  - B. Overview 5
    - 1. History of the research 5
    - 2. Findings 6

II. THEORETICAL 9
  - A. Protein crystallization 9
    - 1. Solubility 9
    - 2. Dynamically controlled protein crystal growth 11
    - 3. Kinetics - the theory of Kam and Feher 12
  - B. Laser light scattering 18
    - 1. Dynamic light scattering/photon correlation spectroscopy 25
      - a. The quasielastic event and the scattered electric field 25
      - b. Photon correlation spectroscopy 27
    - 2. Classical light scattering 35
      - a. Rayleigh scattering 36
      - b. Mie scattering 36

TABLE OF CONTENTS (Continued)

Page

III. EXPERIMENTAL 46
  A. UAB experimental 46
    1. The Brookhaven instrument and peripherals 46
    2. The Wyatt instrument 50
    3. Lysozyme 50
    4. Protamine insulin 52
  B. UAH experimental 53
    1. The Brookhaven instrument and peripherals 53
    2. Lysozyme 57

IV. RESULTS 59
  A. UAB results 59
    1. Lysozyme 59
    2. Insulin 78
  B. UAH results 87

V. DISCUSSION AND CONCLUSIONS 105
  A. Interparticle interactions within monomeric lysozyme 105
    1. The friction as represented by d_{eff} 106
    2. Discussion of D_0 and k_D 108
  B. Supersaturated lysozyme solutions 111
    1. PRAGG's 113
    2. CRAGG's 118
    3. PRAGG's vs CRAGG's 130
  C. Discussion of results from protamine insulin 135
  D. Conclusions 138
    1. Nucleation 138
    2. Monitoring 150
    3. Summary 151
  E. Recommendations and closing remarks 154

REFERENCES 168

LIST OF TABLES

Table Page

I. The conditions of the supersaturated lysozyme solutions are shown with λ_0 103

II. The concentrations and temperatures for the investigation of lysozyme at 0.8% (0.15M) NaCl and pH 4.5 are shown...... 104

III. The variation in d_{eff} due to temperature and concentration is summarized 109

IV. The linear regressions of Fig. 27 coupled with Eq. (36) yield these values of D_0 and k_D 110

V(a). The behavior of d_{eff} during PRAGG formation is summarized 114

V(b). The forward scattering behavior during PRAGG formation is summarized 114

VI. Results from the PCS measurements during crystallization are summarized by these monitoring parameters 131

VII. The forward scattering behavior of L3 - L6 during crystallization is summarized 132

LIST OF FIGURES

Figure Page

1. Solubility of the tetragonal form of lysozyme as published by Cacioppo and Pusey.[18] 10

2. Dynamically controlled crystal growth prototype 13
   (a) Growth module with vapor control 13
   (b) Thermal control of modules 13
   (c) Detector setup 13

3. A scale drawing depicting the submicroscopic events of lysozyme aggregation 19
   (a) At c = 50 mg/ml there are approximately 110 molecules in a 52 500 nm^3 volume 19
   (b) PRAGG's 19
   (c) PreCRAGG's in quasiequilibrium 19
   (d) A CRAGG forms and falls out of solution 19

4. The scattering plane is perpendicular to the direction of polarization of the incident beam 24

5. The scattering vector is defined $\mathbf{q} \equiv \mathbf{k}_i - \mathbf{k}_s$ 26

6. The ideal scattering geometry: N spherically shaped, monodisperse, noninteracting, Rayleigh scatterers 28

7. The Drake and Gordon[28] approximation of Eq. (39) is shown for ka = 2.0, 6.0, and 10.0 in (a), (b), and (c), respectively 39
   (a) For $ka = 2.0, j \approx$ 145 000 39
   (b) For $ka = 6.0, j \approx$ 3 900 000 39
   (c) For $ka = 10.0, j \approx$ 18 000 000 39

LIST OF FIGURES (Continued)

Figure Page

8. The scattered intensity for a distribution of Mie scatterers is shown on the same arbitrary scale as Fig. 7 41

9. The appearance and subsequent increase in forward scattering as predicted by the Drake and Gordon[28] approximation is shown in (a) - (d) 43
   (a) The distribution of Fig. 8 is combined with 10^9 scatterers of ka = 0.07, the approximate ka for lysozyme monomers at λ_0 = 488 nm 43
   (b) The amplitude of the distribution is multiplied by 5...... 43
   (c) The amplitude of the distribution is multiplied by 10.... 43
   (d) The amplitude of the distribution is multiplied by 15.... 43

10. The Brookhaven setup at UAB 48

11. The Brookhaven setup at UAH 54

12. An absorbance scan of lysozyme at room temperature: c = 18.5 mg/ml, 0.8% NaCl, and pH 4.5 60

13. Intensity vs angle on a logarithmic scale for 5 mg/ml lysozyme at pH 4.4 and 10% NaCl 61

14. The appearance and subsequent increase in forward scattering consistent with a polydisperse system of Mie scatterers (λ_0 = 488 nm) is shown 63

15. Displayed in (a) - (c) are the results of Sample L1: 6.75 mg/ml lysozyme, pH 4.4, 6.5% NaCl, T = 30°C, and λ_0 = 488 nm 64
   (a) The increase in FS over time is shown 64
   (b) The single-τ d_{eff} is seen to behave similarly to FS 64
   (c) The behavior of multi-τ d_{eff} is compared to that of single-τ d_{eff} 64

LIST OF FIGURES (Continued)

Figure Page

16. Displayed in (a) - (d) are the results of Sample L2: 6.75 mg/ml lysozyme, pH 4.4, 6.5% NaCl, T = 30°C, and λ_0 = 488 nm 67
    (a) The increase in FS and single-τ d_{eff} over time is shown 67
    (b) The behavior of multi-τ d_{eff} is compared to that of single-τ d_{eff} 67
    (c) The first 300 min of FS and single-τ d_{eff} are shown 67
    (d) The first 300 min of single-τ d_{eff} and multi-τ d_{eff} are shown 67

17. Crystals appeared in this sample, L3: 16 mg/ml lysozyme, pH 4.4, 3.0% NaCl, and λ_0 = 488 nm 71
    (a) FS vs time is shown 71
    (b) Single-τ d_{eff} vs time is shown 71
    (c) Multi-τ d_{eff} is seen to compare favorably to single-τ d_{eff} 71

18. Crystals appeared in sample L4: 21 mg/ml lysozyme, pH 4.4, 3.0% NaCl, and λ_0 = 488 nm 74
    (a) FS vs time is shown 74
    (b) Single-τ d_{eff} vs time is shown 74
    (c) Multi-τ d_{eff} is seen to deviate from single-τ d_{eff} 74
    (d) A portion (1000 min $\leq t \leq$ 3000 min) of (b) is shown... 74

19. The results of insulin sample I1 are displayed 80
    (a) FS vs time is shown 80
    (b) Single-τ d_{eff} vs time is shown 80
    (c) Single-τ d_{eff} is compared to multi-τ d_{eff} 80

20. The results of insulin sample I2 are displayed 83
    (a) FS vs time is shown 83
    (b) Single-τ d_{eff} vs time is shown 83
    (c) Single-τ d_{eff} is compared to multi-τ d_{eff} 83

21. The results of insulin sample I3 are displayed 86

LIST OF FIGURES (Continued)

Figure Page

22. Shown in (a) - (c) are the D_{lin}, D_{2nd}, and I results at three angles for the UAH lysozyme sample L5: 47.0 mg/ml lysozyme, pH 4.5, 2.5% NaCl, T = 11°C, and λ_0 = 413.6 nm 88
    (a) $\theta = 24°$ 88
    (b) $\theta = 45°$ 88
    (c) $\theta = 90°$ 88

23. I(24)/I(90) vs time is shown for L5 91

24. Shown in (a) - (c) are the D_{lin}, D_{2nd}, and I results at three angles for the UAH lysozyme sample L6: 55.7 mg/ml lysozyme, pH 4.5, 3.0% NaCl, T = 11°C, and λ_0 = 413.6 nm 92
    (a) $\theta = 30°$ 92
    (b) $\theta = 60°$ 92
    (c) $\theta = 90°$ 92

25. FS vs time is shown for L6 95

26. The figure shows typical results for the monomer studies 97

27. The concentration dependence of D_{eff} with 95% confidence limits is shown at the four common temperatures 98

28. The free particle hydrodynamic diameter d_0 at the four common temperatures is compared to the value published by Dubin et. al.[29] 99

29. k_D vs T is shown with an arbitrary parabolic fit 100

30. Concentration and temperature effects on d_{eff} are illustrated 101
    (a) The four complete temperature sets are shown with 95% confidence limits 101
    (b) All data are shown with error bars removed for clarity 101

LIST OF FIGURES (Continued)

Figure Page

31. The magnitude of the slopes of the regressions of Fig. 30 is plotted vs c 107

32. The 95% confidence limit of the measures of d_0 are seen to encompass the Dubin[29] value 112

33. The range of fluctuations that a PCS measurement is sensitive to depends on the domain of $g_2(\tau)$ 116
    (a) The single-τ is sensitive to the smaller sizes of a continuous size distribution 116
    (b) The multi-τ extends the domain of $g_2(\tau)$ without great sacrifice in sensitivity to the smaller sizes 116

34. A normalized size distribution is seen moving past a single-τ window 119

35. The evolution of the PRAGG distribution is depicted 121
    (a) The system begins with monomers and some small j-mers 121
    (b) Aggregation continues until the distribution is skewed to the Mie regime 121

36. The criteria are set for the meaning of the terms small, medium, and large as used in the discussion 124

37. The ratio of the diffusion coefficients measured at the forward angle to those of the rearward angle is plotted for L5 128

38. The ratio of the diffusion coefficients measured at the forward angle to those of the rearward angle is plotted for L6 129

39. Shown for L5 is d_{eff} at $\theta = 45°$ as computed from D_{2nd} 133

40. Shown for L6 is d_{eff} at $\theta = 60°$ as computed from D_{2nd} 134

LIST OF FIGURES (Continued)

Figure Page

41. The scattering volume is shown in relation to the growing crystals 136

42. An illustration of the evolution of the preCRAGG distribution during CRAGG formation 140
  (a) The quasiequilibrium distribution is peaked at the monomer and probably contains some preCRAGG's ($j < 10$) 140
  (b) At supersaturation the size distribution at quasiequilibrium is not static, and the preCRAGG's approach j_c 140
  (c) The preCRAGG's continue to approach j_c 140
  (d) The critical nucleus is reached 140
  (e) The preCRAGG's and CRAGG's continue to form 140
  (f) As particles are removed from solution to the solid phase, the distribution relaxes 140
  (g) The distribution continues to relax 140
  (h) A new, relaxed quasiequilibrium is established among the preCRAGG's 140

43. The quasiequilibrium state is shown to be dependent on the degree of supersaturation, $(c - c_{sol})/c_{sol}$ 147

44. The values of d_{final} for L5 and L6 are included for the data of Fig. 43 149

45. A summary of the qualitative size distributions for the three cases of Kam and Feher[36] 152
  (a) This demonstrates the distribution of preCRAGG's that influences PCS measurements of the crystallizing sample, case (1) 152
  (b) Case (2) PRAGG's aggregate too quickly to measure by light scattering and reach visible sizes 152
  (c) The aggregation of case (3) PRAGG's may be followed by light scattering 152

46. Shown here are 42 conditions for each ionicity 156

CHAPTER I

INTRODUCTION

A. Background

The most satisfying method of obtaining the three-dimensional structure of biological macromolecules remains x-ray crystallography. It is not likely to be replaced by other techniques in the near future. The information gained from these crystallographic studies underlies human understanding of the mechanisms by which proteins and nucleic acids function in biological systems. This understanding is imperative for the development of novel drugs and synthetic vaccines and for continued advancement within the field of protein engineering.

The structural information of about 600 proteins is currently stored in The Protein Data Bank.[9] This information, together with structure-function relationships, is used in modern drug design to develop the means to suppress or enhance the function of proteins in a given biological situation. For example, purine nucleoside phosphorylase (PNP) is a protein whose function is necessary in the operation of the human T-cell immune system. Thus, by inhibiting PNP's function the immunity system can be controlled.[24] Also, PNP is known to degrade nucleoside analogues, which are active components of chemotherapy drugs, so by inhibiting PNP, the effectiveness of the chemotherapy may be increased. The structure of PNP,[20,30,31] provided by the Center for Macromolecular Crystallography at the University of Alabama in Birmingham (UAB), has recently been used to develop drugs which may inhibit the function of PNP. From about 60 designs based totally on PNP's structure, six drugs have been selected to undergo clinical trials.[24] Ordinary design and test methods result in the *in vitro* testing of thousands of drug designs before one is selected for clinical trials. Should one of these six possible inhibitors succeed in clinical trials, the accurate knowledge of the three-dimensional structure of PNP will have reduced the necessary number of test designs by two orders of magnitude!

Furthermore, with recent advances in site-directed mutagensis, protein engineering is at a point where it is possible to make mutant and modified proteins at will, but there already exist cases in which the mutant protein behaves much differently from predictions of behavior based on the parent protein's function.[71] For this reason, the three-dimensional structural information is not only the foundation for the methodology of protein engineering, but it also plays an integral role, with thermodynamic and biochemical information, in any attempt at predicting a mutant's function.

The essential steps in achieving this quintessential three-dimensional structure of a protein are:[16]

(1) purification of a sufficient quantity of the protein,
(2) crystallization of the protein,
(3) collection of diffraction data on the native crystal and on crystals containing a heavy atom derivative,
(4) calculation of an electron density map from which a protein model is developed, and
(5) refinement of the protein model.

Recent technological advances have significantly enhanced the capabilities of the crystallographer. For example, present recombinant DNA techniques make it possible to provide some important proteins in quantities sufficient for crystallographic study and hold the promise of providing other important proteins in the future[21,35,37,38,50,68,72,96]; modern synchrotron x-ray sources provide intensities great enough to permit rapid collection of data by steadily evolving area detector systems[6,42,45,46,65,95]; new methods in computer graphics have revolutionized the construction of protein models from electron density maps and have also provided the ability to interpret structures easily[7,48,66]; new software systems continue to provide a variety of approaches to model refinement,[47,54,58,93] and the increasing availability of supercomputers make the use of this powerful software routine.

As one reviews these advances in parallel with the essential steps for attaining protein structure, it is curious that there have been no technological advances to enhance the crystallographer's capability to perform the second essential step, crystallization. It is this step, therefore, that is the major "bottleneck" for modern protein crystallography.[25] Indeed, many ambitious projects in structure based research are terminated in the crystal growth stage.

The shortcomings of protein crystal growth arise from the fact that growth occurs within complex, multiparametric, biochemical solutions. The problem is compounded by the fact that each protein has its own unique set of crystallization conditions which are found quite fortuitously by a trial and error, "shotgun" approach. Many proteins resist attempts at crystallization, and many semi-crystallize into states inappropriate for diffraction study.

At this point in time, achievement of the 3-D structure of cell membrane proteins is of tantamount importance within the medical/biological community,[15] for these proteins are the interface between the internal mechanisms of the cell and its environment. They provide the medium of communication and transport from the chromosomes to the cell's surroundings and vice versa. Due to the fact that the outer portions of these proteins are usually hydrophylic while the inner portions, which are in contact with the lipid bi-layer, are hydrophobic, crystallization of the membrane proteins remains quite a challenge.

One alternative method for attaining protein structure is two-dimensional nuclear magnetic resonance (2-D NMR). This method does not depend on crystallization but is limited to low molecular weight proteins. Another alternative approach is the very new concept of optical matter[17] which uses very intense laser diffraction patterns to align particles in a periodic array. This method seems particularly well suited for the study of membrane proteins since it does not rely on conventional crystallization. This technique, however, has not evolved past the conceptual stages. Therefore, one once again arrives at the importance of protein crystal growth.

The concept of Dynamically Controlled Protein Crystal Growth (DCPCG) has recently been conceived by researchers and colleagues of the UAB Center for Macromolecular Crystallography and presented to NASA for funding under the Advanced Protein Crystal Growth program.[89] Conceptually, DCPCG separates the nucleation stage from the subsequent growth stage. Rosenberger et al.[82] assert that the protein crystallization process parallels that of smaller inorganic molecules and point out that a higher degree of supersaturation is required for nucleation than for subsequent growth.[70] Therefore, once nucleation is achieved a variation of solution parameters could discourage further nucleation while allowing formed nuclei to flourish. This would enhance the quality of the final product.

This dissertation is not concerned with the method by which the degree of supersaturation is reduced. Rather, *the focus of this research is that of monitoring the nucleation event and of contributing to the characterization of the event.* Monitoring nucleation is essential to the success of DCPCG and requires an unobtrusive probe. Laser light scattering is a logical choice. Light scattering is typically done at wavelengths exceeding 400 nm. Most proteins do not absorb at wavelengths greater than 350 nm, so the scattering event should remain quasielastic. Although light scattering is the logical choice, the literature contains little information on scattering from supersaturated solutions.[4,5,10,36,49,51,99,100]

Having argued for the importance of advancement in protein crystal growth and having stated DCPCG as a possible mechanism for such advancement and having introduced laser light scattering as a component of DCPCG, the introduction proceeds to outline the research history and the findings.

B. Overview

1. History of the research

Data for this research were collected at the UAB Laser Facility for Biophysical Studies and at the Center for Microgravity Materials Research at the University of Alabama in Huntsville (UAH). The research began at UAB with *the goal of using laser light scattering to monitor the nucleation event of three different proteins and of identifying the measured behavior* *of the events specific to each protein.* Initial experiments utilized the Wyatt Dawn-B instrument to make classical I(θ) measurements of supersaturated lysozyme solutions over time. This device, without temperature control, was not suitable for this study, and its use was discontinued. Brookhaven instrumentation had both classical and dynamic light scattering capabilities and the sample was temperature controlled. This equipment was used for the duration of the work at both UAB and UAH.

Work with temperature induced lysozyme nucleation at UAB continued until the behavior of both amorphously precipitating and crystallizing solutions was determined. The research then focused on insulin. These samples formed an amorphous precipitate along with crystals, and meaningful data were obscured. After unsuccessful efforts to eliminate this problem, measurements of insulin were discontinued, and a new goal evolved: *Based on previous success with lysozyme, resume experimentation and contribute to the indisputable characterization of the nucleation event.*

Work resumed at UAH using ultrapure lysozyme samples that were being prepared there for microscopy studies. Data for isothermal nucleation were collected and favorably compared to the UAB data. A fundamental study of monomeric lysozyme solutions ensued in an attempt to analyze the behavior witnessed during crystallization. This led to some understanding of the interactions between the lysozyme ions at low ionic strength but at concentrations and temperatures that support nucleation.

2. Findings

This work includes multi-q and multi-τ (see Sec. II.B.1) photon correlation spectroscopy (PCS) measurements, as well as classical intensity measurements, and confirms the behavior of the effective hydrodynamic diameter during lysozyme crystallization to be as reported by Mikol et al.[63] In contrast to Mikol, this research emphasizes that the measurement is not totally one of particle size. Interparticle interactions are investigated and shown to influence the effective diameter to an extent comparable to the changes observed during isothermal nucleation. The effective diameter d_{eff} is a representation of the friction experienced by the scatterers less the viscosity. This includes particle size and interactions. It is concluded from absolute intensity behavior, however, that the aggregate size distribution is a primary contributor.

Interpretation of the interactions is based on the model of Anderson and Reed.[3] The free particle hydrodynamic diameter d_0 is found to be consistent with the value calculated from the free particle diffusion coefficient D_0 published by Dubin et al.[29] In low ionic strength, monomeric solutions, where particle size is discounted, interactions are shown to increase d_{eff} from d_0 as concentrations and temperatures approach those of nucleation. This increase is greater than 10% of d_0 and is attributed to the prominence of hydrodynamic interactions.

Conclusions on nucleation are based on the theory of Kam and Feher.[36,51] The increase in d_{eff} during isothermal nucleation is about 7%. The quasiequilibrium state yields $d_{QE} > d_0$ consistent with Kam and Feher. The effective diameter during quasiequilibrium d_{QE} is shown to be dependent on supersaturation.

For the purpose of *in situ* monitoring of protein crystal growth, it is shown that the formation of an aggregate of amorphous precipitate (PRAGG) can be distinguished from the formation of a precrystalline aggregate (preCRAGG) distribution. At $\lambda_0 = 488$ nm a deviation of I(30)/I(90) from one (see Sec. II.B.2) indicates PRAGG formation and is an unfavorable condition for the solution. A sharp increase in d_{eff} is shown to signal nucleation. For a record of d_{eff} during the lysozyme nucleation event, a single-τ ($0 < q^2\tau \leq 1 \times 10^7$ s/cm^2) PCS measurement is found to encompass the proper fluctuations, and multi-q measurements are recommended.

Although work with lysozyme solutions was tedious and PRAGG's were often an unintentional result, protamine insulin proved to be totally unpredictable. Considerable effort with these samples showed only that the onset of nucleation could be detected by light scattering. PCS measurements during insulin nucleation were impossible.

Overall, the findings of this research are of considerable benefit to DCPCG and provide a foundation for further study of lysozyme nucleation. An indisputable characterization of the nucleation event and of precursory molecular events remains elusive.

CHAPTER II

THEORETICAL

A. Protein crystallization

1. Solubility

Solubility is defined as the amount of solute that can be dissolved in a given amount of a particular solvent at a particular condition. At conditions above the solubility the solution is said to be supersaturated. When a solution reaches two to three times the solubility the solvent molecules are forced out of solution as a precipitate. Sleet and snow are excellent examples of a precipitate and simply demonstrate the fact that the resulting precipitate under given solution conditions may be an amorphous aggregation of solute molecules or an ordered crystalline array. Obviously, the interests of protein crystal growth are in obtaining large, high quality, ordered crystalline arrays (protein crystals) of protein molecules for x-ray diffraction studies. At this time lysozyme is the only protein for which the solubilities over a wide range of conditions have been determined. Figure 1 presents the solubility curve for lysozyme at pH 4.5 as determined by Cacioppo and Pusey[18] by the packed microcolumn technique[76] developed at Marshall Space Flight Center. It was these data that were consulted here. Further work by Rosenberger et al.[81] using scintillation techniques has shown excellent agreement with Cacioppo.

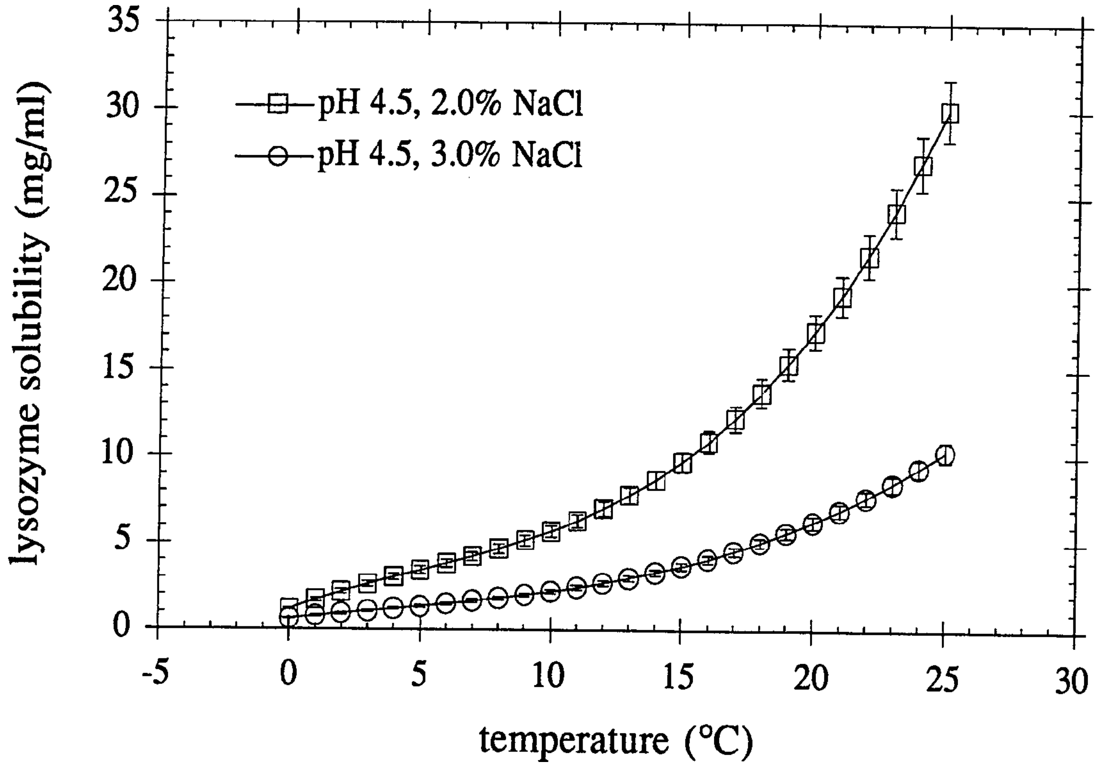

FIG. 1. Solubility of the tetragonal form of lysozyme as published by Cacioppo and Pusey.[18] The curves are from third order polynomials taken from Ref. 18, and the error bars reflect the reported %error. The conditions nearest to those used in this work are shown: pH 4.5; 2.0% and 3.0% NaCl.

2. Dynamically controlled protein crystal growth

Early investigations of inorganic crystal growth by Ostwald[70] demonstrated that nucleation requires a higher degree of supersaturation than does post nucleation growth. This motivates DCPCG. If the nucleation event is detected, then the degree of supersaturation can be lowered by changing solution parameters. Temperature, ionic strength, and protein concentration are parameters which strongly affect the degree of supersaturation of lysozyme; ionic strength and temperature control the solubility point, and protein concentration determines the degree above solubility. The lower supersaturation level would deter secondary nucleation and allow the first nuclei to flourish. The subsequent growth of the first nuclei would then be free from[82]: 1) perturbations in the concentration field due to many growing crystals; 2) misoriented growth due to attachment of other crystals; and 3) defects caused by collisions with other crystals.

Popular methods of achieving supersaturation in protein crystal growth (PCG) solutions include liquid-liquid diffusion,[84,85] dialysis,[61,101] and vapor diffusion.[25] All these methods have adopted microscale technologies so that only microliter quantities of protein are required. Miniaturization of any PCG technique is essential because of the expense of important protein.

PCG experiments are currently being performed in free fall on board the space shuttle to remove the convective flows originating from concentration gradients around growing crystals. The hanging drop vapor diffusion technique, used for these studies, has demonstrated the utility of PCG in space.[26,59] The next step in these studies will include the *in situ* variation of solution parameters by a payload specialist on USML 1. The

USML experiments will detect microscopic crystals by ordinary white light microscopy and then adjust parameters, but later experiments are proposed to include laser light scattering as a detector/monitor of submicroscopic events.

Figure 2 shows the conceptual design of a DCPCG apparatus as presented to an Advanced Protein Crystal Growth working group in 1989.[89] Laser light scattering, which is amenable to miniaturization,[14,27,53] is used to detect nucleation and other submicroscopic events. Solution conditions can be changed by varying the saturation of a gas circulated over the solution as demonstrated by Wilson, Bray, and Suddath.[98] Temperature is controlled by Peltier devices as shown.

3. Kinetics - the theory of Kam and Feher

The theoretical aspects of small molecule crystal growth have been addressed in many treatises.[1,12,34,40,41,57,80] These are confidently used as the basis for interpretation of results from projects involving crystallization of a new material or from projects attempting improvement of the crystal quality of a commonly crystallized material. No such foundation exists for protein crystallization. Kam and Feher[36,51] have provided some insight into the process of lysozyme growth, but many questions remain, especially with regard to prenucleation and nucleation events. Even if the events of lysozyme growth were thoroughly modeled, one could not totally generalize the model to other protein systems, but if such a model existed, it would provide the basis for characterization of the events within other systems.

Kam and Feher have based their interpretations on the assumption that an aggregate grows by successive addition of monomers and have

FIG. 2. Dynamically controlled crystal growth prototype.

(a) Growth module with vapor control.

1 - Laser
2 - Beam Focusing Lens
3 - Detector Positions
4 - Beam Stop
5 - Sample Insertion
6 - Video.
7 - Vapor Chamber
8 - Wicking Agent Input
9 - Wicking Agent Output
10 - Seal
11 - Lighting Strip

(b) Thermal control of modules.

(c) Detector setup.

1 - Index Matching Fluid
2 - Lens
3 - Pinhole
4 - Detector
5 - Detector Output Wires
6 - O ring Seal.

(a)

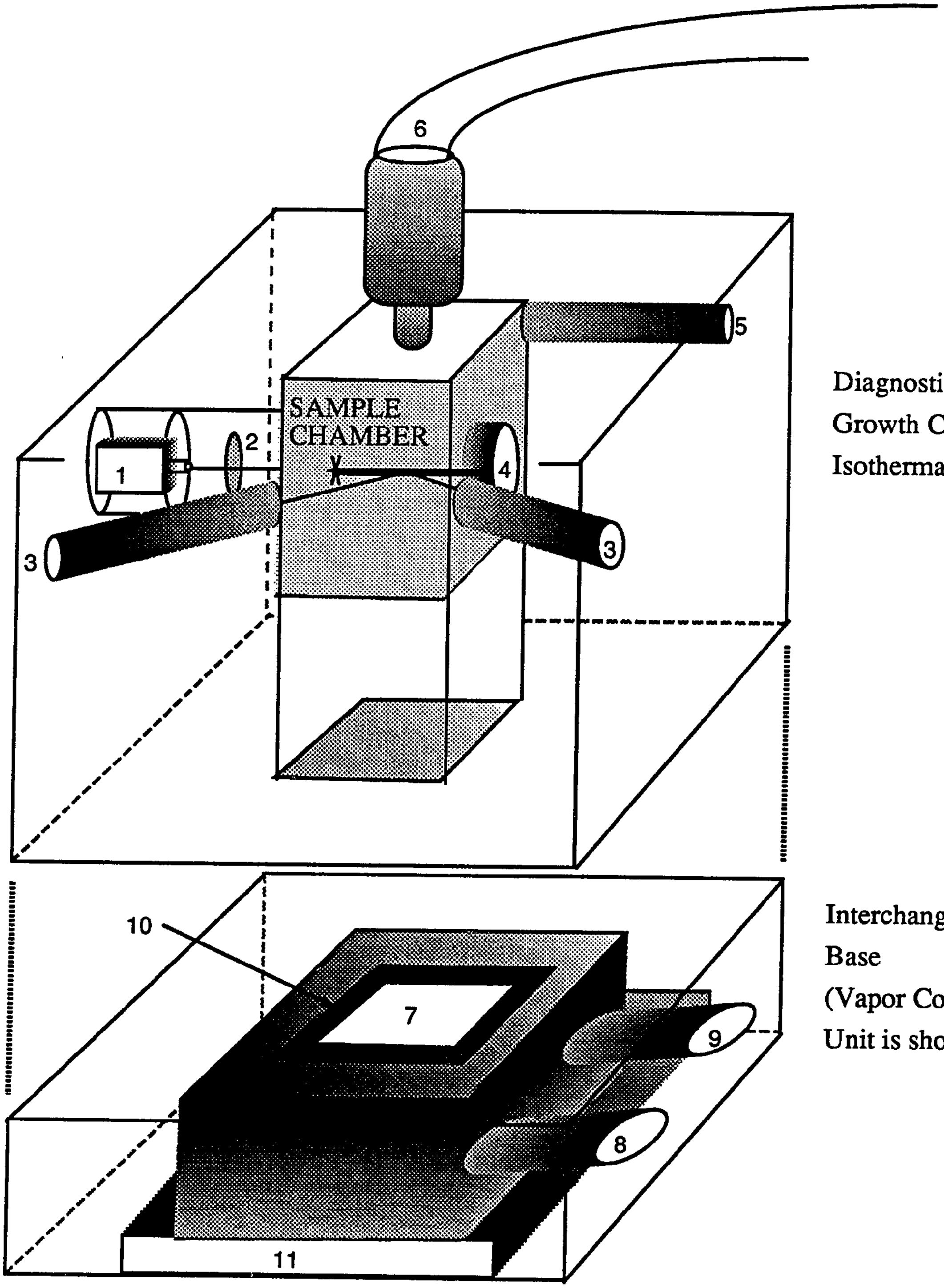

Diagnostics and
Growth Cell in
Isothermal Block

Interchangeable
Base
(Vapor Control
Unit is shown.)

(b)

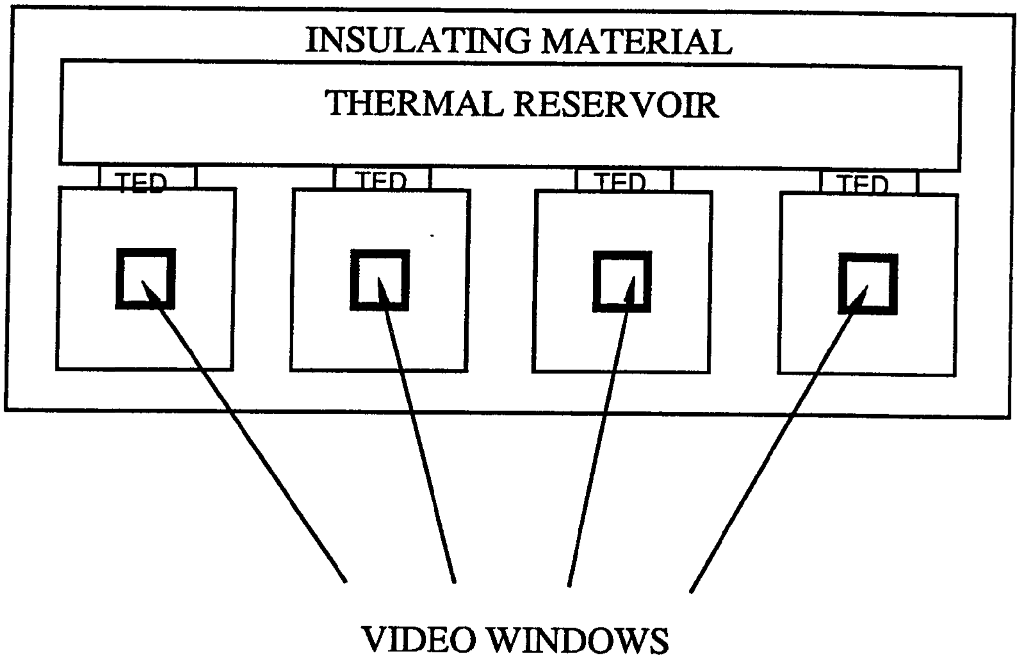
INSULATING MATERIAL
THERMAL RESERVOIR
TED
TED
TED
TED
VIDEO WINDOWS

(c)

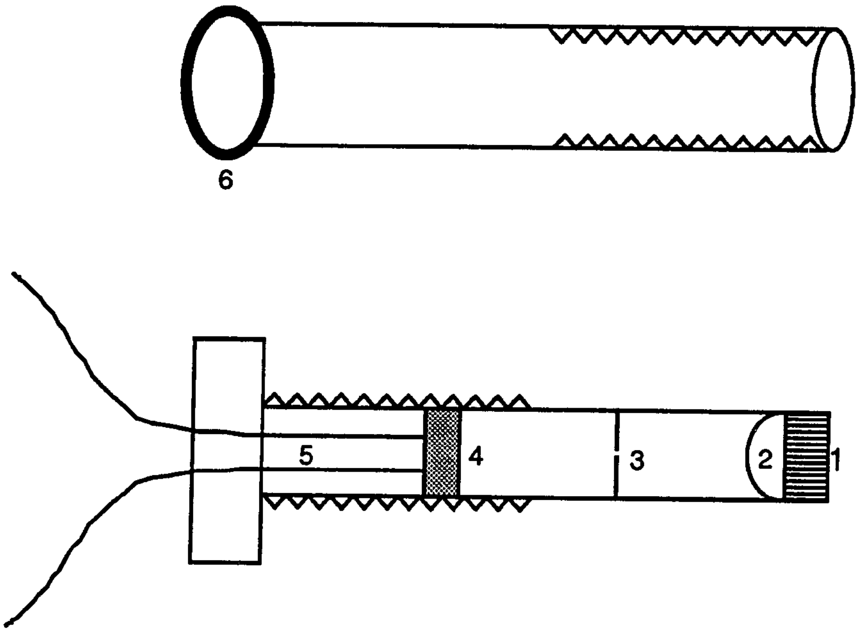
6
5
4
3
2
1

described the process by a chain of association/dissociation reactions given by:

$$A_j + A_1 \underset{k_{j+1}^b}{\overset{k_j^f}{\Leftrightarrow}} A_{j+1} \quad ,$$

and

$$K_j \equiv \frac{k_j^f}{k_{j+1}^b} \quad .$$

The lower case k's represent the forward and backward reaction rate constants, and K_j is the equilibrium constant for the reaction of an aggregate j-mer A_j with a monomer A_1.

The assertion is that two major pathways by which aggregates grow are possible. The first is the ordered addition of monomers to form a three-dimensional crystal, and the second is the addition of a monomer to a linear, spatially disordered chain to form an amorphous aggregate. The former aggregate has recently acquired the jocular acronym[100] CRAGG (crystalline aggregate) and the latter PRAGG (precipitate aggregate). The equilibrium constants for the two pathways are then K_j^{CRAGG} and K_j^{PRAGG} (the notation used by Kam and Feher was K_j^{XTAL} and K_j^{AMOR}).

From surface free energy considerations of the PRAGG it is logically argued that all K_j^{PRAGG} are approximately equal due to the constancy of two binding sites (one on each end of the chain) for each PRAGG for all j.

For CRAGG's it is established that due to competition between a surface free energy term proportional to r^2 (where r is the aggregate radius) and a volume free energy term proportional to r^3, $K_\infty^{CRAGG} >> K_1^{CRAGG}$. The addition of a monomer to a growing crystal of macroscopic size is represented by K_∞^{CRAGG}, and K_1^{CRAGG} is for the formation of the first dimeric aggregate. This directly implies

$$\frac{K_\infty^{PRAGG}}{K_1^{PRAGG}} \approx 1 \text{ , and } \frac{K_\infty^{CRAGG}}{K_1^{CRAGG}} >> 1 \quad .$$

Also, $K_1^{CRAGG} \neq K_1^{PRAGG}$ since different kinds of bonds are most certainly involved.

With this background and with the assumption that K_1 varies with solution conditions (e.g., pH and ionicity), Kam and Feher present three possible cases[36]:

(1) If $K_1^{CRAGG} > K_1^{PRAGG}$, then $K_j^{CRAGG} > K_j^{PRAGG}$ for all j. CRAGG's of all sizes are energetically favored over PRAGG's, and crystals will result.

(2) If $K_1^{CRAGG} << K_1^{PRAGG}$, then possibly $K_\infty^{CRAGG} < K_\infty^{PRAGG}$. PRAGG's are favored and no crystals will form. A crystal placed in such a solution will dissolve.

(3) If $K_1^{CRAGG} < K_1^{PRAGG}$ and $K_\infty^{CRAGG} > K_\infty^{PRAGG}$, then large CRAGG's are more stable than large PRAGG's, but small PRAGG's are more stable than small CRAGG's. In this case small PRAGG's form and deplete the solution of monomers to such an extent that large CRAGG's are never developed; that is no nucleation occurs. However, a crystal placed into this solution might continue to grow.

For case (2) there is no competition between the r^2 and r^3 terms, so PRAGG's begin to associate immediately upon supersaturation. For case (1) a theoretical time period t_{QE} is necessary to establish a quasiequilibrium state among preCRAGG's. The size of the aggregates and the distribution during quasiequilibrium are dependent on solution conditions. Then, after a short time delay t_d preCRAGG j-mers begin to reach a critical value j_c and the volume term dominates. Nucleation is then initiated and CRAGG growth proceeds rapidly. In this case, $t_d >> t_{QE}$, and both are inversely dependent on k_2^b. The term preCRAGG is used in the present work for j-mers of $j < j_c$ and the term CRAGG is used for actual nuclei and growing crystals (i.e., $j > j_c$). Figure 3 illustrates the fundamental differences in the PRAGG's, preCRAGG's, and CRAGG's.

B. Laser light scattering

The scattering measurements of interest here are a measure of the visible electromagnetic energy that is elastically scattered from an incident beam by each constituent of a particle ensemble. The elastic nature of the scattering event may be assured by the choice of incident energy. These experiments utilize the coherent radiation of a laser beam, so the incident energy is governed by the choice of wavelength λ_0. The ensemble of scatterers consists of small solvent particles characterized by the solvent index of refraction, n, and of large solute particles, which are, of course, of ultimate interest. Each scatterer contributes to the scattered intensity in two ways: a static contribution, which depends on the shape of a particle and its dimensions relative to the incident wavelength, and a dynamic contribution, which depends on the particle motion. Thus, the intensity at any point within the scattered field fluctuates rapidly about a mean value.

To make the situation mathematically manageable, the scattering geometry (see Fig. 4) is chosen such that the scattered energy is detected within a plane, defined by the incident and scattered ray, perpendicular to the incident polarization. Dynamic light scattering investigates the dynamic property of the ensemble by measurement of the time dependent scattered intensity $I(t)$ at a fixed scattering angle θ, and classical light scattering investigates the static property by measurement of the time averaged scattered intensity I vs θ. Here $I(t)$ was investigated by photon correlation

FIG. 3. A scale drawing depicting the submicroscopic events of lysozyme aggregation. The scale is 1 cm = 5 nm, and the monomer is illustrated as a prolate ellipsoid, 3.3 x 5.5 nm.

(a) At c = 50 mg/ml there are approximately 110 molecules in a 52 500 nm^3 volume. The average center to center distance is 7.81 nm.

(b) PRAGG's.

(c) PreCRAGG's in quasiequilibrium.

(d) A CRAGG forms and falls out of solution.

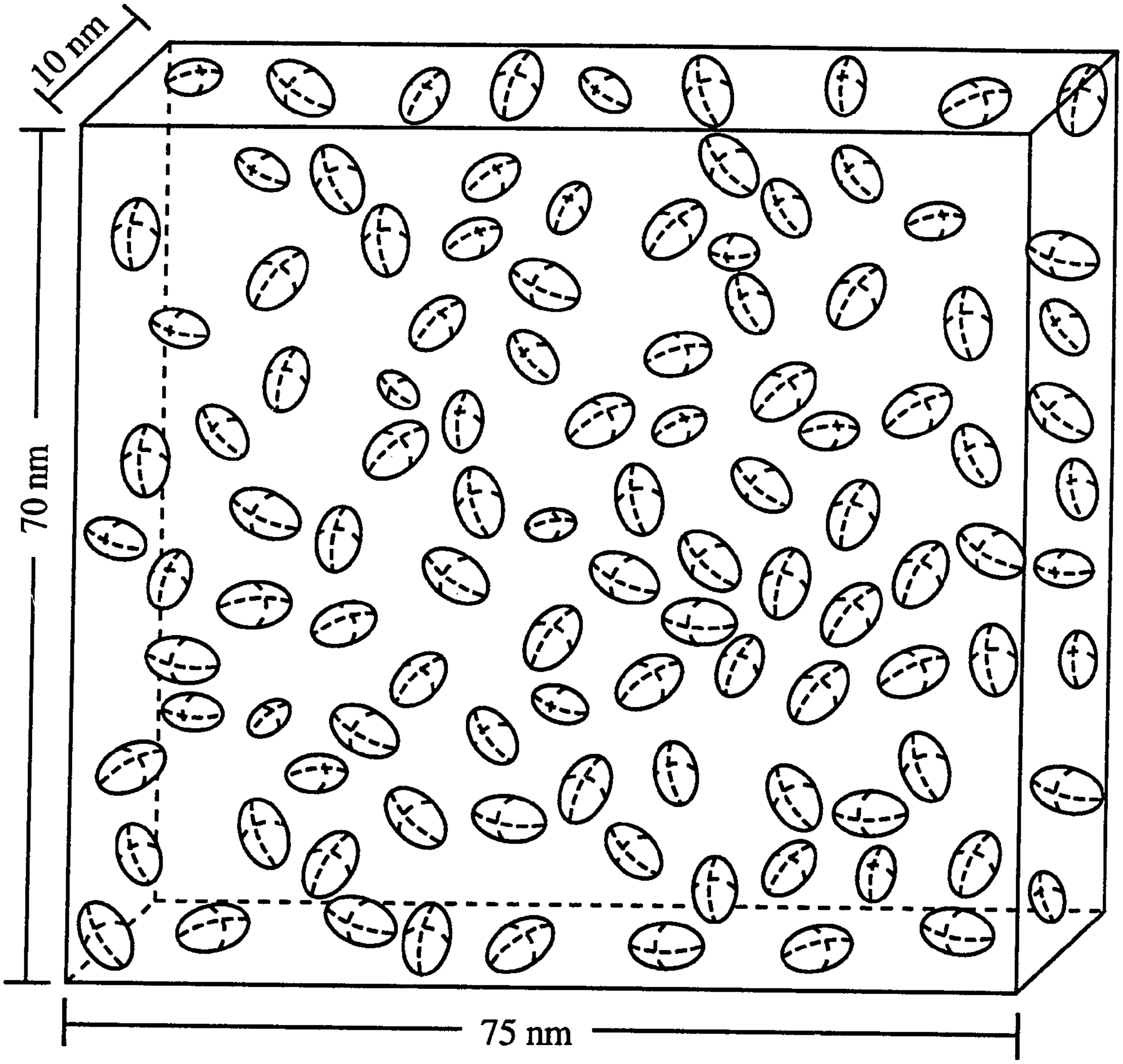
10 nm
70 nm
75 nm

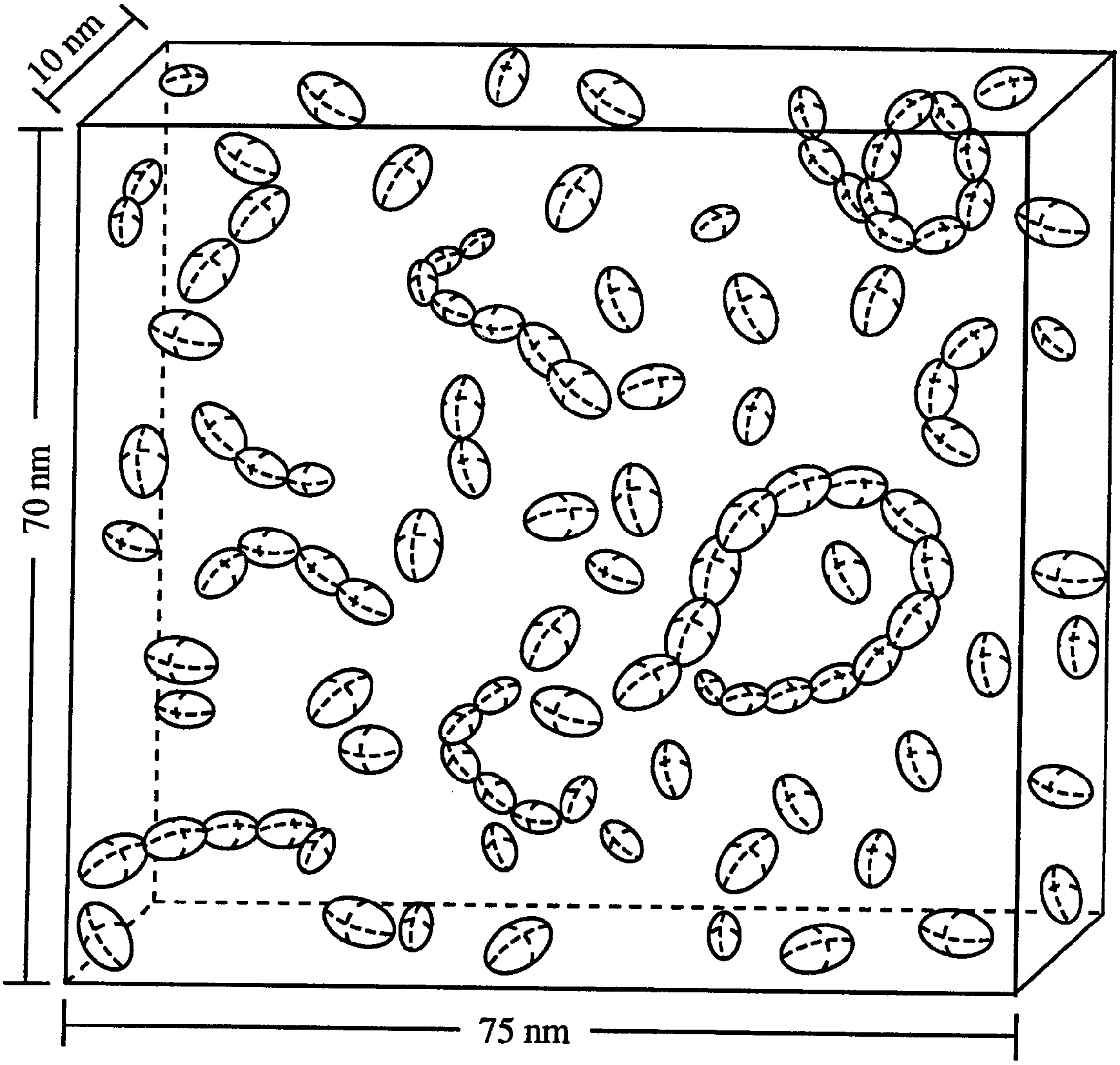
10 nm
70 nm
75 nm

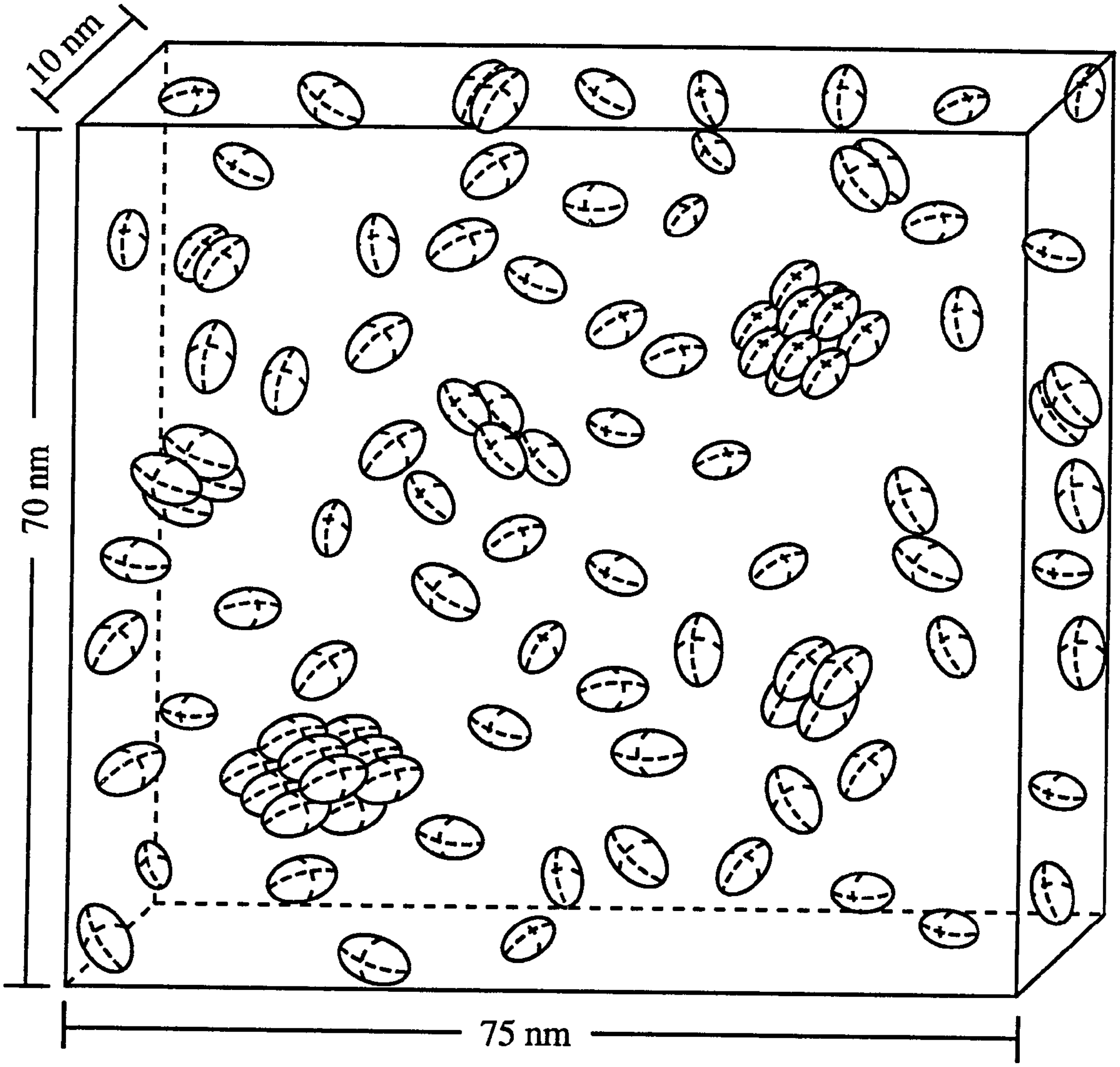
10 nm
70 nm
75 nm

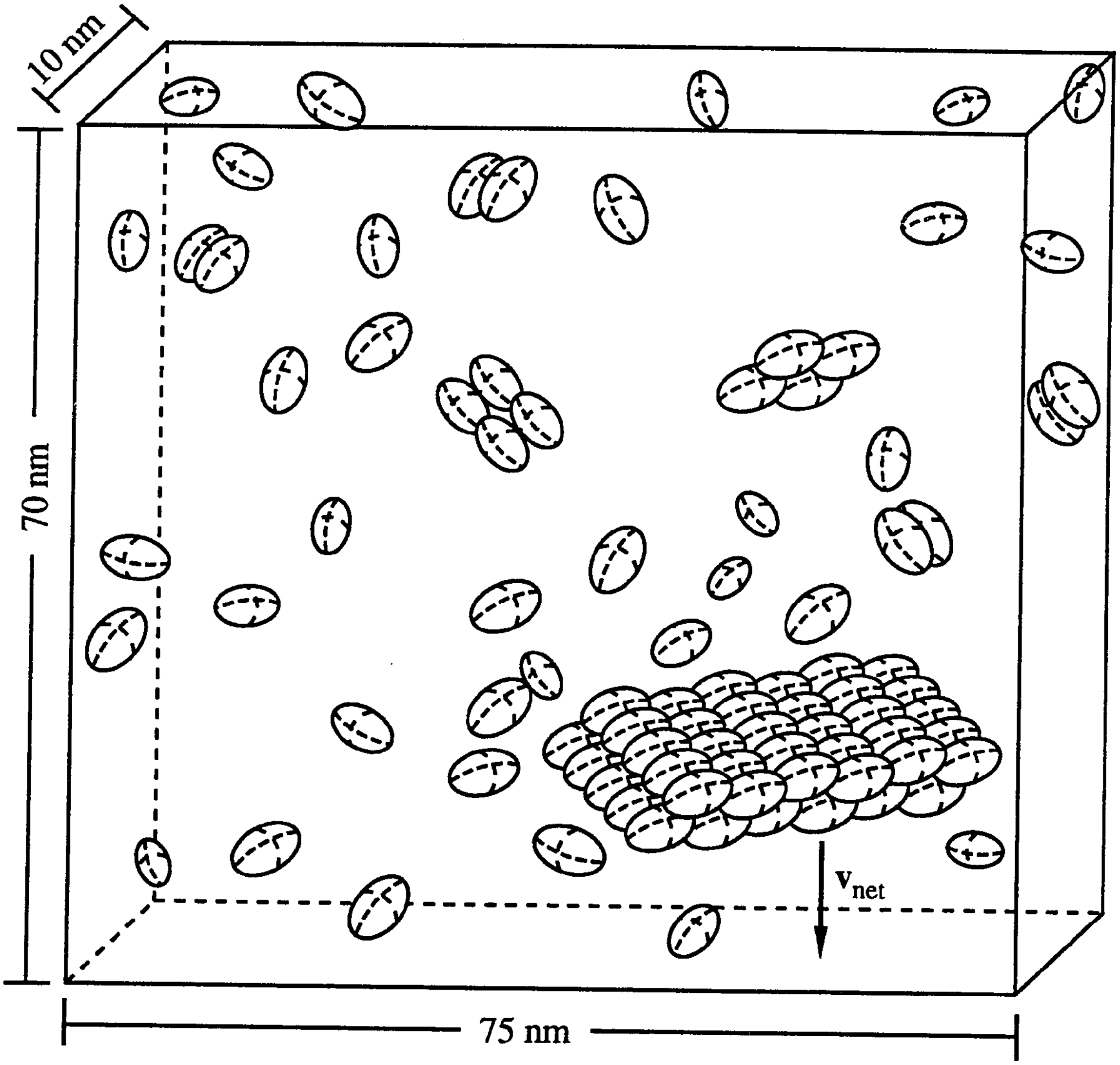
10 nm
70 nm
75 nm
v_{net}

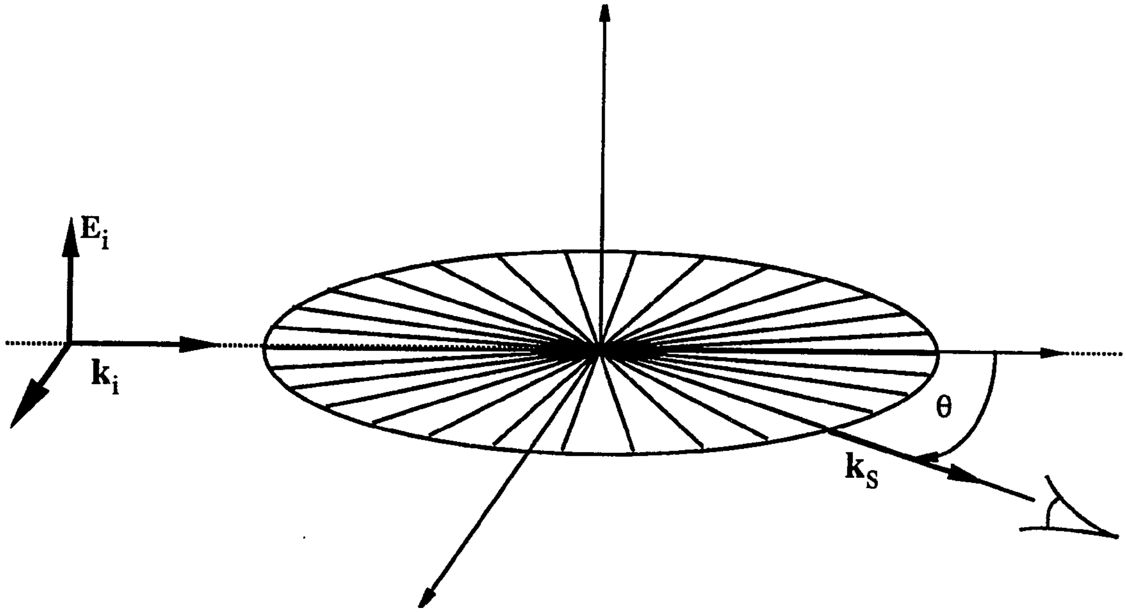

FIG. 4. The scattering plane is perpendicular to the direction of polarization of the incident beam. The scattering angle θ is measured with respect to the direction of incidence.

spectroscopy (PCS) which is discussed in the following section. This is followed by a brief section reviewing Rayleigh scattering and outlining an approximation to the classical Mie theory as applicable to this work.

1. Dynamic light scattering/photon correlation spectroscopy

a. The quasielastic event and the scattered electric field.

Illumination of the ensemble of N scatterers is accomplished by a focused, polarized laser beam, which may be well approximated[19] as a plane wave traveling in the direction of incidence with wave vector $\mathbf{k}_i$. A small detector in the scattering plane selects the direction of the scattered wave, which in the far field, may also be approximated by a plane wave $\mathbf{k}_s$. At a proper λ_0 (proper being one which does not excite the particle electronic states) the photon-particle collision would be perfectly elastic for a stationary particle, but the particle's motion causes a Doppler frequency shift in the scattered wave. Since in most situations the scatterers move at speeds less than that of sound, some six orders of magnitude less than the speed of light, the scattering event is said to be quasielastic. Consequently, the assumption of quasielastic light scattering is that

$$k_s = k_i = \frac{2\pi}{\lambda} \quad , \qquad (1)$$

where

$$\lambda = \frac{\lambda_0}{n} \quad . \qquad (2)$$

With this assumption the scattering vector $\mathbf{q}$ may be determined (see Fig. 5) such that

$$\mathbf{q} \equiv \mathbf{k}_i - \mathbf{k}_s \quad , \qquad (3)$$

and

$$q = \frac{4\pi}{\lambda} \sin\frac{\theta}{2} \quad . \qquad (4)$$

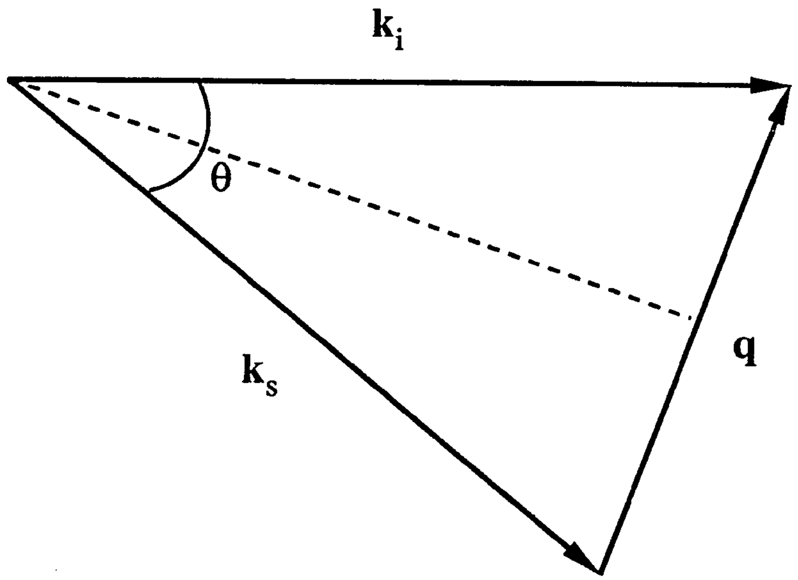

FIG. 5. The scattering vector is defined $\mathbf{q} \equiv \mathbf{k}_i - \mathbf{k}_s$. The scattering event is quasielastic, $k_s \approx k_i = 2\pi n/\lambda_0$. Therefore, $q = (4\pi n/\lambda_0)\sin(\theta/2)$.

The contribution to the magnitude of the scattered electric field by the moving ensemble constituent j with position $\mathbf{r}_j(t)$ (see Fig. 6) may be written with full generality as[87]:

$$E_j(q, t) = u_j(q, \mathbf{r}_j(t))\, e^{-i\omega_0 t} \quad , \tag{5}$$

where the complex amplitude u_j is given by:

$$u_j(q, \mathbf{r}_j(t)) = A_j\, e^{i\mathbf{q} \cdot \mathbf{r}_j(t)} \quad . \tag{6}$$

This leads to the scattered intensity:

$$I(q, t) = \left| \sum_{j=0}^{N} E_j(q, t) \right|^2 = \left| \sum_{j=0}^{N} u_j(q, \mathbf{r}_j(t)) \right|^2 \quad . \tag{7}$$

It is now clearly seen that the time dependence in I arises from $\mathbf{r}(t)$. The amplitude A_j depends on q if the particle dimensions are comparable to λ. This dependence is the subject of classical (or static) measurements and is addressed in a later section. There is also some temporal dependence for A_j due to particle rotation and to internal fluctuations, but this effect is neglected in this work because of the time scale over which these fluctuations occur.

b. Photon correlation spectroscopy. This work has utilized homodyne photon correlation to detect the temporal behavior of the scattered intensity. The intensity fluctuations represent all motion within the ensemble, but each type of motion has a characteristic relaxation time over which the intensity fluctuation, unique to that type of motion, will occur. The domain of the measured intensity autocorrelation function $G_2(\tau)$ (discussed below) selects the range of relaxation times which will contribute to $G_2(\tau)$ and thereby selects the type of motion being observed.

For example, the characteristic relaxation time of the fluctuations effected by the motion of the solvent molecules is much smaller than that of the fluctuations effected by the solute particles. A correlation time τ

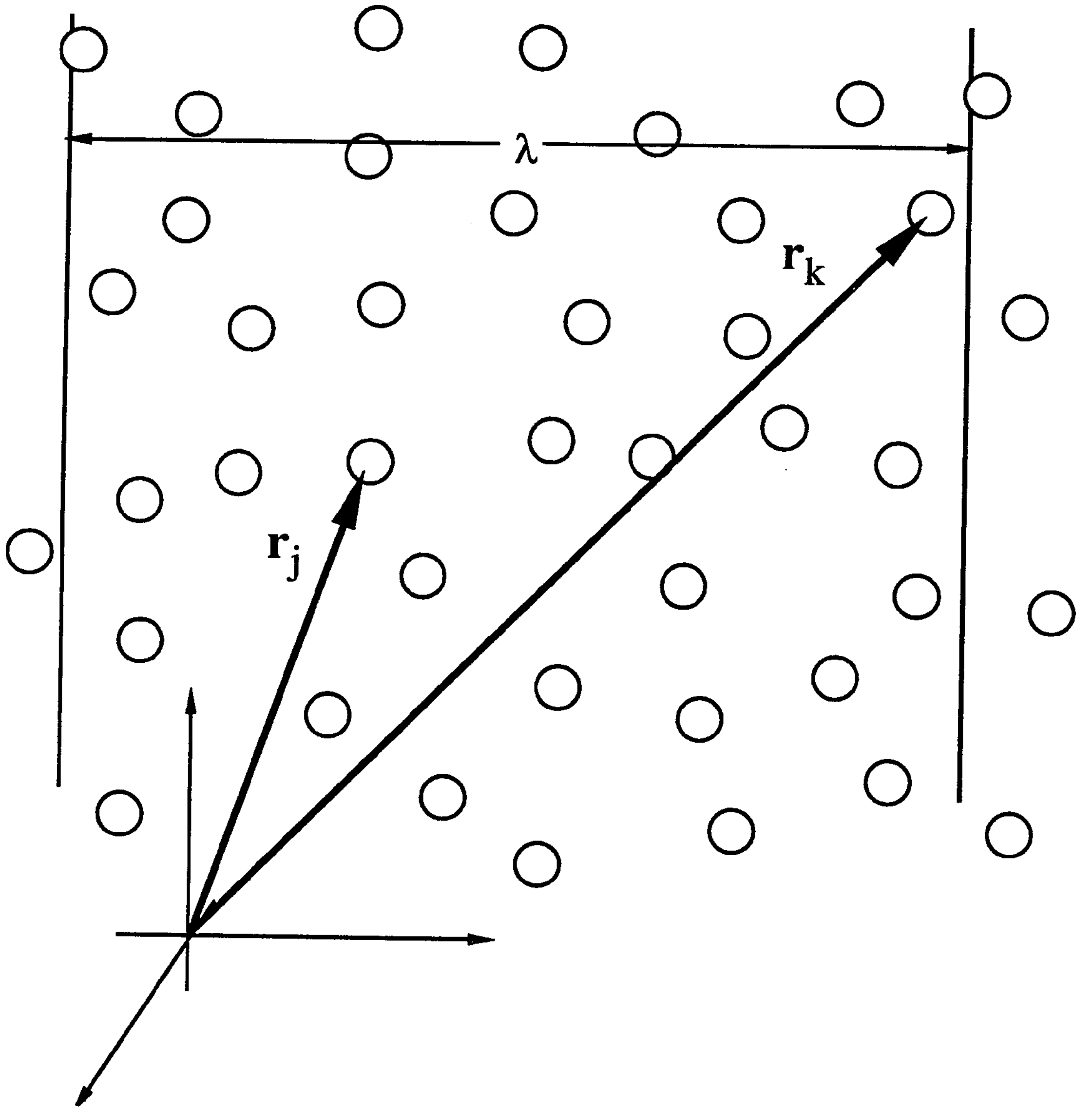

FIG. 6. The ideal scattering geometry: N spherically shaped, monodisperse, noninteracting, Rayleigh scatterers. The jth particle is positioned with vector $\mathbf{r}_j$.

smaller than those available with state of the art digital correlators would be required to measure these fluctuations, so they can be ignored. Large collective motion, such as that caused by mechanical vibration and convection, appears on a much larger time scale than is generally used in PCS, so they are also ignored.

In experiment, $\tau = m\Delta\tau$, where m is the correlator channel number and $\Delta\tau$ is the sample time, which may be varied. The domain of $G_2(\tau)$ is then determined by $\Delta\tau$ and the total channels available with the correlator. The time scales over which the correlations were made in this work dictate that the diffusive motion of the solute particles was the source of the observed fluctuations.

To demonstrate the relationship between the scattered field and the diffusive motion consider the amplitude correlation function $G_1(\tau)$:[87]

$$G_1(\tau) = \langle u(t)u^*(t+\tau)\rangle \quad , \qquad (8)$$

where

$$u(t) = \sum_{j=0}^{N} u_j(q, t) \qquad (9)$$

for constant q. In general, the amplitude correlation function is

$$G_1(\tau) = \left\langle \sum_{j=0}^{N} \sum_{k=0}^{N} A_j A_k e^{iq\cdot[r_j(t) - r_k(t+\tau)]} \right\rangle \quad , \qquad (10)$$

but upon declaring a monodisperse, independent system of particles, one obtains:

$$G_1(\tau) = N\langle |A|^2\rangle \langle e^{iq\cdot\Delta r(\tau)}\rangle \quad , \qquad (11)$$

where $\Delta \mathbf{r}(\tau) = \mathbf{r}(t) - \mathbf{r}(t+\tau)$ is the displacement of a constituent particle in time τ, and < > represents the ensemble or time average. The measurement is only sensitive to displacements parallel to **q**, and if **q** is taken to define the z direction then Eq. (11) becomes

$$G_1(\tau) = N\langle |A|^2\rangle \langle e^{iq\Delta z(\tau)}\rangle \quad . \qquad (12)$$

The values of each component of the displacements $\Delta \mathbf{r}_j$ take on a Gaussian distribution over the ensemble, and after Fourier transformation into q space of the Gaussian density function for the one dimensional displacement Δz Eq. (12) becomes:

$$G_1(\tau) = N\langle |A|^2\rangle e^{\frac{-q^2}{2}\langle \Delta z^2\rangle} \quad . \qquad (13)$$

The τ dependence for $<\Delta z^2>$ is provided by the famous result by Einstein[32] for the mean square displacement of a particle due to one dimensional diffusion:

$$\langle \Delta z^2\rangle = 2D_z\tau \quad , \qquad (14)$$

where D_z is the z average translational diffusion coefficient. Equation (14) is valid for τ values used in this work. Thus, using the usual notation of lower case g for normalized correlation functions, one may write the amplitude correlation function as:

$$g_1(\tau) = e^{-q^2D_z\tau} \quad . \qquad (15)$$

The above theoretical treatment of $G_1(\tau)$ illuminates the relationship to particle diffusion, but in practice, it is the intensity autocorrelation function $G_2(\tau)$ that is measured. The theoretical expression is

$$G_2(\tau) = \langle u(t)u^*(t)u(t+\tau)u^*(t+\tau)\rangle \quad , \qquad (16)$$

and the measurement is

$$G_2(\tau) = \langle n(t)n(t+\tau)\rangle \quad , \qquad (17)$$

where n is the number of photons counted during $\Delta\tau$, which is centered about τ. For large N, Eq. (17) simplifies to the Siegert relation[88]:

$$g_2(\tau) = \frac{G_2(\tau)}{\langle n\rangle^2} = 1 + |g_1(\tau)|^2 = 1 + \beta e^{-2q^2D_z\tau} \quad , \qquad (18)$$

where β represents contrast reduction in the signal due to a finite coherence area at the detector.

Interpretation of Eq. (18), which, recall, is for a monodisperse, independent solute ensemble, involves a linear regression to $\ln[g_2(\tau) - 1]$. The slope $(-2q^2D_z)$ represents the diffusive relaxation times ($\tau_D = 1/q^2D_z$, the value q^2D_z is often called Γ). The intercept ($\ln\beta$) determines β.

When the system of diffusing particles becomes more complex, as in the case of size polydispersity, $g_2(\tau)$ cannot be described by a single exponential decay. If, for example, the solute ensemble contains M species of particles each with diffusion coefficient D_{z_i}, then $g_2(\tau)$ becomes a squared sum of single exponentials[8]:

$$g_2(\tau) = 1 + \left| \sum_{i=1}^{M} A_i \, e^{-q^2 D_{z_i} \tau} \right|^2 \quad . \tag{19}$$

For this case, $\ln(\sqrt{g_2(\tau) - 1})$ may be expanded[55] into a power series in τ:

$$\ln(\sqrt{g_2(\tau) - 1}) = -C_1\tau + C_2\tau^2 - C_3\tau^3 + \ldots \quad . \tag{20}$$

The ith cumulant of the decaying exponential is C_i. The first cumulant C_1 (often denoted by $\overline{\Gamma}$) is related to an average diffusion coefficient:

$$C_1 = q^2 D_{avg} \quad . \tag{21}$$

The second, third, and fourth cumulants represent, respectively, the variance, skewness, and kurtosis of the size distribution. If the size distribution has a single peak[94] and the domain of $g_2(\tau)$ properly encompasses the diffusive relaxation times, then a cumulant expansion is a useful tool.

Multi-τ measurement is a capability of some correlators that increases the domain of $G_2(\tau)$ without losing resolution of the rapid fluctuations represented in $G_2(\tau \rightarrow 0)$. The BI 2030AT used in this work divides the channels into four equal sections and increases $\Delta\tau$ for each section by a user defined multiplier. For example, if in a 72 channel correlator a $2\mu s$ sample time was chosen with the multipliers 1, 2, and 3, then $\Delta\tau$ is $2\mu s$ for the first 16 channels, $2 \times 2^1\mu s$ for the second section of 16 channels, $2 \times 2^2\mu s$ for the third section, and $2 \times 2^3\mu s$ for the fourth section. The final eight channels are long delay channels which determine the measured baseline.

A fundamental problem in the analysis of size polydispersity by PCS is that interesting systems rarely distribute themselves ideally. Many methods have been introduced to deal with polydispersity,[22,44,67,69,75,92] but they cannot be detailed here.

Another nonideal aspect of the problem is that the diffusion is influenced by interparticle interactions.[13,43,77,78] Expansion of $g_1(q, \tau)$ into structure factors facilitates analysis of interactions.[78] A static component $S(q)$ and a dynamic component $F(q, \tau)$ contribute:

$$g_1(q, \tau) = \frac{F(q, \tau)}{S(q)} \quad . \tag{22}$$

The static structure factor contributes because the scattering centers are displaced from one another at any point in time:

$$S(q) = N^{-1} \sum_{j=1}^{N} \sum_{k=1}^{N} \left\langle e^{i\mathbf{q}\cdot(\mathbf{r}_j - \mathbf{r}_k)} \right\rangle \quad . \tag{23}$$

If $\mathbf{r}_j$ in no way depends on $\mathbf{r}_k$, that is to say the particles do not interact, then $\mathbf{r}$ is random, the average eliminates the cross terms, and

$$S(q) = 1 \quad . \tag{24}$$

The temporal dependence of $g_1(q, \tau)$ is reflected by $F(q, \tau)$:

$$F(q, \tau) = N^{-1} \sum_{j=1}^{N} \sum_{k=1}^{N} \left\langle e^{i\mathbf{q}\cdot[\mathbf{r}_j(t) - \mathbf{r}_k(t+\tau)]} \right\rangle \quad . \tag{25}$$

Again the cross terms vanish for non-interacting particles, and the self-dynamic structure factor is obtained:

$$F_s(q, \tau) = \left\langle e^{iq\cdot[r(t) - r(t+\tau)]} \right\rangle \quad . \tag{26}$$

Equations (22), (23), and (25) describe the general case. Equations (22), (24), and (26) describe the special case of non-interaction and yield Eq. (15). Consequently, the self-dynamic structure factor may be written as:

$$F_s(q, \tau) = e^{-D_0 q^2 \tau} \quad . \tag{27}$$

The free particle diffusion coefficient is D_0 and obeys the Stokes-Einstein relation[33]:

$$D_0 = \frac{k_B T}{f_0} \quad , \tag{28}$$

where

$$f_0 = 3\pi\eta d_0 \quad . \tag{29}$$

The free particle friction factor f_0 depends on the hydrodynamic diameter d_0 and the viscosity η. The Boltzman constant is k_B, and T is the absolute temperature.

The static structure factor may be written in terms of the measurement as :

$$S(q) = \frac{D_0}{D(q)} \quad . \tag{30}$$

Pusey and Tough[78] detail the q dependence in the presence of Coulombic interactions. They show $S(q \rightarrow \infty) = 1$, so free particle motion is observed at large q. As $q \rightarrow 0$ a collective motion is observed. The dynamic structure factor in the latter special case is:

$$F(q, \tau)|_{q \rightarrow 0} = S(q \rightarrow 0)\, e^{-D_c q^2 \tau} \quad , \tag{31}$$

where

$$S(q \rightarrow 0) = k_B T \left(\frac{\partial c_n}{\partial \pi}\right)_T \quad . \tag{32}$$

The number concentration is c_n, the osmotic pressure is π, and D_c is the collective diffusion coefficient measured in conventional gradient diffusion experiments. In this case D_c obeys the generalized Stokes-Einstein relation[8]:

$$D_c = \frac{\left(\frac{\partial \pi}{\partial c_n}\right)_T}{f} \quad . \tag{33}$$

The large q free particle diffusion observation and the low q collective diffusion observation are separated by a peak[13,23,77,78,86] in S(q) at $q_{max} = 2\pi/L$ where the mean center to center interparticle distance is $L = c_n^{-1/3}$.

In Eq. (33) both the thermodynamic term in the numerator and the friction factor in the denominator generally increase with increasing concentration. The interplay between these two terms[2,3,73] causes the behavior of D_c. In order to more easily understand this interplay consider the model of Anderson and Reed.[3] They present the overall dependence of D_c on the volume fraction ϕ to be:

$$D_c = D_0(1 + \Gamma\phi + O\phi^2) \ , \tag{34}$$

where

$$\Gamma = W - H \quad . \tag{35}$$

The term W (denoted by 8I in Ref. 3) represents the effect of long range conservative forces such as Coulombic forces. For repulsive forces $W > 0$ and for attractive forces $W < 0$. The term H (denoted by 8Λ in Ref. 3) represents the hydrodynamic forces and is always positive. The volume fraction differs from c_n by a positive constant, so Eq. (34) is often written to first order in terms of k_D instead of Γ:

$$D_c = D_0(1 + k_D c_n) \ . \tag{36}$$

With a single species of macromolecular ion as a solute component Coulombic forces would always be repulsive, and $W > 0$. In such a system if $k_D < 0$ then $H > W$. Thus, for single solute, ionic macromolecular solutions hydrodynamic interactions have overcome the Coulombic interactions when $k_D < 0$.

This section has outlined how particle diffusion manifests itself in the scattered intensity autocorrelation function as D_z. Discussion of some special cases showed that: (1) for non-interacting monodisperse systems, $D_z = D_0$; (2) for non-interacting, ideally distributed, polydisperse systems D_{avg} may be obtained from a cumulant expansion; and (3) for an interacting monodisperse system, D_c is measured in a low q scattering experiment and depends on the interactions. These cases provide insight into analysis of the data, but there is no proven analysis technique for interacting polydisperse systems. Supersaturated protein solutions definitely fit into this category.

"Apparent" diffusion coefficients used in this work were obtained either by a linear regression assuming Eq. (18) or by a second order cumulant fit assuming Eqs. (20) and (21). These values are heretofore denoted by D_{lin} and D_{2nd}, respectively. When temperature is varied it is often convenient to eliminate known temperature effects by computing an effective diameter d_{eff} by Eqs. (28) and (29) from D_{lin} or D_{2nd}.

2. Classical light scattering

Classical light scattering is a measure of average scattered intensity I vs scattering angle θ. The measured $I(\theta)$ is dependent on the size and concentration of particles in solution. Typical assessment of the data is done by measuring $I(\theta)$ vs c_n and extrapolating to 0 concentration. This is done by Zimm plot,[102] but for crystallizing systems, the concentration dependence is not accessible. Thus, the Zimm Plot is not used in this work and is not discussed. However, if particles aggregate within the scattering volume then one might discern a transition in $I(\theta)$ from a Rayleigh scattering pattern $[I(\theta) = \text{constant}]$ to a Mie scattering pattern $[I(\theta) \neq \text{constant}]$.

a. Rayleigh scattering. If the largest dimension of a spheroidal particle is small compared to λ then the induced electric field throughout the particle may be considered uniform at any given instant.[79] The charge separation within the polarizable material of the particle constitutes an effective dipole moment, **p**, that oscillates in time with the incident field. The time averaged intensity I of the energy reradiated into the scattering plane by a sphere of radius $< \lambda/20$ is[28,52]:

$$I(\theta) = I_0 = \frac{cp^2\pi^2}{2\varepsilon_0 R^2 \lambda^4} \quad . \tag{37}$$

Here c is the speed of light, ε_0 is the permittivity of free space, and R is the distance from the scattering center to the detector. In this instance, p is proportional to a^3, where a is the particle radius. This gives a^6 dependence to the intensity. It also depends on the dielectric qualities of the sphere, its surrounding medium, and the strength of the incident field (see Ref. 52). A classical experiment measures $I(\theta)$ and would yield a line with zero slope if performed on a system of N Rayleigh scatterers even if the N scatterers were polydisperse.

b. Mie scattering. A particle whose dimensions are comparable to λ does not experience a uniform electric field at any given time and does not reradiate uniformly into the scattering plane.[62] Wavefronts emitted by the coherent sources (the oscillating dipoles, quadrupoles,...etc.) within an individual scatterer interfere in the far field to cause a rather complex θ dependence for I. The name most often associated with analysis of this phenomena is Gustov Mie although many others have greatly contributed.[19] There is a unique I(θ) for each size scatterer, yet for a polydisperse distribution of Mie scatterers there are many particle size distributions that would yield the same I(θ). Therefore, detailed quantitative analysis of true polydisperse systems of Mie particles is not possible by classical light scattering alone.

The mathematics of the generalized Mie theory are quite involved, and the results require knowledge of the electric field within the confines of the scatterer before I(θ) can be determined. For this reason the current work utilizes the approximation to Mie theory presented by Drake and Gordon in Ref. 28. The approximation assumes the field within the scatterer to be a superposition of two plane waves, one traveling in the same direction as the incident wave and the other in the scattering direction. If, in accordance with Drake and Gordon, one defines

$$x = ka(1 + m^2 - 2m\cos\theta)^{1/2} \quad , \tag{38}$$

where m is the relative index of refraction between the solvent and the scatterer, then the resulting form for I(θ) follows from Maxwell's equations:

$$I(\theta) = I_0\left[\frac{3|j_1(x)|}{x} + x^{-3/2}\right] \quad , \tag{39}$$

where $j_1(x)$ is the first order spherical Bessel function of the first kind and I_0 is defined in Eq. (37).

Figure 7 demonstrates this approximation by showing, on an arbitrary scale, the scattered intensity (λ_0 = 488 nm) for three sizes of spherical scatterers labeled **A**, **B**, and **C**. Inspection of these curves shows the occurrence of local maxima and minima to be unique for each k*a*. Hence, these maxima and minima contain the scatterers' size information in a Mie scattering experiment. In this demonstration, if one were to assume hard sphere molecules of radius 2 nm (the approximate mean radius of lysozyme) packed into these volumes with a packing density of 0.76, then **A** would represent an aggregate j-mer with j ≈ 145 000, **B** would represent j ≈ 3 900 000, and **C** would represent j ≈ 18 000 000.

Figure 8 shows the scattered intensity on the same arbitrary scale for a distribution of these three sizes of Mie scatterers and demonstrates the effect of polydispersity on a classical measurement. The distribution is 1000 of aggregate **A**, 50 of aggregate **B**, and 1 of aggregate **C**. It is immediately obvious that Mie scattering information is obscured even by this simple discreet combination. Note, however, that the ratio of I measured at a forward angle to that measured at a rearward angle would maintain a value greater than 1.00 for any Mie distribution. Furthermore, the polydispersity guarantees that any two angles could be chosen for such a ratio. Therefore, I(30°)/I(90°), with a measured value exceeding 1.00, indicates the presence of a particle distribution with some constituents having dimensions larger ~λ/20.

It must here be pointed out that λ/20 is not a well defined boundary between the Rayleigh and Mie scattering regimes. There are various approximations[52] used in describing these transitional regimes, yet scatterers in these transitional regimes begin to exhibit forward scattering

FIG. 7. The Drake and Gordon[28] approximation of Eq. (39) is shown for ka = 2.0, 6.0, and 10.0 in (a), (b), and (c), respectively. Assuming hard sphere monomers of 2 nm radius packed into a spherical volume with a packing density of 0.76, an approximate j value for the aggregate j-mer is given. The intensity scale is arbitrary but kept constant, and $\lambda_0 = 488$ nm.

(a) For ka = 2.0, $j \approx$ 145 000.

(b) For ka = 6.0, $j \approx$ 3 900 000.

(c) For ka = 10.0, $j \approx$ 18 000 000.

(a)

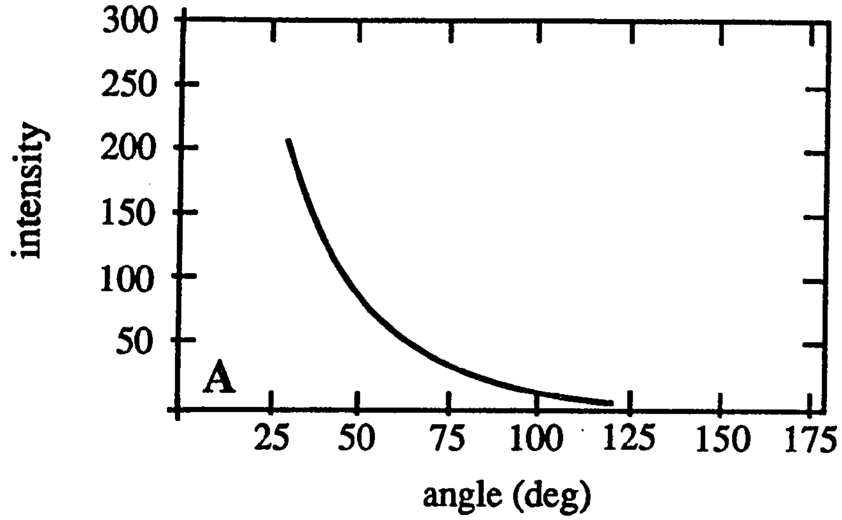
intensity
300
250
200
150
100
50
A
25
50
75
100
125
150
175
angle (deg)

(b)

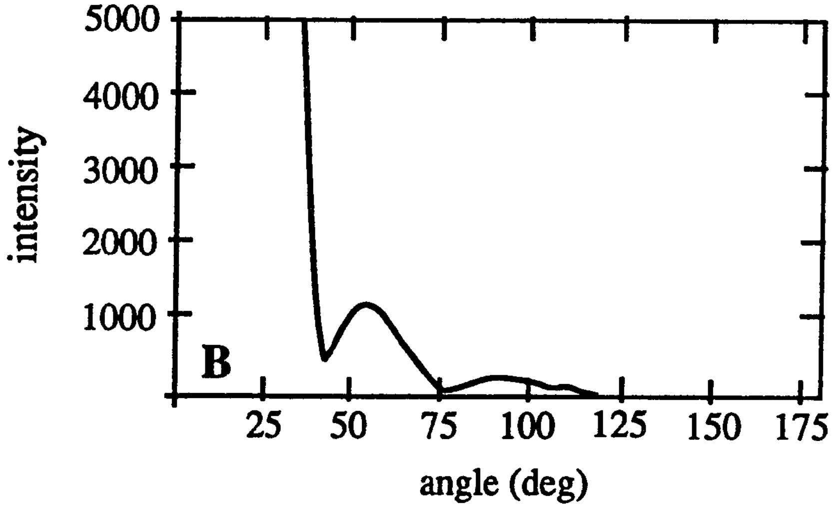
intensity
5000
4000
3000
2000
1000
B
25
50
75
100
125
150
175
angle (deg)

(c)

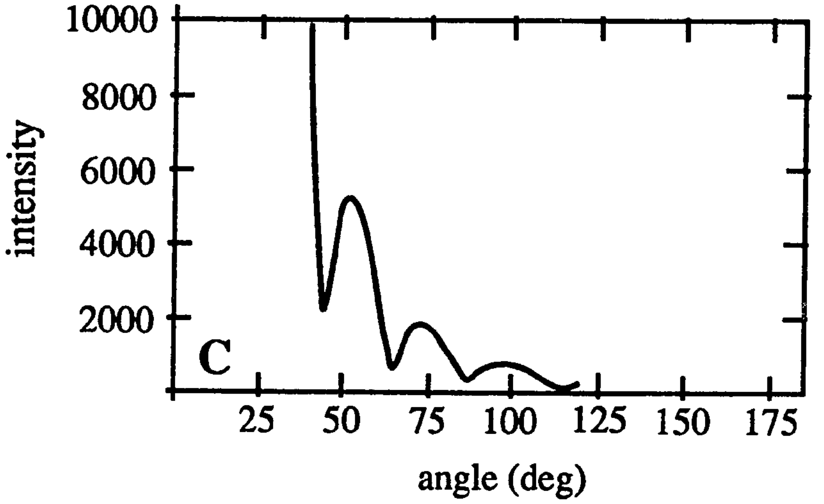
intensity
10000
8000
6000
4000
2000
C
25
50
75
100
125
150
175
angle (deg)

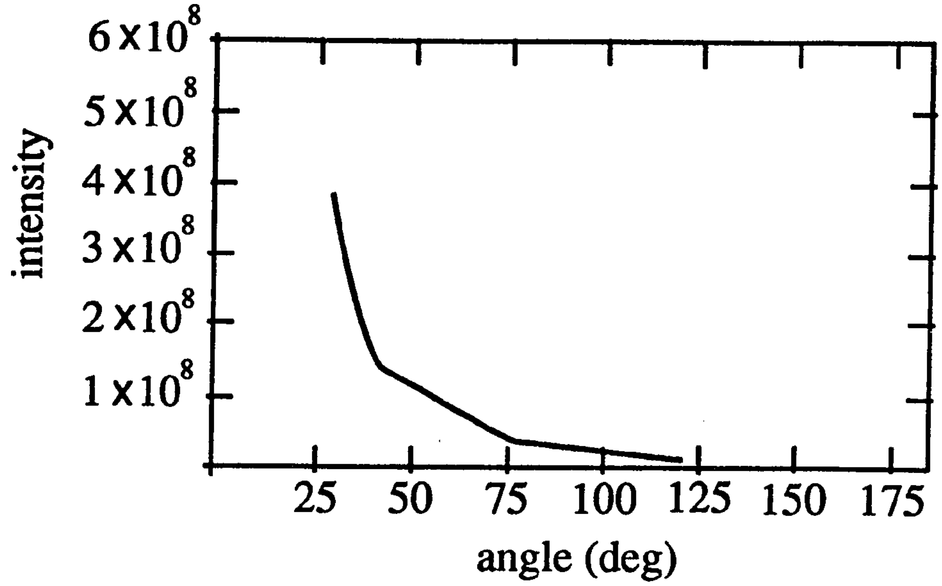

FIG. 8. The scattered intensity for a distribution of Mie scatterers is shown on the same arbitrary scale as Fig. 7. The distribution is 1000 particles of k*a* = 2, 50 particles of k*a* = 6, and 1 particle of k*a* = 10.

before they begin to exhibit the maxima and minima depicted in Fig 7. Thus, the premise is preserved.

Figure 9 shows the appearance and subsequent increase in forward scattering as the amplitude of the Mie distribution is increased in the presence of a background of monomers (spheres of radius 2 nm). Figure 9(a) shows the distribution embedded within 10^9 monomers. Figure 9(b) shows the appearance of forward scattering when the amplitude of the Mie distribution is multiplied by 5 (i.e., 5000 of **A** + 250 of **B** + 5 of **C**). Figure 9(c) and 9(d) show the increase in forward scattering as the amplitude is multiplied by 10 and 15, respectively.

Although a measurement of forward scattering from a polydisperse scattering system cannot provide quantitative information about the size distribution, it can be used to confirm the presence of Mie scatterers within the distribution.[11]

FIG. 9. The appearance and subsequent increase in forward scattering as predicted by the Drake and Gordon[28] approximation is shown in (a) - (d). The intensity scales are the same as in the two previous figures.

(a) The distribution of Fig. 8 is combined with 10^9 scatterers of k*a* = 0.07, the approximate k*a* for lysozyme monomers at λ_0 = 488 nm.

(b) The amplitude of the distribution is multiplied by 5. The number of monomers remains constant. Forward scattering appears.

(c) The amplitude of the distribution is multiplied by 10. Forward scattering increases.

(d) The amplitude of the distribution is multiplied by 15. Forward scattering continues to increase.

(a)

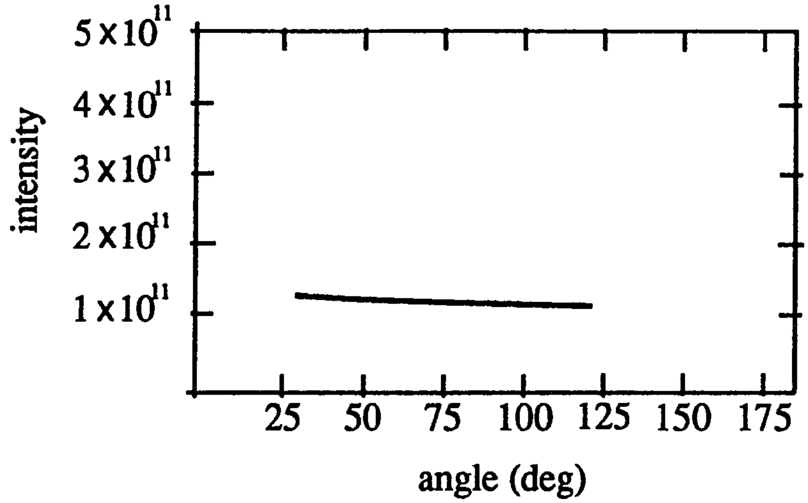
intensity
5 x 10^11
4 x 10^11
3 x 10^11
2 x 10^11
1 x 10^11
25
50
75
100
125
150
175
angle (deg)

(b)

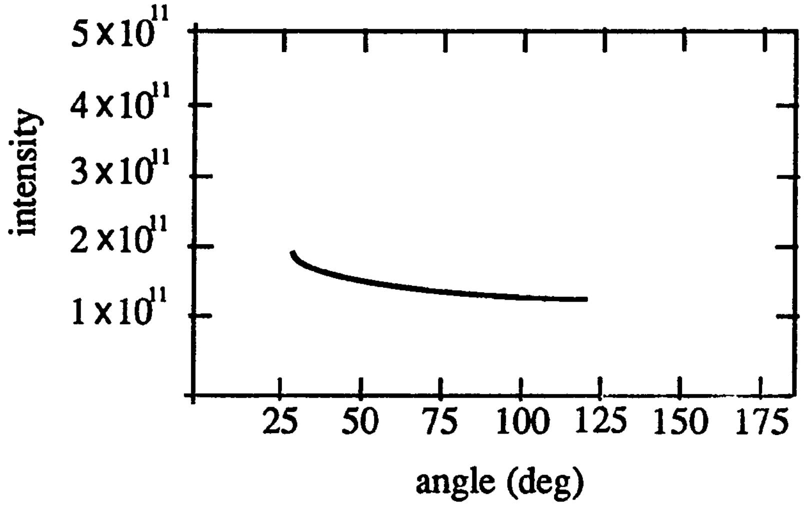
intensity
5 x 10^11
4 x 10^11
3 x 10^11
2 x 10^11
1 x 10^11
25
50
75
100
125
150
175
angle (deg)

(c)

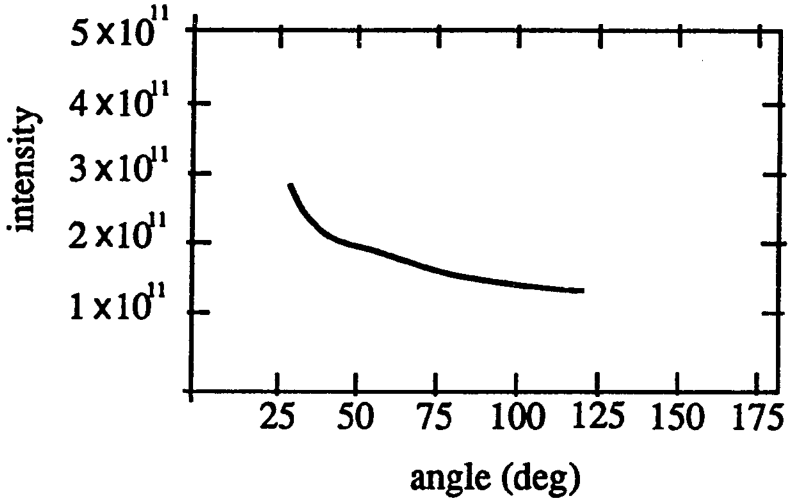
intensity
5 x10^11
4 x10^11
3 x10^11
2 x10^11
1 x10^11
25
50
75
100
125
150
175
angle (deg)

(d)

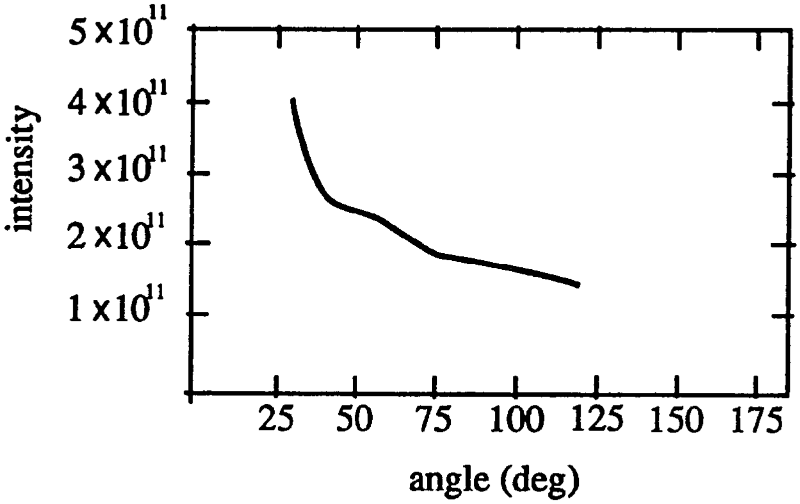
intensity
5 x10^11
4 x10^11
3 x10^11
2 x10^11
1 x10^11
25
50
75
100
125
150
175
angle (deg)

CHAPTER III

EXPERIMENTAL

Materials, equipment, and experimental procedures at UAH differed from those used at UAB, so this chapter will be divided accordingly. Data from lysozyme and insulin samples were collected at UAB, but at UAH, only lysozyme was used. The light scattering equipment produced by Brookhaven Instruments Corporation (BIC) proved the most useful and was available at both UAB and UAH. Thus, most data reported herein were collected using the Brookhaven instrument. However, some early classical measurements at UAB were made on lysozyme using the Dawn-B classical light scattering instrument from Wyatt Technologies Corporation.

A. UAB experimental

1. The Brookhaven instrument and peripherals

The most reliable data were collected using BIC scattering equipment and software. Utilized at UAB was the BI-2030 72 channel correlator controlled by an IBM compatible BIC AT personnel computer. The sample was centered in a quartz vat filled with the index matching fluid decahydranaphthalene (decalin). Water, circulated around the vat by a Neslab Endocal RTE-5DD circulating water bath, kept the index matching fluid, and hence the sample, at a constant temperature (± 0.1°C). When necessary, the index matching fluid was pumped through a 0.2 μm millipore filter by a BIC peristaltic pump. The vat was at the center of the BI-200SM (stepping motor) goniometer assembly which stepped the detection optics and photomultiplier tube to the various scattering angles accurately. Based on Raleigh scattering from the index matching fluid the goniometer alignment for all measurements was to within 2% over the angular range used. The Spectra Physics model 2020 Ar^+ laser tuned to the 488 nm line was used as the illuminating source. The experimental setup is shown as Fig. 10.

Light scattering measurement sessions began after turbulence due to injection of the sample subsided. Sessions consisted of both classical and correlation measurements and lasted between 20 and 40 minutes depending on the sample.

Intensity measurements were made for $30° \leq \theta \leq 120°$ in 10° increments and were corrected for dark counts and correlator dead time. At each of the 10 angles the average of five measurements, each 2 seconds in duration, was taken and was multiplied by $\sin\theta$ to account for the changes in scattering volume that are encountered when changing θ. It is this corrected value of intensity times $\sin\theta$ that is heretofore called I.

Correlation functions were obtained at a single angle but utilized various sample times including multi-τ. The $\Delta\tau$ were determined as soon as turbulence subsided and usually varied slightly from sample condition to sample condition, but at a particular condition the necessary times were consistent. For multi-τ measurements the multipliers were 1, 2, and 3. Reported values at a particular time were obtained by averaging the measurements during that session. Most of the UAB studies using the Brookhaven instrument utilized temperature as a dynamic parameter to induce crystallization. For these, the temperature was lowered at the end of each session, and about 15 minutes were always allowed for stabilization before a new session began.

FIG. 10.   The Brookhaven setup at UAB.

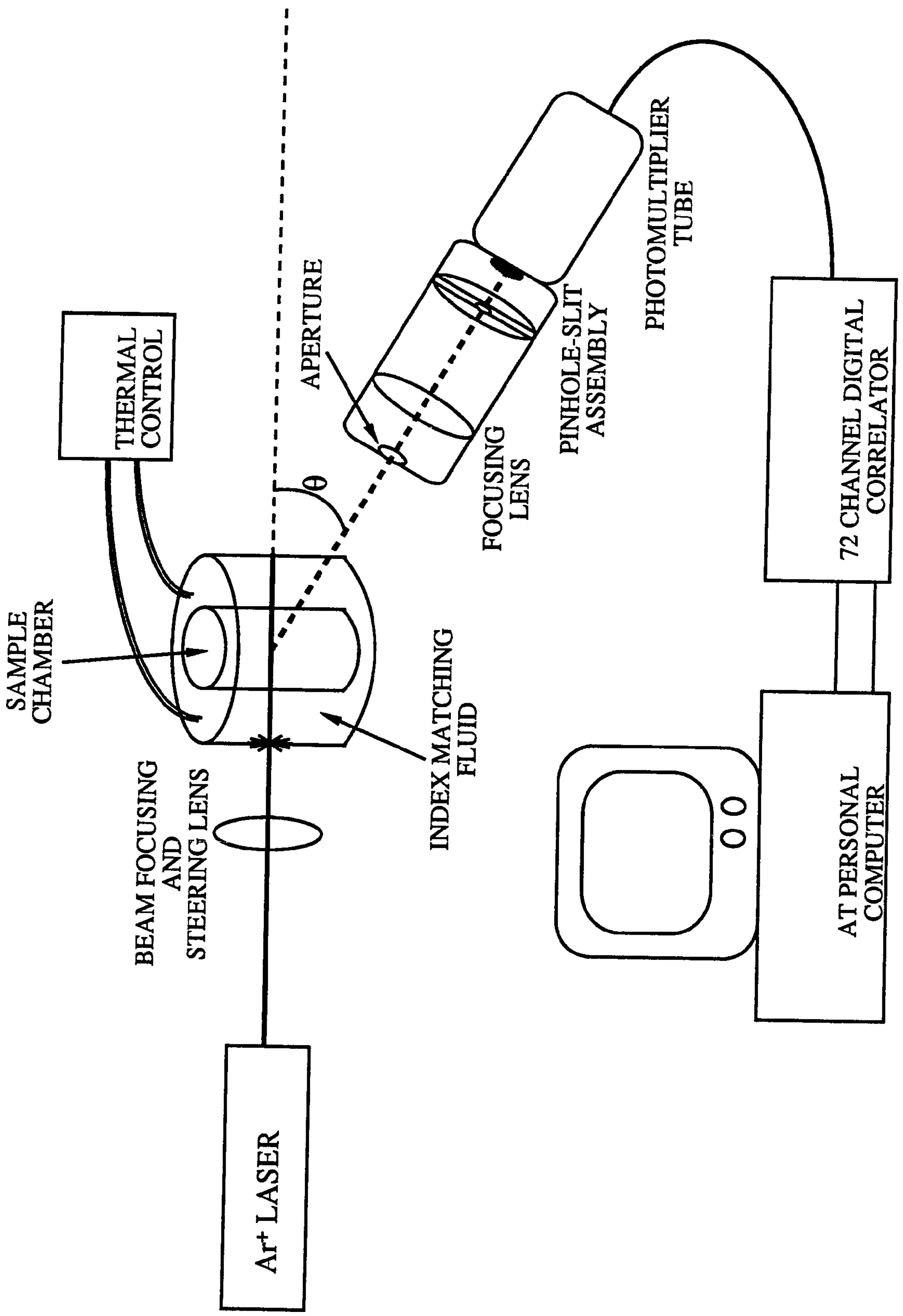
Ar+ LASER
BEAM FOCUSING AND STEERING LENS
SAMPLE CHAMBER
THERMAL CONTROL
INDEX MATCHING FLUID
θ
APERTURE
FOCUSING LENS
PINHOLE-SLIT ASSEMBLY
PHOTOMULTIPLIER TUBE
72 CHANNEL DIGITAL CORRELATOR
AT PERSONAL COMPUTER

2. The Wyatt instrument

Early light scattering measurements on lysozyme included use of the Wyatt Dawn B classical light scattering instrument. The instrument was a self-contained unit consisting of a 10 mw HeNe laser ($\lambda_0 = 632.8$ nm) and of a sample chamber surrounded by a detector array of 15 photodiodes whose angular positions for $20° < \theta < 130°$ are equidistant in $\sin(\theta/2)$. The sample chamber was not temperature controlled. The detector output was interfaced to the BIC AT personal computer via the Data Translation DT2801A 16 channel 12 bit A/D multiplexer and processed by the Dawn B software.

For normalization, twice filtered optical grade toluene was used as a Rayleigh scatterer. Normalization to 90° such that $I(\theta)/I(90°) \equiv 1$ was arbitrary. The light scattered by the solvent (a predetermined amount of NaCl in acetate buffer) was measured after normalization and was subtracted automatically by the Dawn B software during the measurements.

Data from the Dawn B were collected over periods ranging from one day to one week depending on the sample. About 10 measurements per hour were typically made during the first two to three hours. The intervals were gradually lengthened until, finally, measurements were taken about three to eight hours apart. The signals from each of the 15 photodiodes were read 100 times for each measurement and the lowest 10 values were averaged and reported. This disallowed large bursts of intensity caused by any dust or contaminate within the sample.

3. Lysozyme

All water, purified and ultrafiltered by the Millipore Milli-Q system, was deionized to > 16 MΩ. Hen egg white lysozyme (MW ≈ 14 400 Daltons) was purchased from Boehringer Mannheim Biochemicals and dissolved at room temperature in 0.05 M acetate buffer which was prepared at pH 4.5 by calculated mixture of preprepared stock solutions of 0.2M acetic acid and 0.2M sodium acetate. To remove any salts remaining from isolation of the protein, the solution was dialyzed (Spectra/Por 8000 MW cutoff) at 4°C for 36 hours against the acetate buffer with the reservoir being changed every six to eight hours. At 4°C the solution was removed from the dialysis bag by glass transfer pipette, placed in microcentrifuge tubes, and centrifuged at 15 000 RPM for 30 minutes. These stock lysozyme solutions were stored at 4°C until use, but an aliquot was removed for absorption measurements at room temperature. The concentration c was calculated using Beer's law ($A = \varepsilon l c$) from UV ($\lambda = 280$ nm) absorbance (A) measurements using the Beckman DU-50 spectrophotometer. The molecular absorptivity reported by Sophianopoulas et al.[90] ($\varepsilon^{1\%}_{280\text{ nm}} = 26.4$) was used. The optical path length l of the square cuvettes used was 1 cm. The concentration of the stock was recorded as the average of four absorbance measurements and was usually between 60 and 100 mg/ml.

Dilutions were made given: c_i^{lys}, the lysozyme stock solution concentration; V_f, the desired final sample volume, usually 5 ml; c_f^{lys}, the desired final lysozyme concentration; and c_f^{NaCl}, the final NaCl concentration. A sample calculation follows:

If the stock lysozyme was 70 mg/ml and 5 ml of 30 mg/ml lysozyme and 3% NaCl at pH 4.5 was required, then

$$c_i^{NaCl} = \frac{c_f^{NaCl}}{1 - \frac{c_f^{lys}}{c_i^{lys}}} = \frac{3\%}{1 - \frac{30}{70}} = 5.25\% \quad ,$$

and

$$V_i^{lys} = \frac{c_f^{lys}}{c_i^{lys}} V_f = \left(\frac{30}{70}\right) 5 \text{ ml} = 2.14 \text{ ml} \quad ,$$

and

$$V_i^{NaCl} = V_f - V_i^{lys} = 5 \text{ ml} - 2.14 \text{ ml} = 2.86 \text{ ml} \quad .$$

Therefore, 2.86 ml of a 5.25% NaCl solution in acetate buffer at pH 4.5 would be slowly added to 2.14 ml of stock lysozyme, and the solution parameters reported as 30 mg/ml lysozyme, 3% NaCl at pH 4.5.

If the initial temperature T_{init} was to be different from room temperature, all solutions and containers were brought to T_{init} in a water bath before mixing. After mixing, the solution was gently vortexed and filtered (0.2 μm Millipore) into the scattering cuvette which was, if necessary, held at T_{init} in the BIC scattering chamber. Unfortunately, the temperature could not be controlled during vortexing and transport to the cuvette, a total time of about one or two minutes. However, it was the mixing stage of preparation that affected the final formation of PRAGG's or of CRAGG's. If the NaCl solution was added too quickly or if the mixture was not vortexed thoroughly, PRAGG's would result, seemingly regardless of sample parameters. It was discovered later that gentle stirring (if necessary on a temperature controlled stir plate) of the sample during addition of NaCl would consistently yield CRAGG's.

4. Protamine insulin

The protocol for the temperature dependent crystallization of insulin was taken from Krayenbuhl and Rosenberg.[56] A phosphate buffer (0.01M Na_2HPO_4, 0.5M NaCl, 0.3% m-cresol, pH 6.5) and a 1% solution of salmine sulfate (grade II from salmon, Sigma Chemical Corp.) in water were prepared. An amount ranging from 5 to 10 mg of crystalline bovine insulin (0.5% zinc content, Sigma Chemical Corp.) was weighed on the Mettler AE240 precision balance and diluted to 1.60 mg/ml with the phosphate buffer. To 50 parts of this suspension was added 1 part of the 1% salmine sulfate solution. The resulting suspension was vortexed and incubated in a water bath at 60°C for one hour. At room temperature the samples were centrifuged at 15 000 RPM for four minutes. The supernatant was removed by glass pipette and quickly returned to 60°C. Aliquots were removed and checked microscopically for crystals. The sample was then ready for crystallization which was induced as the temperature was lowered. For the light scattering experiments, the solutions were transported at 60°C to the laser lab and filtered (0.2 μm Millipore) into the scattering cuvette which was held at T_{init} = 40°C.

It should be noted that the exact concentration at which the insulin crystallized was not known. Due to the centrifugation step, the final concentration was dependent on how much insulin went into solution during the incubation period.

B. UAH experimental

1. The Brookhaven instrument and peripherals

The Brookhaven equipment at UAH was similar to that at UAB. The set up is shown as Fig. 11. The BI-200SM goniometer was used with a BI-2030AT 136 channel correlator. Either the 647.1 nm or the 413.6 nm line of a Spectra Physics 2020/11 krypton laser was used. The goniometer was modified by mounting a Glan-Thompson prism to intercept the incident beam immediately before the sample chamber. A half-wave plate was used to rotate the plane of polarization ahead of the prism to attenuate the beam and to provide a depolarized component when desired. A non-polarizing beam splitter was placed up beam from the half wave plate

FIG. 11. The Brookhaven setup at UAH.

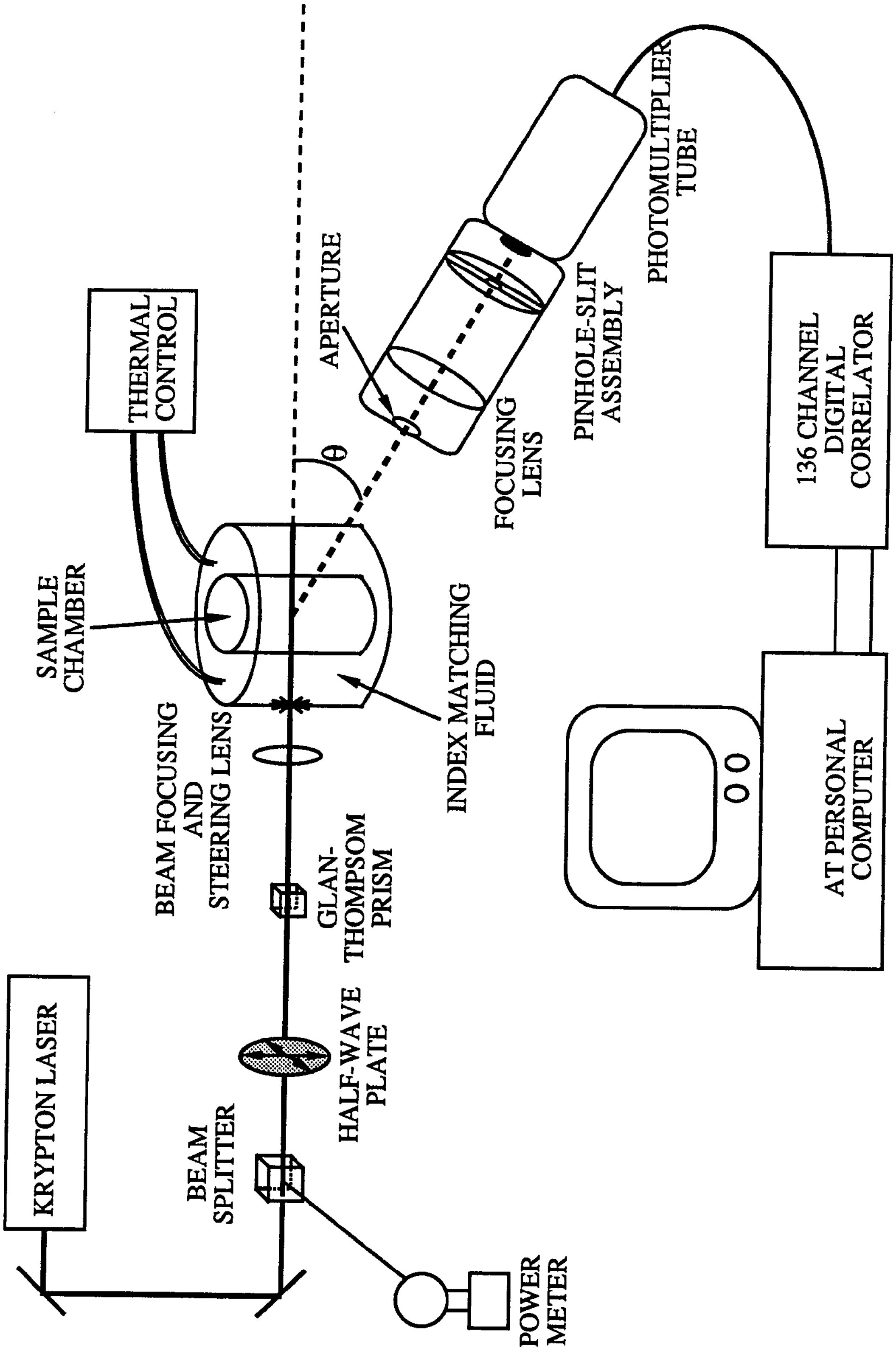
KRYPTON LASER
BEAM SPLITTER
POWER METER
HALF-WAVE PLATE
GLAN-THOMPSOM PRISM
BEAM FOCUSING AND STEERING LENS
SAMPLE CHAMBER
INDEX MATCHING FLUID
THERMAL CONTROL
θ
APERTURE
FOCUSING LENS
PINHOLE-SLIT ASSEMBLY
PHOTOMULTIPLIER TUBE
136 CHANNEL DIGITAL CORRELATOR
AT PERSONAL COMPUTER

to provide a signal for monitoring the incident intensity with a Newport model 815 digital power meter. The sample was contained in a 12 mm diameter cuvette which was immersed in the decalin. The temperature of the decalin and hence the sample was controlled by a Neslab RTE-100 circulating thermostat. The temperature of the decalin very near the sample was measured using a chromel-alumel thermocouple and a Fluke 2190A digital thermometer, which was calibrated at the ice point. Prior to a measurement the decalin was circulated by a small gear pump through a 0.2 μm millipore filter to remove contaminants. Based on Rayleigh scattering from the decalin the alignment of the goniometer was within 1% over the range used in the experiments. The incident beam was always polarized vertically.

During the study of isothermal crystallization the temperature of the decalin was held at 11°C and the sample, which was undersaturated at room temperature, was immersed. Separate experimentation with the thermocouple placed directly into the center of the sample showed equilibration to 11°C within four minutes. For these measurements $\lambda_0 = 647.1$ nm. Data collection began immediately and continued by means of the BIC control program for about 30 hours. The correlation functions were taken sequentially at $\theta = 90°$ and two smaller angles. If a baseline could not be calculated to within 1% of the measured value the correlation function was discarded. The RMS counting error is reported for D_{lin} and D_{2nd}.

For the concentration and temperature dependence of the low ionic strength (monomeric) solutions, five correlation functions were measured for each condition at 11 angles such that $20° < \theta < 150°$. To increase q for this work, the laser was tuned to the 413.6 nm line. Each sample was prepared at pH 4.5 with an ionic strength of 0.8% NaCl. At a particular lysozyme concentration measurements were made for 11°C $\leq T \leq$ 35°C. The average of the five values of D_{lin} or D_{2nd} are reported, and for these multiple measurements of stable solutions, the 95% confidence limit is reported as an error range.

2. Lysozyme

Lysozyme chloride from chicken egg white (MW ≈ 14 400 Daltons) was purchased from Sigma Chemical Co. and dissolved in deionized water (> 18MΩ; Millipore, Milli-RO system). This solution was first dialyzed (Spectra/Por 8000 MW cutoff) against DI water. Two water changes in 20 hours were sufficient to remove any remaining salts as had been shown by previous experiments using a Na^+ probe and NaCl solutions of known concentrations. The solution was then dialyzed against 0.05M acetate buffer, pH 4.5, for 60 hours with the reservoir being changed periodically. Absorbance readings of the discarded buffer ensured that the dialysis membrane was not compromised. The dialyzed protein solution was filtered (Nalgene, 0.2 μm) and was concentrated (Amicon ultrafiltration device) to approximately 110 mg/ml. Concentration of the solution raised the pH slightly, but no corrections were made. This solution was stored at 4°C and used as stock.

The 0.05M acetate buffer was prepared in advance at pH 4.50 with 0.01% sodium azide to inhibit microbial growth. A weighed (Mettler AE 200 precision balance) amount of NaCl was dissolved in buffer to make the NaCl stock. These solutions were pH corrected, if necessary, with 0.2M acetic acid or 0.2M sodium acetate and were stored at 4°C. Measurements of pH were made with the Orion SA 520 pH meter with an 8103 Ross combination semi-micro electrode.

Samples at the desired concentrations were prepared at room temperature by adding calculated volumes of the protein, buffer, and NaCl stock solutions. Volume calculations were the same as the example given in section A.3 of this chapter. Eppendorf pipettes were used to deliver these volumes. The NaCl was added last, and the sample was immediately and thoroughly mixed by vortexing. The sample was centrifuged at 9000 rpm in a Savant HSC 10K high speed centrifuge. The supernatant was drawn off, pH corrected, and filtered (0.2 μm Acrodisc nonprotein binding syringe filter) into sterile scattering cuvettes.

A small portion of the sample was used for absorption measurements. The concentration was calculated by Beer's law from UV (λ = 280 nm) absorbance measurements using the Beckman DU-64 spectrophotometer. The molecular absorptivity of Sophianopoulas[90] ($\varepsilon^{1\%}_{280\text{ nm}} = 26.4$) was again used. The optical path length was 1 cm.

The calibration of the Eppendorf pipettes was checked during the course of the experiments using a microbalance as well as absorbance standards. They were found to be accurate to within tolerances given by the factory. However, the larger volume pipettes were considerably more accurate than the smaller volumes, and this led to an increase in the sampling volumes for the absorbance readings. Multiple measurements (three or four) also increased confidence in the determined concentrations although concentration error is still suspected of being the largest contributor to overall experimental error.

CHAPTER IV

RESULTS

A. UAB results

1. Lysozyme

An absorption scan of lysozyme (see Fig. 12) showed no absorbance for λ > 350 nm so laser light scattering proceeded. Initial experiments utilized the Wyatt Dawn-B instrument. Classical light scattering is typically performed on dilute solutions, so these experiments attempted crystallization at low lysozyme concentrations of 5 to 10 mg/ml. Three types of behavior were observed with the Wyatt unit:

(1) At NaCl concentrations greater than 10% w/v the sample rapidly became turbid and the scattered intensity was too great to measure.

(2) At NaCl concentrations less than 5% no changes in scattering behavior were observed. A Rayleigh profile persisted for up to two weeks with no measurable increase in absolute intensity.

(3) Between 5% and 10% NaCl an interesting phenomena was observed as demonstrated by Fig. 13, which shows an increase in absolute intensity over time as well as an increase in forward scattering.

For all these samples, dilution of the stock and the measurements were done at room temperature. Type (1) samples resulted in a white precipitate covering the bottom of the scattering vial after 6 to 24 hours. Microscopic examination showed orthorhombic crystals protruding from

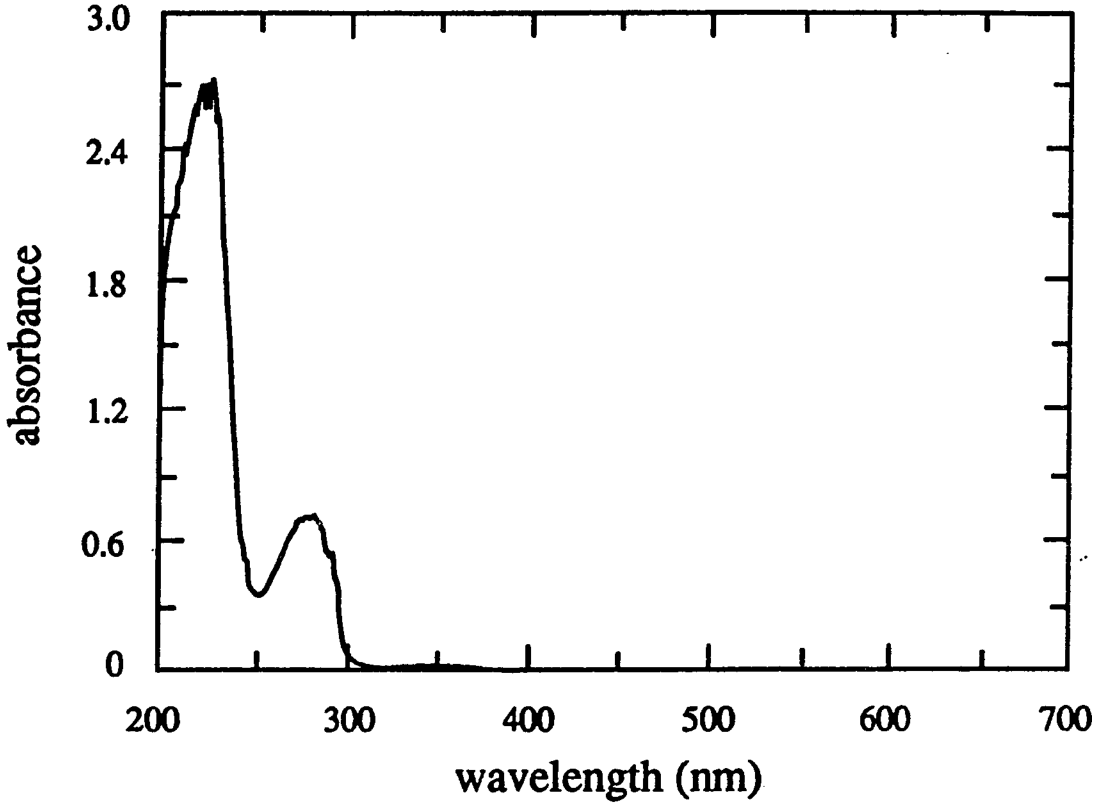

FIG. 12. An absorbance scan of lysozyme at room temperature: c = 18.5 mg/ml, 0.8% NaCl, and pH 4.5. The dilution was 10 µl/ml.

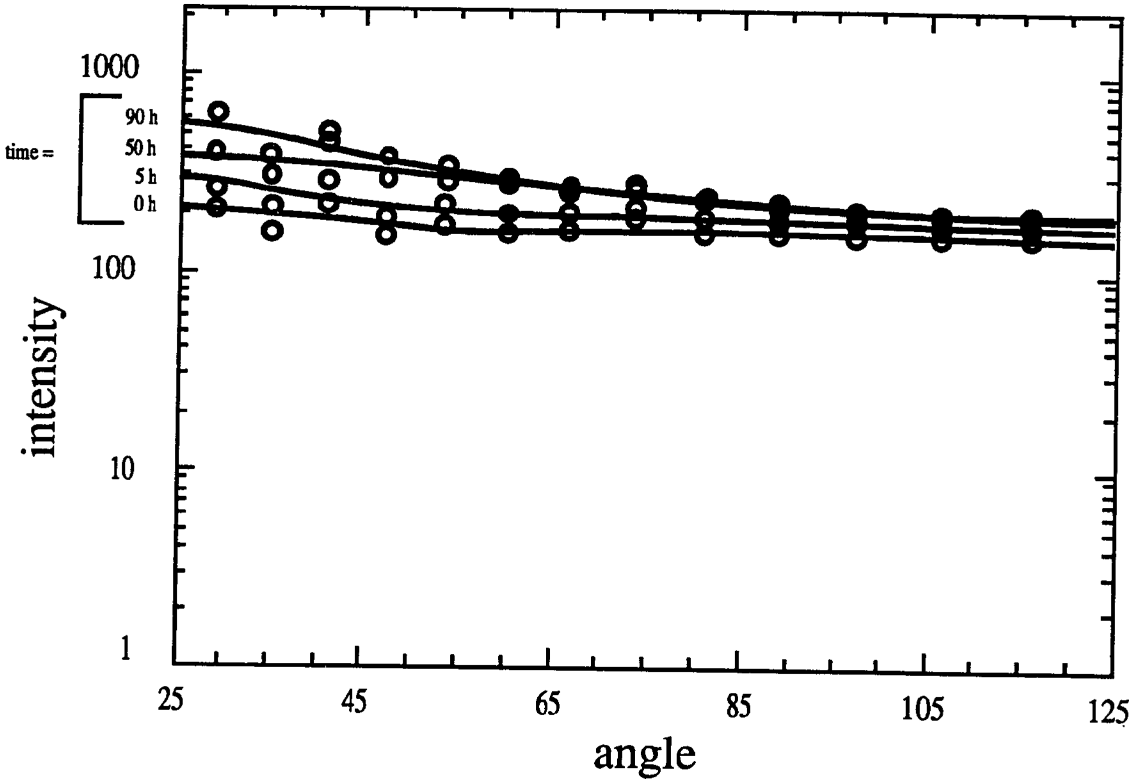

FIG. 13. Intensity vs angle on a logarithmic scale for 5 mg/ml lysozyme at pH 4.4 and 10% NaCl. The data were collected with the Wyatt Dawn-B at room temperature. The data are shown at four times (noted beside the intensity axis) during the experiment and are fit to fourth order Chebyshev polynomials.

"snowballs" of amorphous precipitate. Type (2) samples showed no visible results after one month. Type (3) samples also showed nothing at 4x magnification even after one month.

Dawn-B measurements were discontinued in favor of the Brookhaven instrument which offered a thermally controlled sample environment, as well as PCS capability. Before the lysozyme concentration was increased, data on type (3) samples were collected isothermally at 30°C. Figure 14 shows an increase in forward scattering over time. This sample will be referenced later as L1. As discussed earlier, a measure of forward scattering is the ratio of the absolute intensity at 30° I(30) to that at 90° I(90). For convenience the ratio I(30)/I(90) is denoted by FS. A plot of FS and d_{eff} over time for L1 is shown as Fig. 15. The correlation functions were obtained (for $\lambda_0 = 488$ nm, $q = 11.73 \times 10^4$ cm^{-1}) at $\theta = 40°$, and d_{eff} was calculated from D_{2nd} using Eqs. (28) and (29). Results from another sample L2 at these conditions are shown as Fig. 16. Posterior microscopic examination of L1 and L2 at 10x magnification revealed no precipitate.

Tetragonal crystals formed in properly prepared solutions when the ionic strength was lowered and the lysozyme concentration was increased. Results from tetragonal sample L3 are shown as Fig. 17. The lysozyme concentration was 16 mg/ml, NaCl was 3.0%, pH was 4.4, and the temperature was dropped from 35°C to 15°C in one step. The sample equilibrated to 15°C within 15 minutes. Classical measurements show little forward scattering [see Fig. 17(a)].

Measurement of another tetragonal sample L4, the same as L3 but with a lysozyme concentration of 21 mg/ml, was made as the temperature was stepped down from 35°C to 25°C to 20°C to 15°C as shown in Fig. 18.

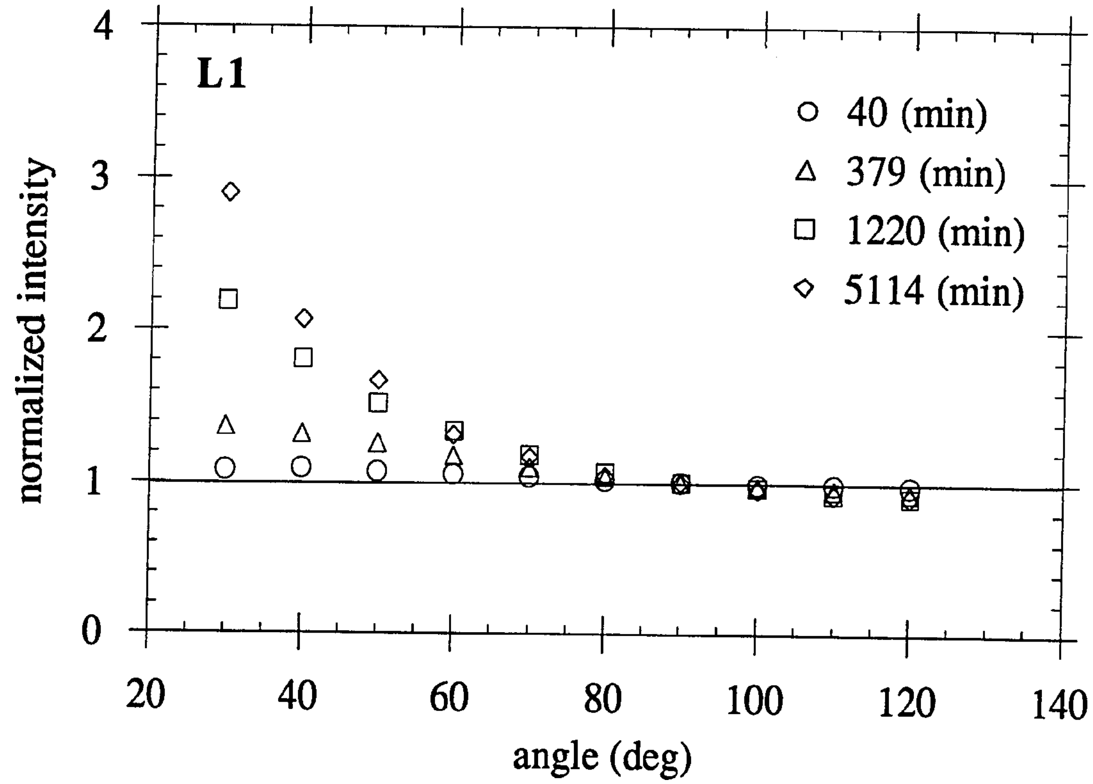

FIG. 14. The appearance and subsequent increase in forward scattering consistent with a polydisperse system of Mie scatterers (λ_0 = 488 nm) is shown. The intensity is normalized to that at 90°. This is sample L1: 6.75 mg/ml lysozyme, pH 4.4, 6.5% NaCl, and T = 30°C. (These data appear in Ref. 11. Reprinted with permission.)

(a)

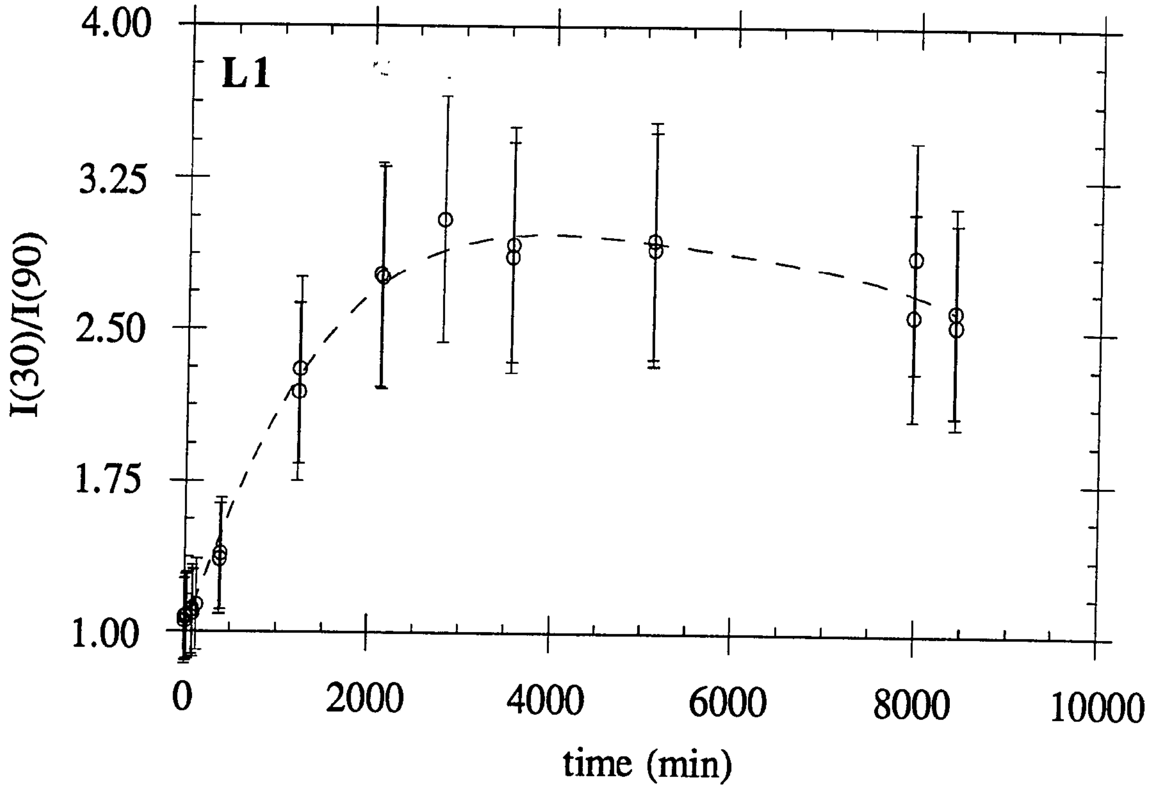

FIG. 15. Displayed in (a) - (c) are the results of Sample L1: 6.75 mg/ml lysozyme, pH 4.4, 6.5% NaCl, T = 30°C, and λ_0 = 488 nm.

(a) The increase in FS over time is shown. Mie particles appear and increase in size and/or number. The curve is a fourth order polynomial.

(b) The single-τ d_{eff} is seen to behave similarly to FS. A fifth order polynomial is fit to d_{eff}.

(c) The behavior of multi-τ d_{eff} is compared to that of single-τ d_{eff}. Both curves are fifth order polynomials. The multi-τ measurement is sensitive to a broader range of fluctuations and therefore, includes the larger sizes of the polydisperse distribution (c.f. Fig. 33).

(b)

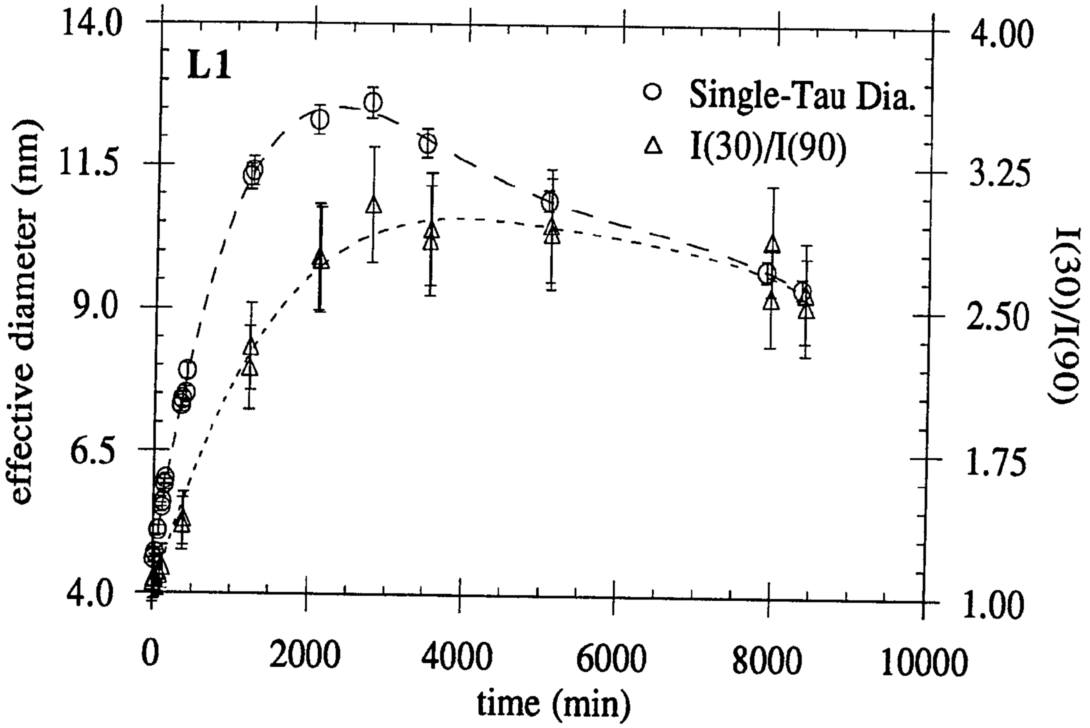
L1
○ Single-Tau Dia.
△ I(30)/I(90)
effective diameter (nm)
14.0
11.5
9.0
6.5
4.0
I(30)/I(90)
4.00
3.25
2.50
1.75
1.00
0
2000
4000
6000
8000
10000
time (min)

(c)

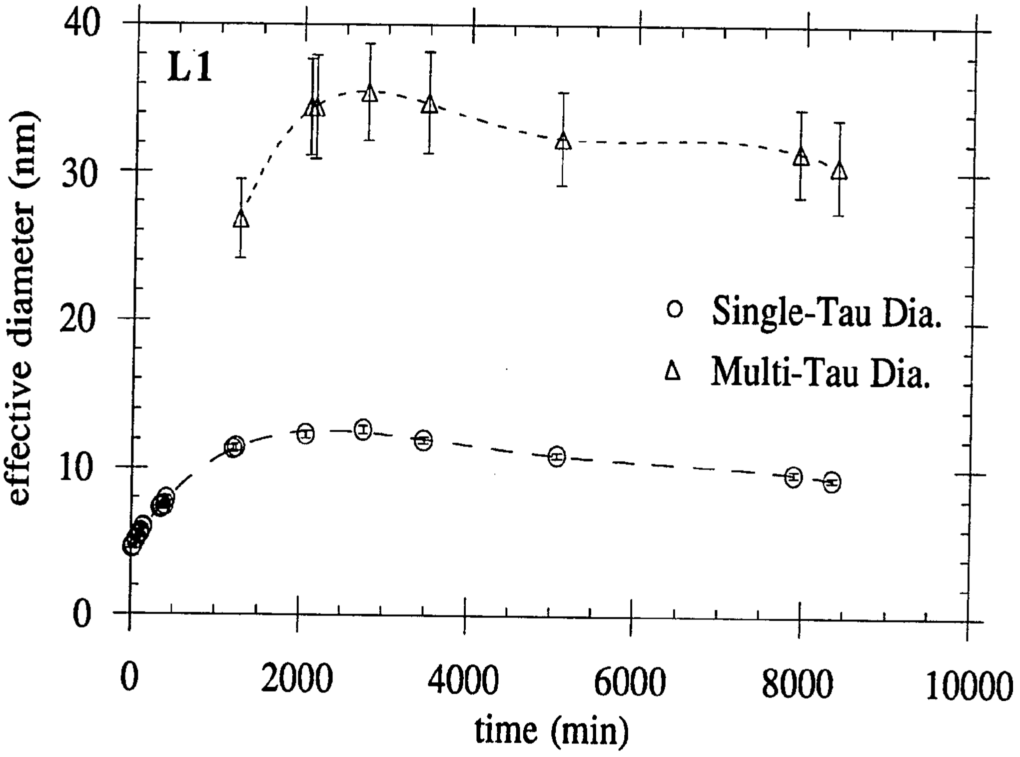
L1
effective diameter (nm)
0
10
20
30
40
0
2000
4000
6000
8000
10000
time (min)
○ Single-Tau Dia.
Δ Multi-Tau Dia.

(a)

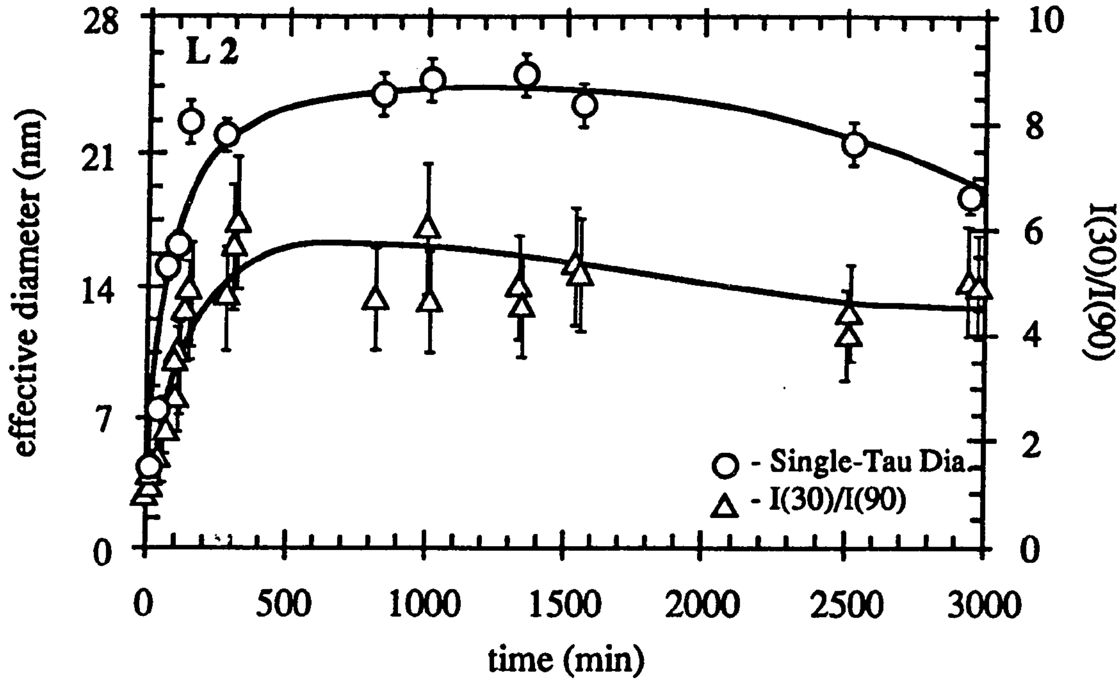

FIG. 16. Displayed in (a) - (d) are the results of Sample L2: 6.75 mg/ml lysozyme, pH 4.4, 6.5% NaCl, T = 30°C, and λ_0 = 488 nm.

(a) The increase in FS and single-τ d_{eff} over time is shown. Again, these two measures behave similarly. Even though conditions were identical to those of L1, the aggregation is more rapid. The curve is hand drawn.

(b) The behavior of multi-τ d_{eff} is compared to that of single-τ d_{eff}. Both curves are hand drawn. Again, the multi-τ measurement is sensitive to a broader range of fluctuations.

(c) The first 300 min of FS and single-τ d_{eff} are shown. The data are shown to fit with a fifth order polynomial over this interval.

(d) The first 300 min of single-τ d_{eff} and multi-τ d_{eff} are shown. The curve is a fifth order polynomial.

(b)

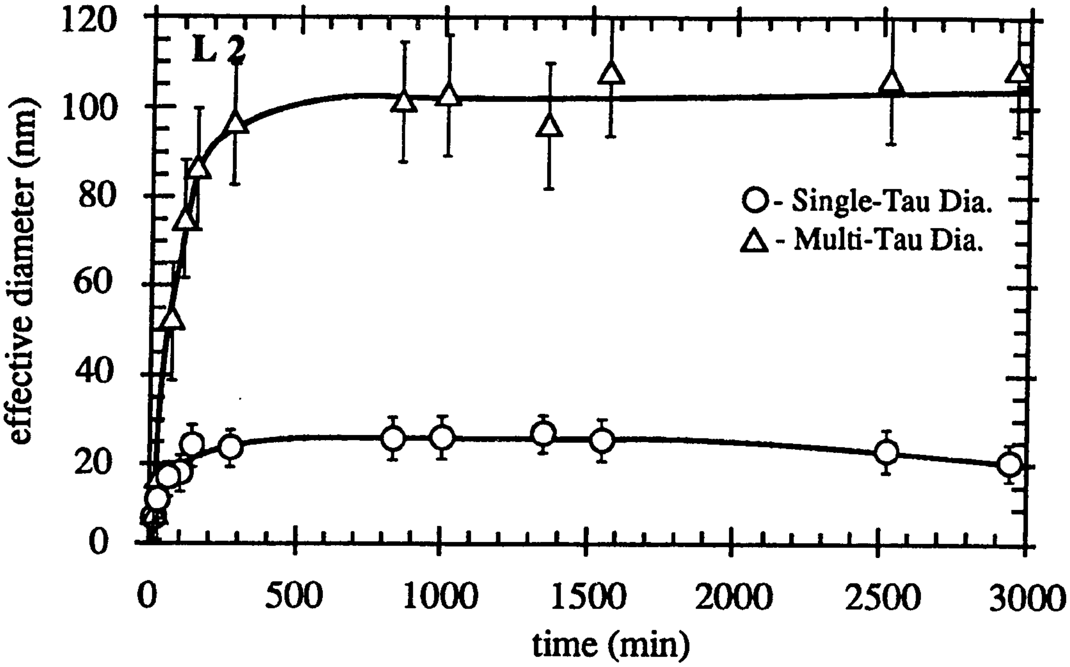
L 2
120
100
80
60
40
20
0
effective diameter (nm)
0
500
1000
1500
2000
2500
3000
time (min)
○- Single-Tau Dia.
△ - Multi-Tau Dia.

(c)

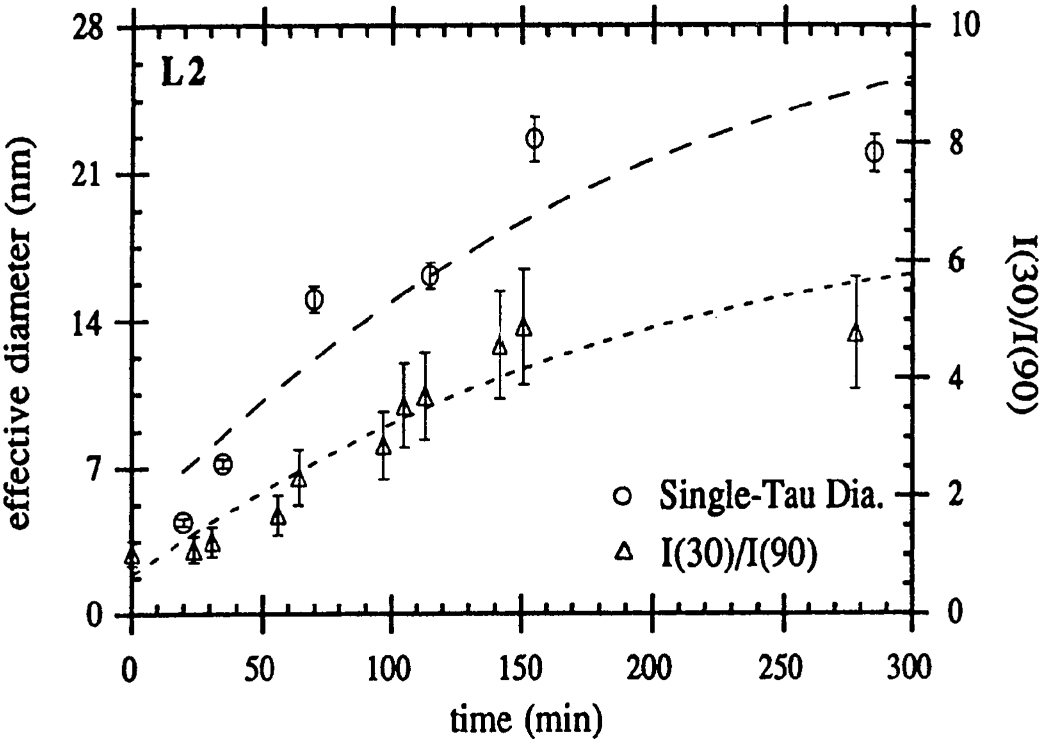
L2
effective diameter (nm)
I(30)/I(90)
time (min)
○ Single-Tau Dia.
△ I(30)/I(90)
0
7
14
21
28
0
2
4
6
8
10
0
50
100
150
200
250
300

(d)

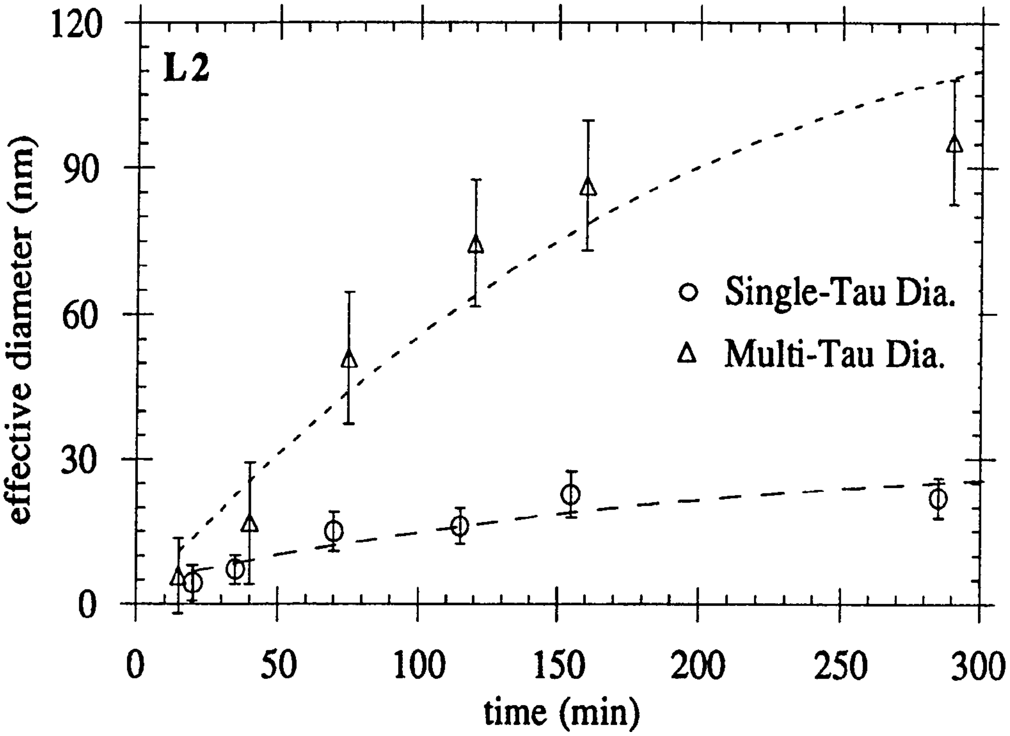
L2
effective diameter (nm)
time (min)
0
30
60
90
120
0
50
100
150
200
250
300
○ Single-Tau Dia.
△ Multi-Tau Dia.

(a)

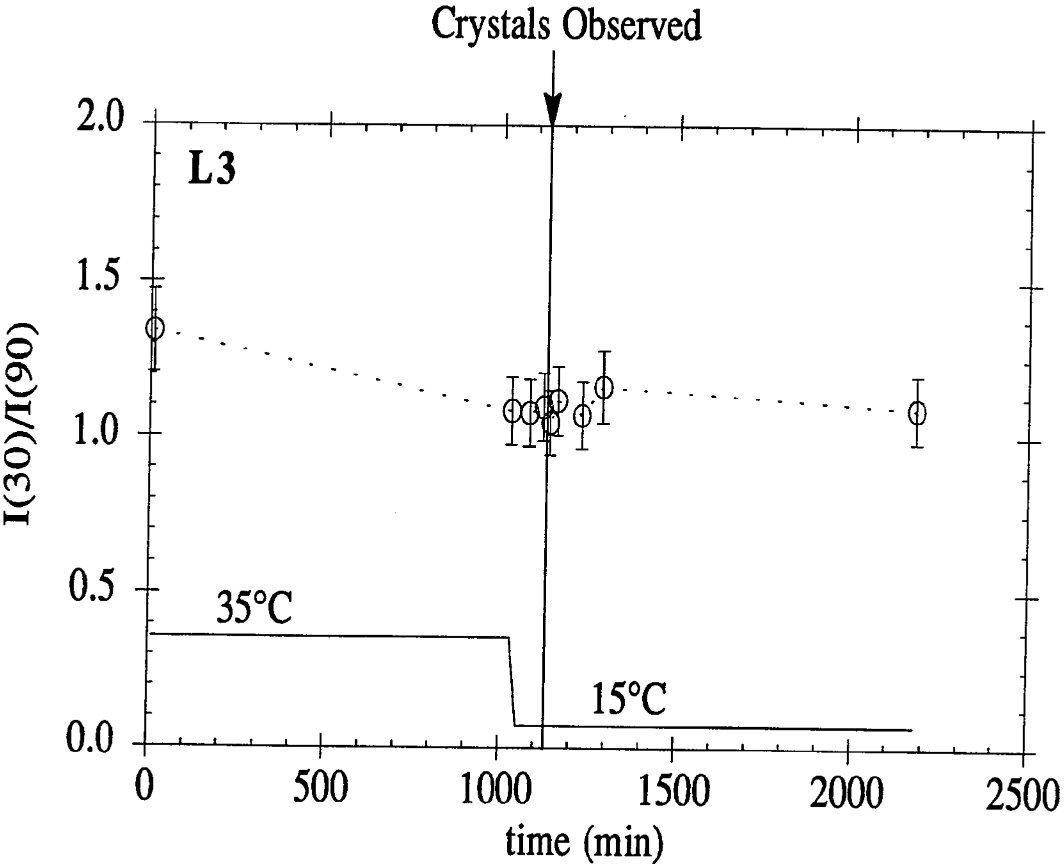

FIG. 17. Crystals appeared in this sample, L3: 16 mg/ml lysozyme, pH 4.4, 3.0% NaCl, and λ_0 = 488 nm. The temperature was reduced from 35°C to 15°C in one step as shown by the solid line in (a) - (c). The time at which crystals were observed as scintillations from the cuvette walls is noted by the vertical line.

(a) FS vs time is shown. The first point may be high due to microbubbles in the sample from filtering. During crystallization, no significant deviation from one is seen. The dotted lines connect the data points.

(b) Single-τ d_{eff} vs time is shown. The CRAGG profile begins to emerge from the data of L3. The hand drawn curve superimposes the profile as it later evolved.

(c) Multi-τ d_{eff} is seen to compare favorably to single-τ d_{eff}.

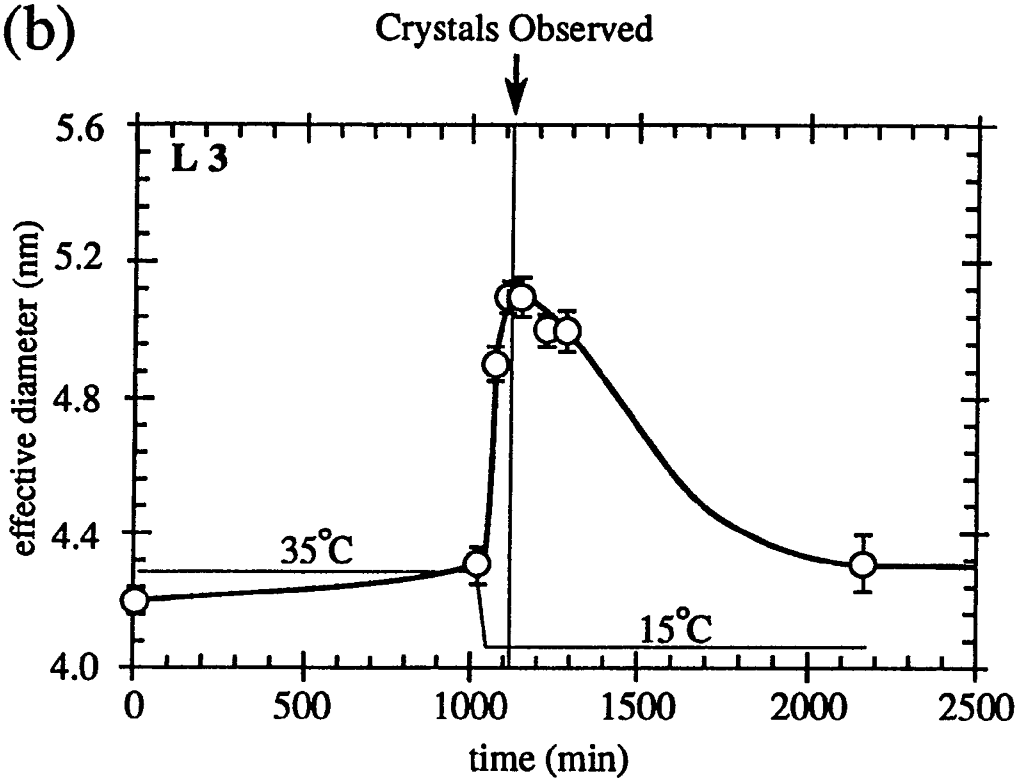
(b)
Crystals Observed
L 3
35°C
15°C
5.6
5.2
4.8
4.4
4.0
effective diameter (nm)
0
500
1000
1500
2000
2500
time (min)

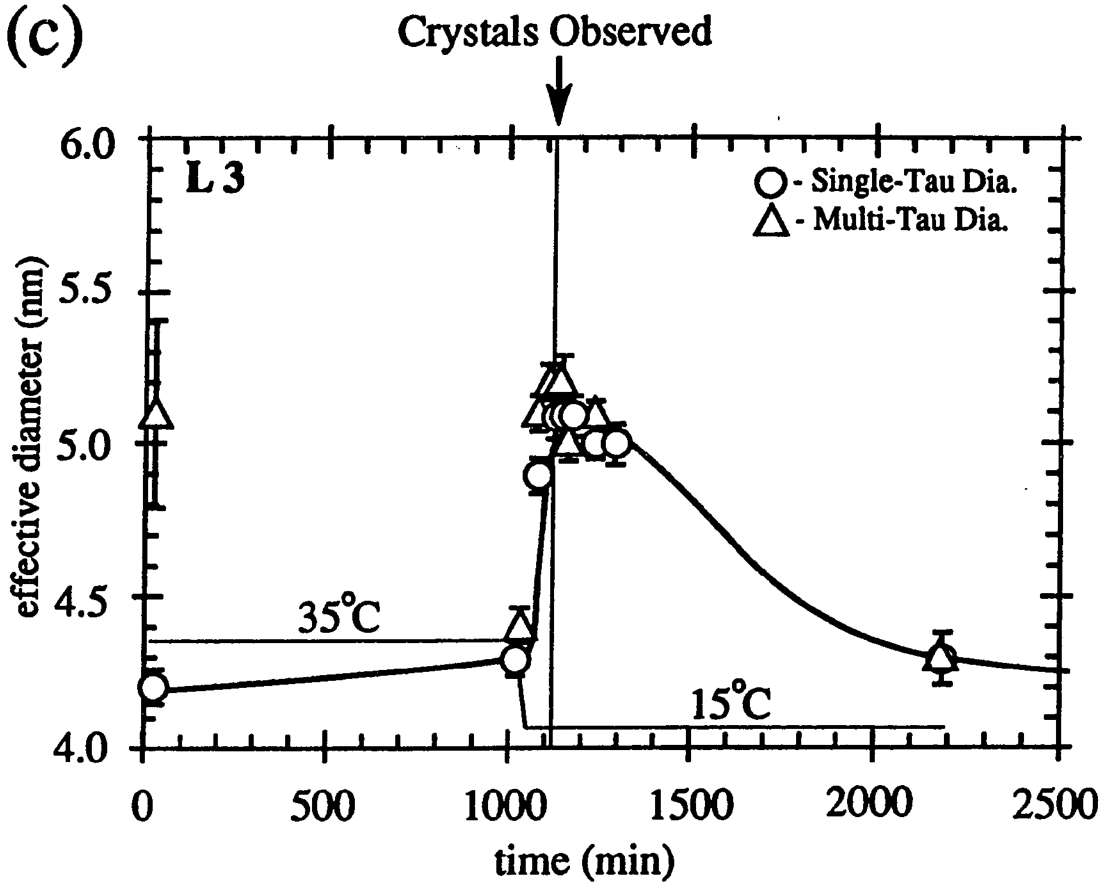
(c)
Crystals Observed
L 3
○ - Single-Tau Dia.
△ - Multi-Tau Dia.
effective diameter (nm)
6.0
5.5
5.0
4.5
4.0
35°C
15°C
0
500
1000
1500
2000
2500
time (min)

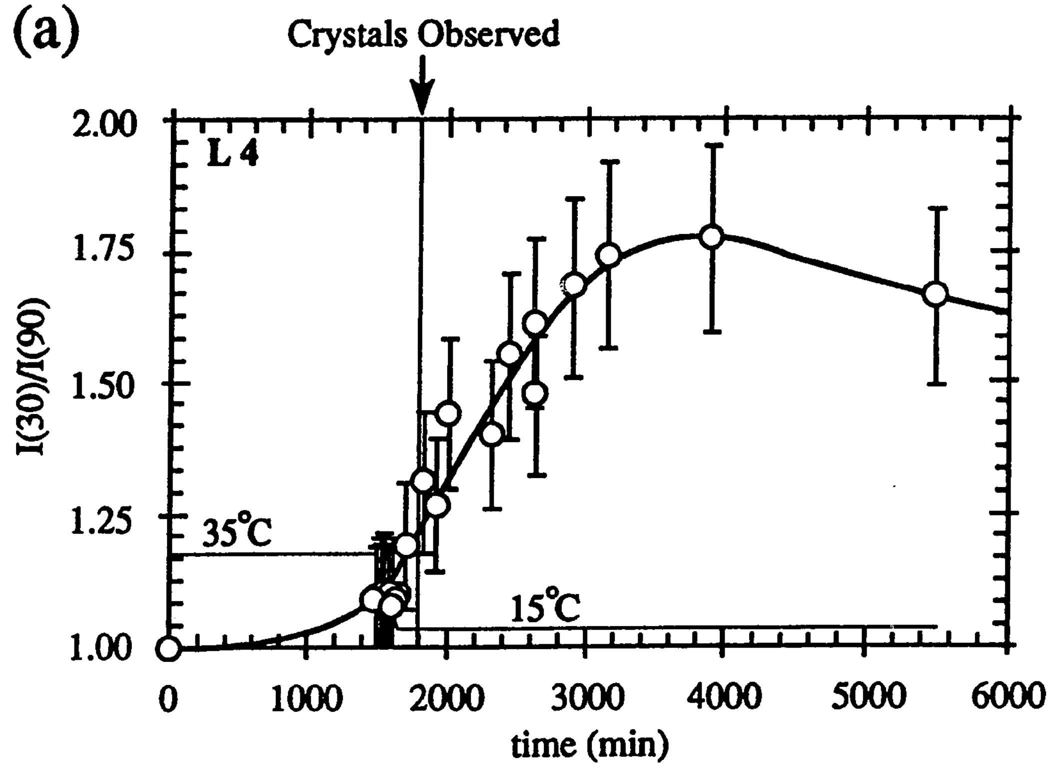

FIG. 18. Crystals appeared in sample L4: 21 mg/ml lysozyme, pH 4.4, 3.0% NaCl, and λ_0 = 488 nm. The temperature was reduced in steps (35°C to 25°C to 20°C to 15°C noted by the solid line). The time at which crystals were observed is noted. The smooth curves are hand drawn in (a) - (d).

(a) FS vs time is shown. An increase in FS is obvious after crystals appear. Note that the increase is not as large as that of L1 and L2.

(b) Single-τ d_{eff} vs time is shown. The CRAGG profile becomes more obvious.

(c) Multi-τ d_{eff} is seen to deviate from single-τ d_{eff}.

(d) A portion (1000 min $\leq t \leq$ 3000 min) of (b) is shown. Single-τ d_{eff} is sensitive to the PreCRAGG distribution and remains unaffected by the Mie scatterers.

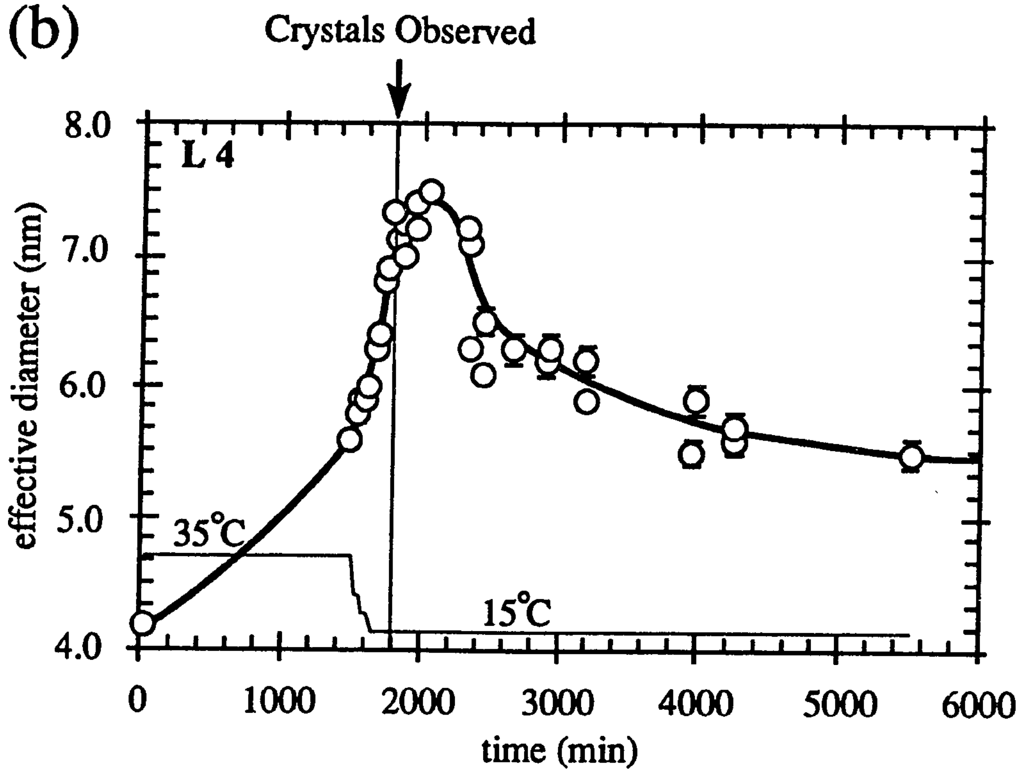
(b)
Crystals Observed
L 4
8.0
7.0
6.0
5.0
4.0
effective diameter (nm)
35°C
15°C
0
1000
2000
3000
4000
5000
6000
time (min)

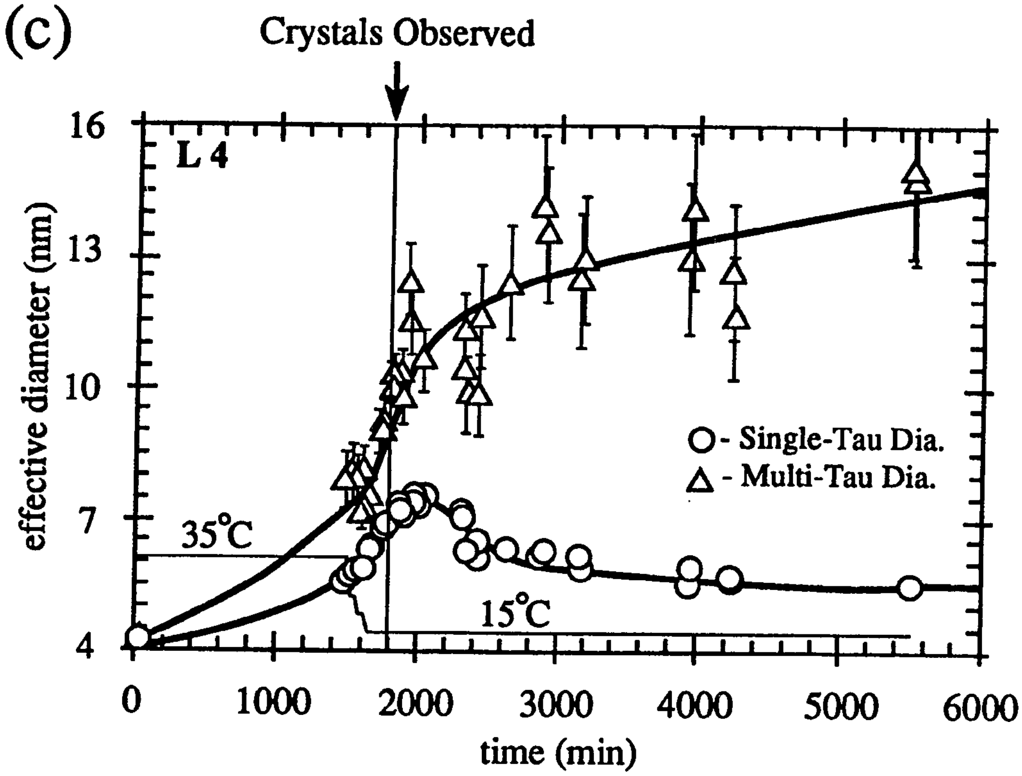
(c)
Crystals Observed
L 4
effective diameter (nm)
16
13
10
7
4
35°C
15°C
O - Single-Tau Dia.
Δ - Multi-Tau Dia.
0
1000
2000
3000
4000
5000
6000
time (min)

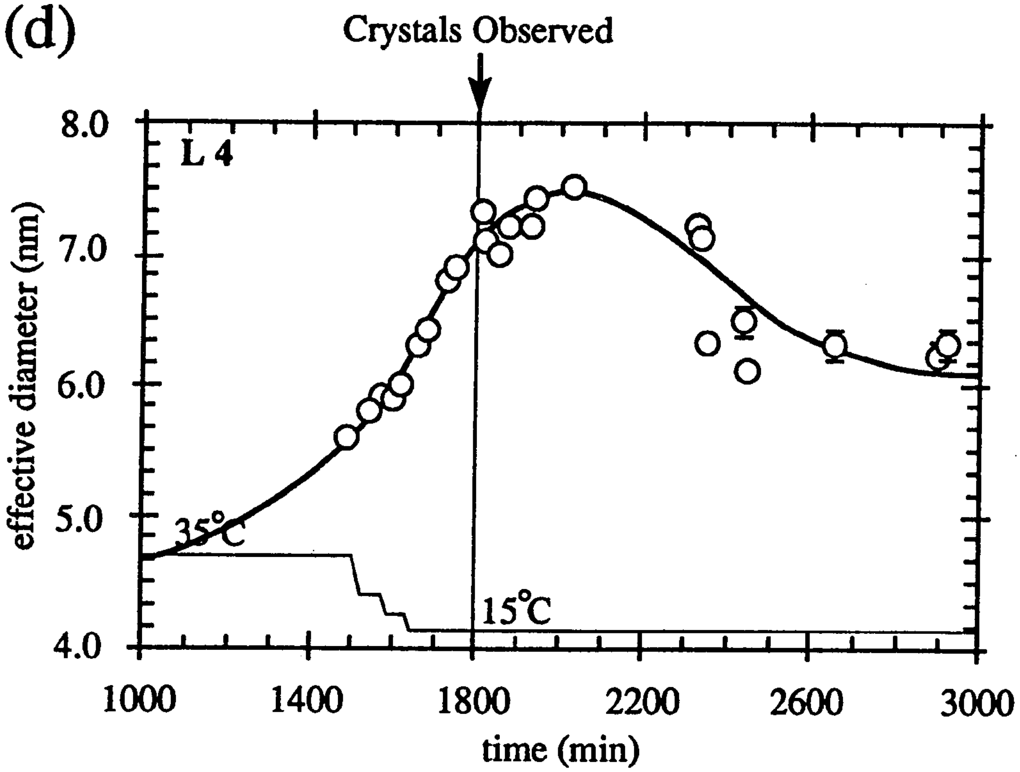
(d)
Crystals Observed
L 4
35°C
15°C
effective diameter (nm)
8.0
7.0
6.0
5.0
4.0
1000
1400
1800
2200
2600
3000
time (min)

At each step the sample equilibrated to the new temperature within 10 minutes. Classical measurements [see Fig. 18(a)] show an increase in forward scattering which is of lesser magnitude than was observed in L1 and L2.

In summary, the low protein, high ionic strength solutions had shown a large increase in d_{eff} and in FS. Any resulting precipitate was amorphous or amorphous with orthorhombic crystals. The higher protein, lower ionic strength solutions yielded tetragonal crystals. These solutions showed a rather slight increase in d_{eff}, and sometimes in FS, during nucleation. After crystals were visible, d_{eff} reached a maximum, and finally decreased to near the initial value. (Note: d_{eff} is calculated to eliminate the known effects of temperature on diffusion as given by the Stokes-Einstein relation. Changes in d_{eff} reflect changes in the friction encountered by the particles, which in interacting systems is only partly dependent on particle size. For L1 and L2, the viscosity of 5% NaCl was used, and for L3 through L6 that of 3% NaCl was used.)

2. Insulin

Upon achieving tetragonal lysozyme crystals the research focus shifted to insulin, the protein which had been chosen to demonstrate temperature induced crystallization in the Protein Crystallization Facility[60] on board the space shuttle (STS 37 and STS 42). Although the solubility of insulin was not available, solution parameters were chosen according to Krayenbuhl and Rosenberg[56] in an attempt to achieve crystallization as the temperature was lowered from 40°C to room temperature.

These insulin samples were not well suited for study by light scattering. At 40°C the samples began as good, clean light scattering specimens. However, at the onset of crystallization, which proved unpredictable due to the preparation protocol, it became difficult or impossible to make light scattering measurements because of an "active period." The active period was a period of time during which bright scintillations from the scattering volume thwarted efforts to measure a baseline for PCS calculations and made classical measurements erratic. After crystals were visible on the cuvette sides, the active period would subside, and measurements were again possible. PCS data were collected during the active period, and if a baseline could be used, the measurement was reported although this was rarely the case.

Even though every sample was prepared with identical protocol, the onset, severity, and duration of the active period varied from sample to sample. This is demonstrated by the following three samples:

1) The sample I1 of Fig. 19 had a severe sustained active period beginning at 30°C. Crystals did not become visible until room temperature was reached.

2) The sample I2 of Fig. 20, which had more refined temperature steps, showed a mild active period. It began as the temperature was brought to 26°C. PCS was impossible during this time, but classical measurements were not strongly affected.

3) Some samples became active at 40°C as demonstrated by sample I3 in Fig. 21. Crystals also appeared at this temperature.

These inconsistencies, typical of the insulin, were a source of much frustration and are attributed to the preparation protocol. The concentration was never actually known. Nevertheless, light scattering proved an adequate detector of the onset of the active period, which in these studies always preceded the appearance of crystals. PCS was rarely

(a)

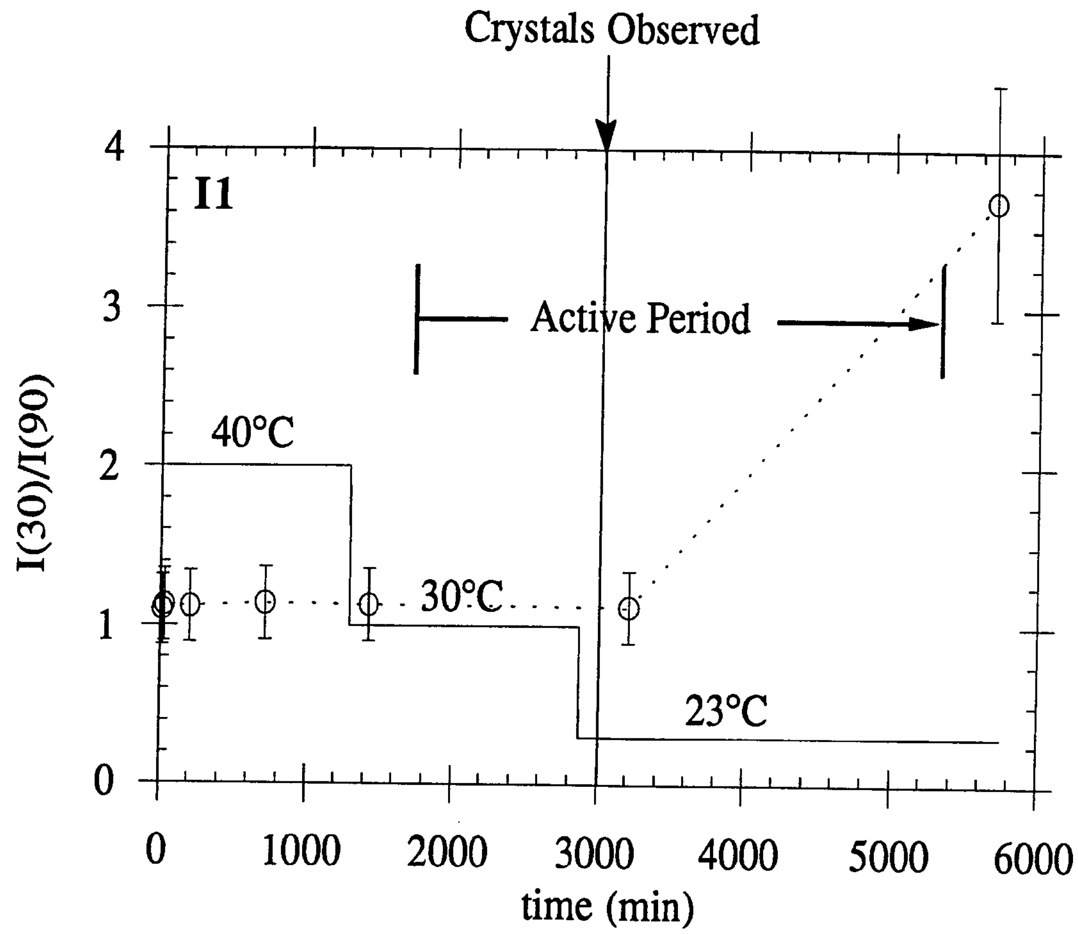

FIG. 19. The results of insulin sample I1 are displayed. All insulin samples were prepared identically as described in the text. The temperature of I1 was reduced in three steps as noted by the solid line. The vertical line denotes the time at which the cuvette walls began to cloud slightly. At nucleation all samples underwent an active period, which is noted in (a) - (c). The dotted lines connect the data points.

(a) FS vs time is shown.

(b) Single-τ d_{eff} vs time is shown.

(c) Single-τ d_{eff} is compared to multi-τ d_{eff}.

(b)

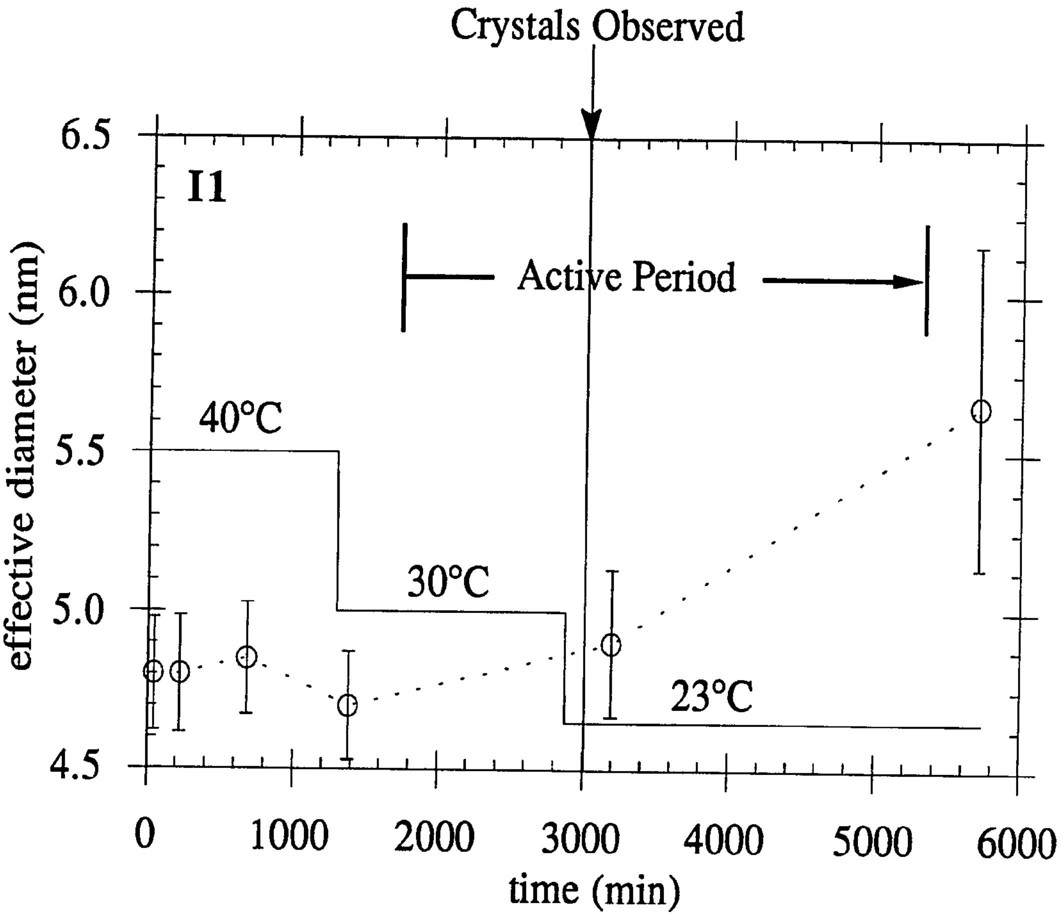
Crystals Observed
I1
Active Period
40°C
30°C
23°C
6.5
6.0
5.5
5.0
4.5
effective diameter (nm)
0
1000
2000
3000
4000
5000
6000
time (min)

(c)

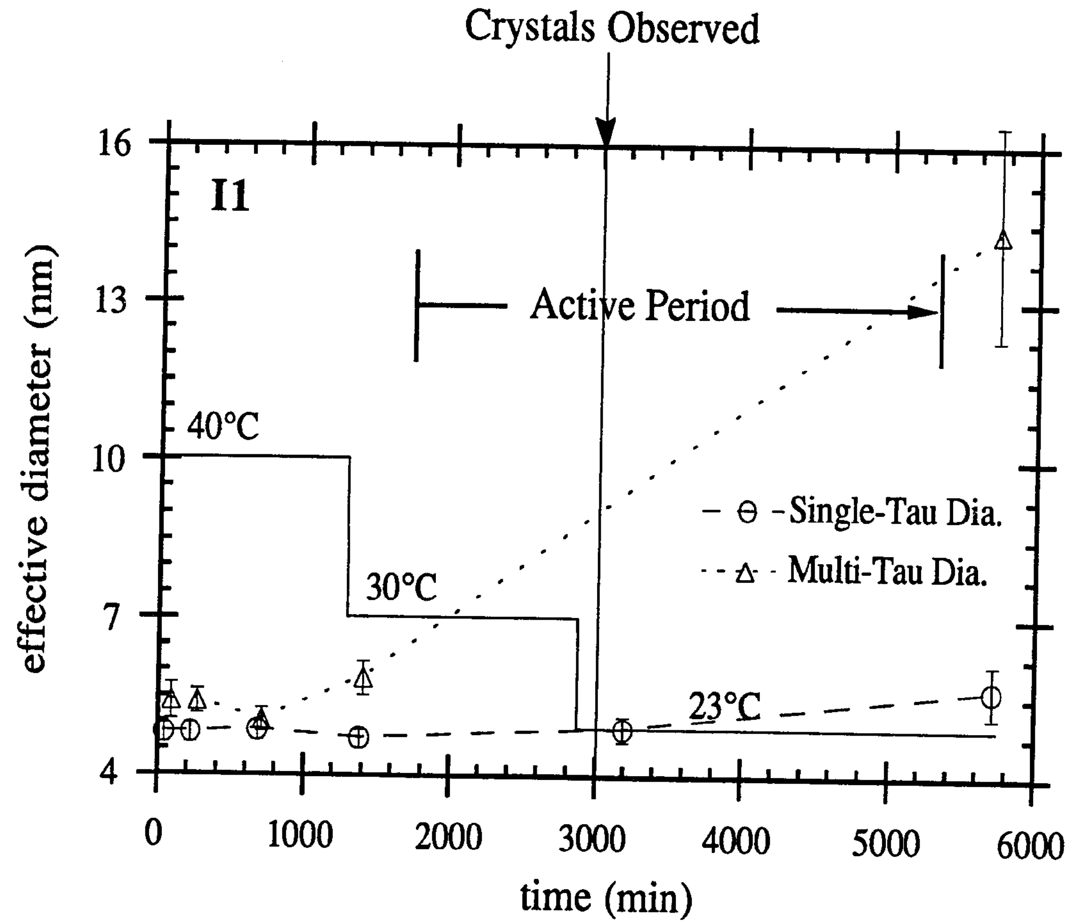
Crystals Observed
I1
Active Period
40°C
30°C
23°C
Single-Tau Dia.
Multi-Tau Dia.
effective diameter (nm)
4
7
10
13
16
time (min)
0
1000
2000
3000
4000
5000
6000

(a)

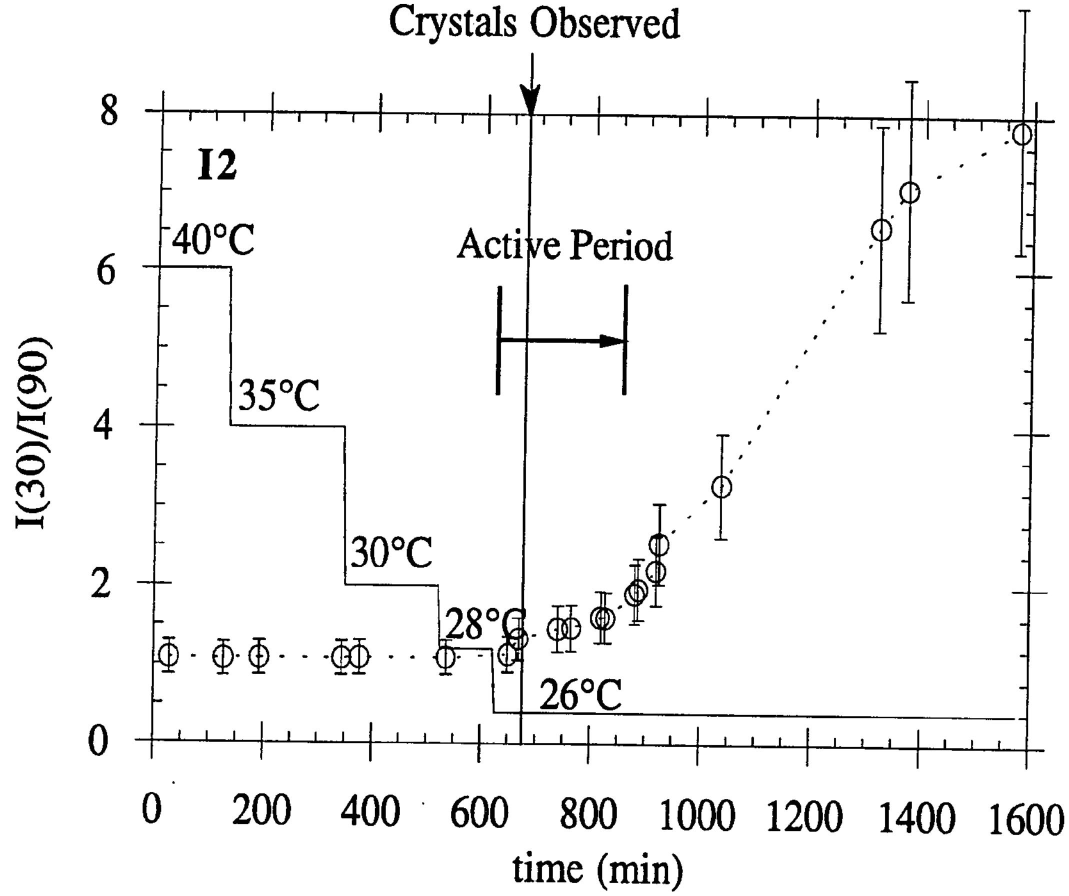

FIG. 20. The results of insulin sample I2 are displayed. The temperature of I2 was reduced in five steps as noted by the solid line. The vertical line denotes the time at which the cuvette walls began to cloud slightly. At nucleation all samples underwent an active period, which is noted in (a) - (c). The dotted lines connect the data points.

(a) FS vs time is shown.

(b) Single-τ d_{eff} vs time is shown.

(c) Single-τ d_{eff} is compared to multi-τ d_{eff}.

(b)

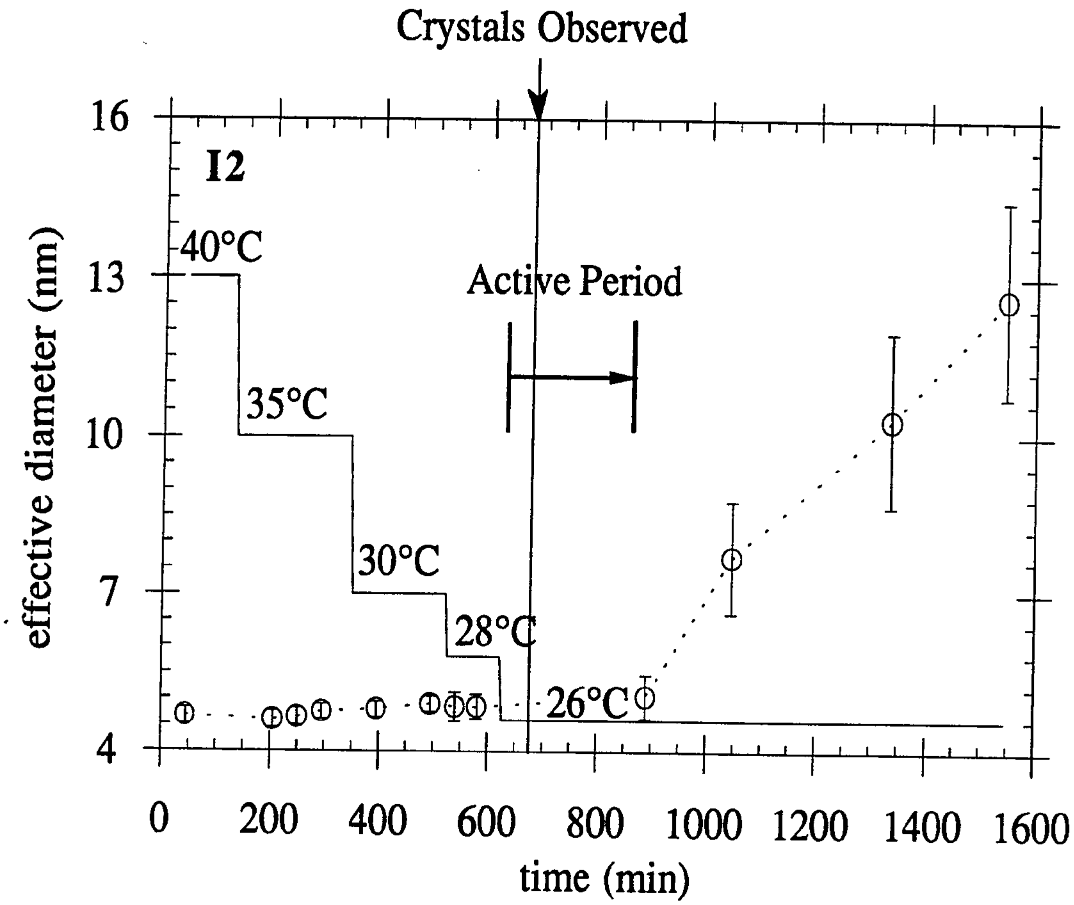
Crystals Observed
I2
40°C
35°C
30°C
28°C
26°C
Active Period
effective diameter (nm)
16
13
10
7
4
0
200
400
600
800
1000
1200
1400
1600
time (min)

(c)

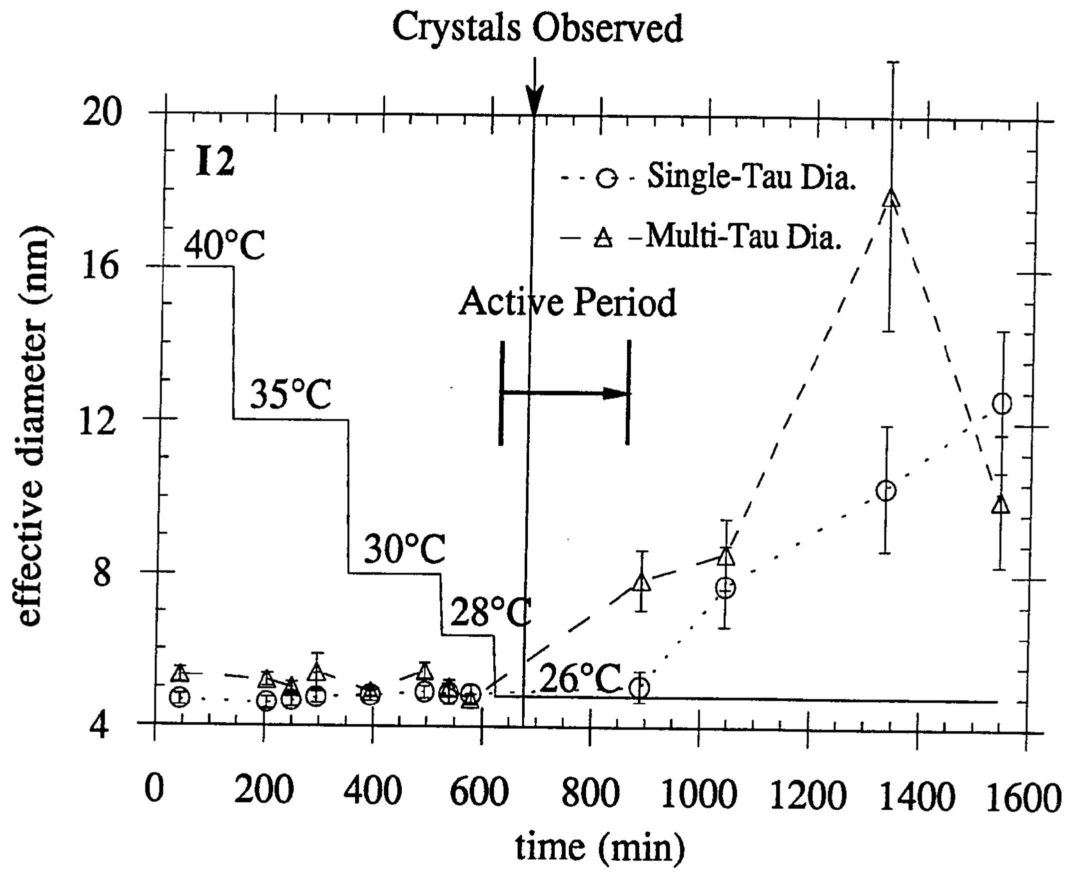
Crystals Observed
I2
- - ○ - Single-Tau Dia.
— △ –Multi-Tau Dia.
40°C
35°C
30°C
28°C
26°C
Active Period
effective diameter (nm)
time (min)
20
16
12
8
4
0
200
400
600
800
1000
1200
1400
1600

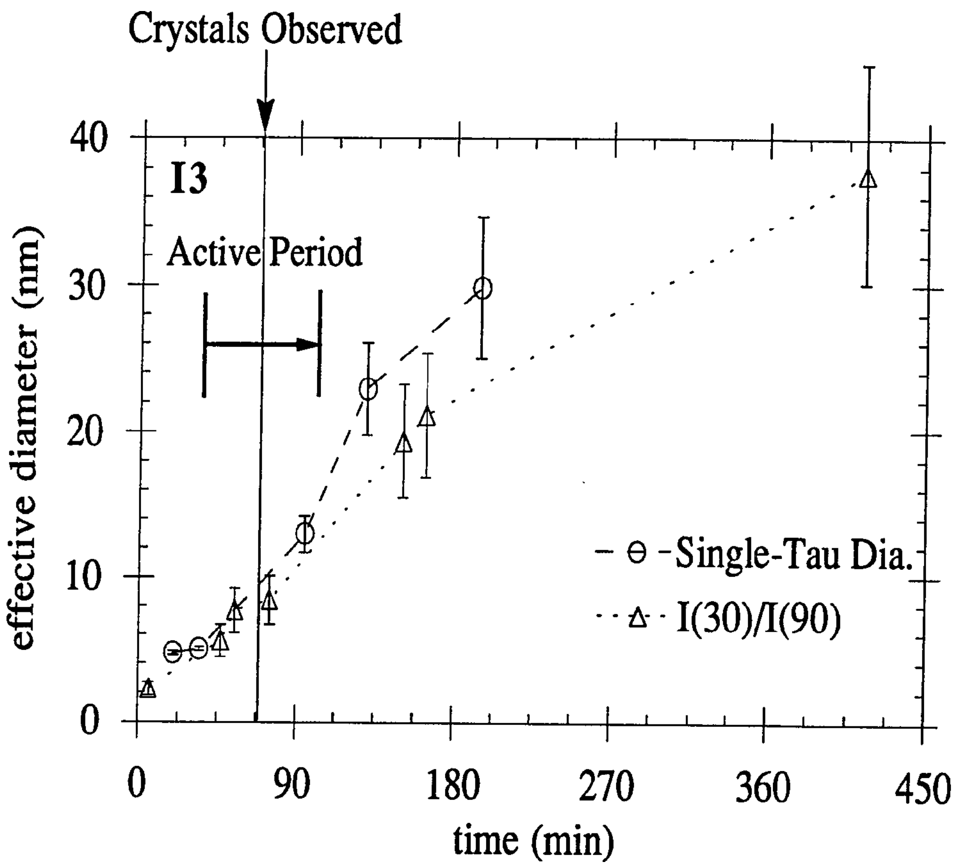

FIG. 21. The results of insulin sample I3 are displayed. I3 became active while being held at 40°C. The vertical line denotes the time at which the cuvette walls began to cloud slightly. The dotted lines connect the data points.

possible during the active period, but in some instances, measurement of FS was possible.

With lysozyme and insulin, light scattering had proven itself as a detector of nucleation, but analysis of the phenomena occurring during nucleation remained elusive. Such an analysis of insulin was not possible without a long term investigation of crystallization conditions, so the research focus returned to the reasonably well behaved lysozyme solutions. The Brookhaven at UAH was equipped with the BI control program, an automated data collection program that makes multi-q measurements feasible. Also, microscopy studies on lysozyme at UAH allowed access to ultrapure samples, so the next data were collected there.

B. UAH results

The first endeavor at UAH was to observe tetragonal crystallization isothermally. The samples were prepared at room temperature with conditions such that crystallization would not occur at room temperature but would occur at 11°C. They were then placed directly into the scattering chamber, which was held at 11°C. Equilibration to 11°C occurred within four minutes. At this temperature crystallization proceeded.

Figure 22 demonstrates the behavior of D_{lin}, D_{2nd}, and I for sample L5 at 46.9 mg/ml lysozyme, 2.5% NaCl, and pH 4.5. The behavior of FS for this sample is shown as Fig. 23. Sample L6, at greater ionic strength and greater lysozyme concentration (55.0 mg/ml lysozyme, 3.0% NaCl), is shown as Figs. 24 and 25. These results were similar to those obtained at UAB, and one can clearly see the benefit of the control program.

After convincingly reproducing the isothermal behavior, a fundamental investigation of lysozyme solutions was begun in order to help

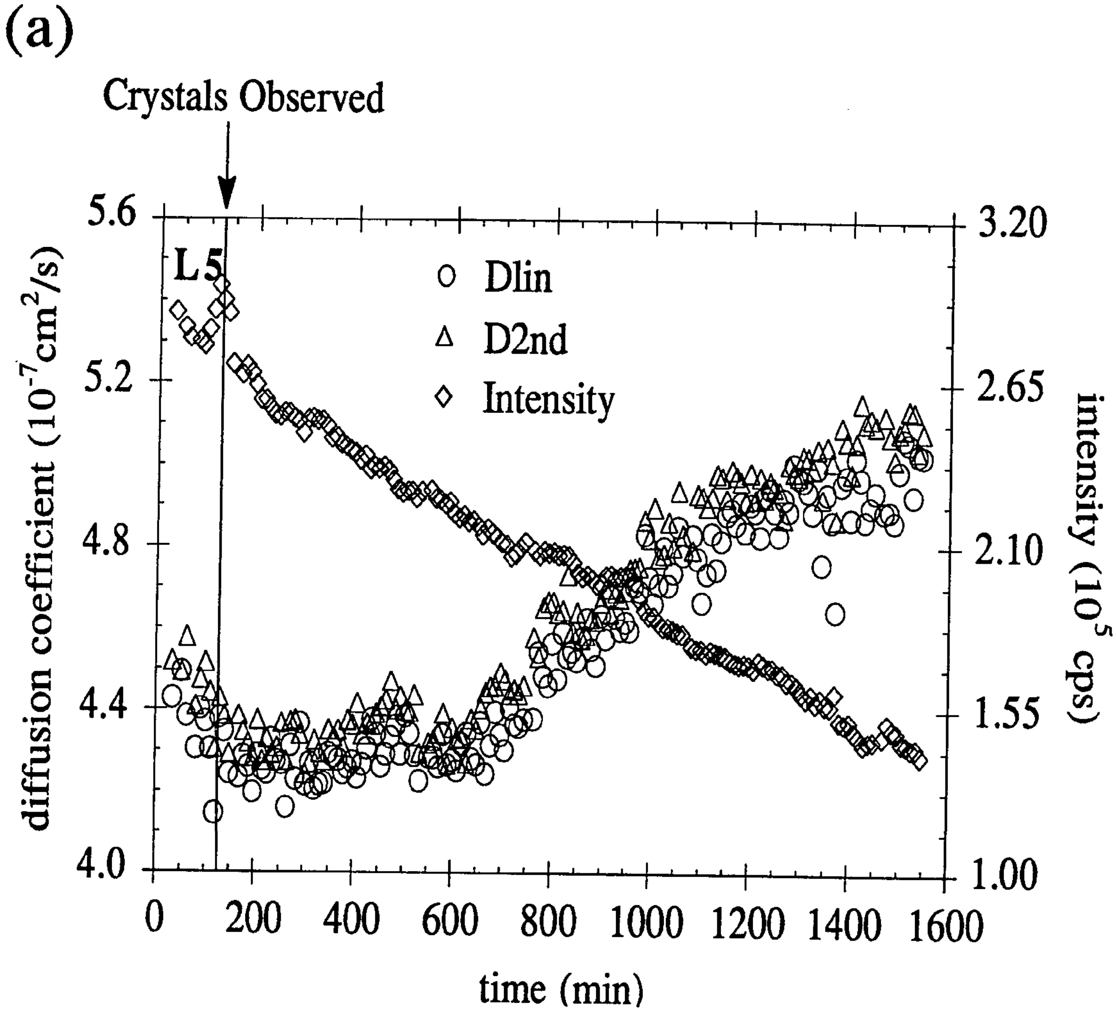

FIG. 22. Shown in (a) - (c) are the D_{lin}, D_{2nd}, and I results at three angles for the UAH lysozyme sample L5: 47.0 mg/ml lysozyme, pH 4.5, 2.5% NaCl, T = 11°C, and λ_0 = 647.1 nm. The solution was prepared undersaturated at room temperature and was placed directly into the scattering chamber, which was held at 11°C. The sample reached 11°C within four minutes. The vertical line denotes the time at which crystals were observed on the cuvette walls. RMS counting errors (for D_{lin} most are less than 1%, for D_{2nd} most are less than 3%) are available for these data but are omitted for easier viewing due to the number of data points.

(a) $\theta = 24°$.

(b) $\theta = 45°$.

(c) $\theta = 90°$.

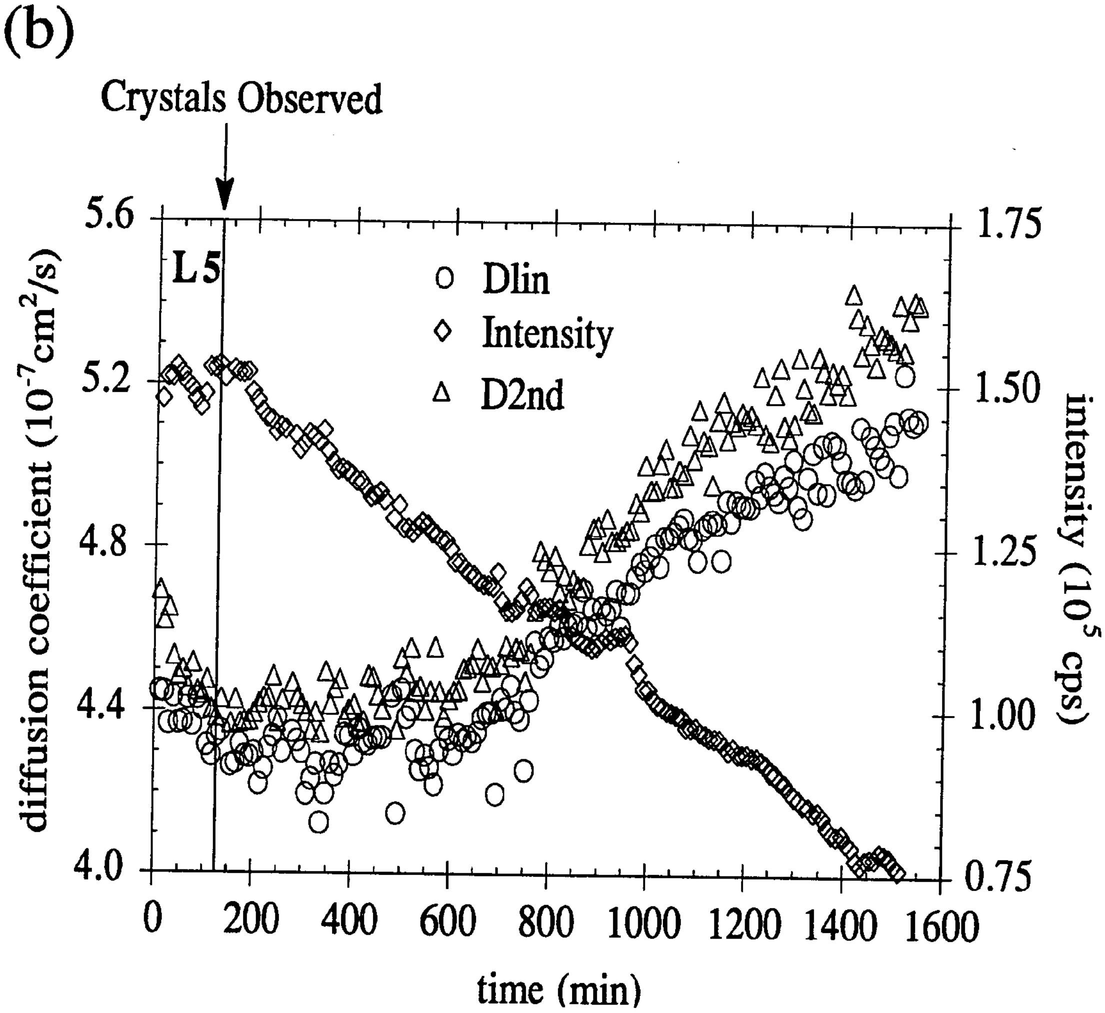
(b)
Crystals Observed
L5
○ Dlin
◇ Intensity
△ D2nd
diffusion coefficient ($10^{-7}cm^2/s$)
5.6
5.2
4.8
4.4
4.0
intensity (10^5 cps)
1.75
1.50
1.25
1.00
0.75
0
200
400
600
800
1000
1200
1400
1600
time (min)

(c)

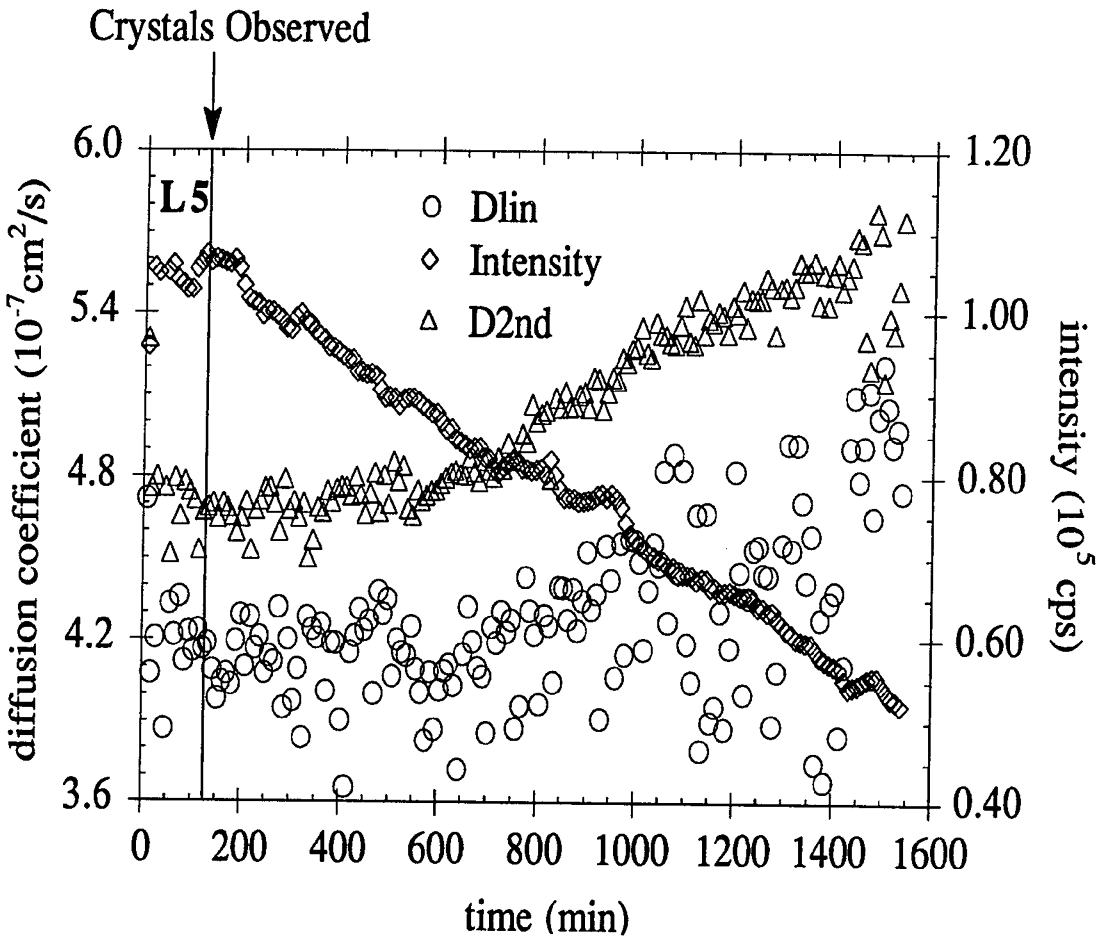
Crystals Observed
L5
○ Dlin
◇ Intensity
△ D2nd
diffusion coefficient ($10^{-7}cm^2/s$)
6.0
5.4
4.8
4.2
3.6
intensity (10^5 cps)
1.20
1.00
0.80
0.60
0.40
0
200
400
600
800
1000
1200
1400
1600
time (min)

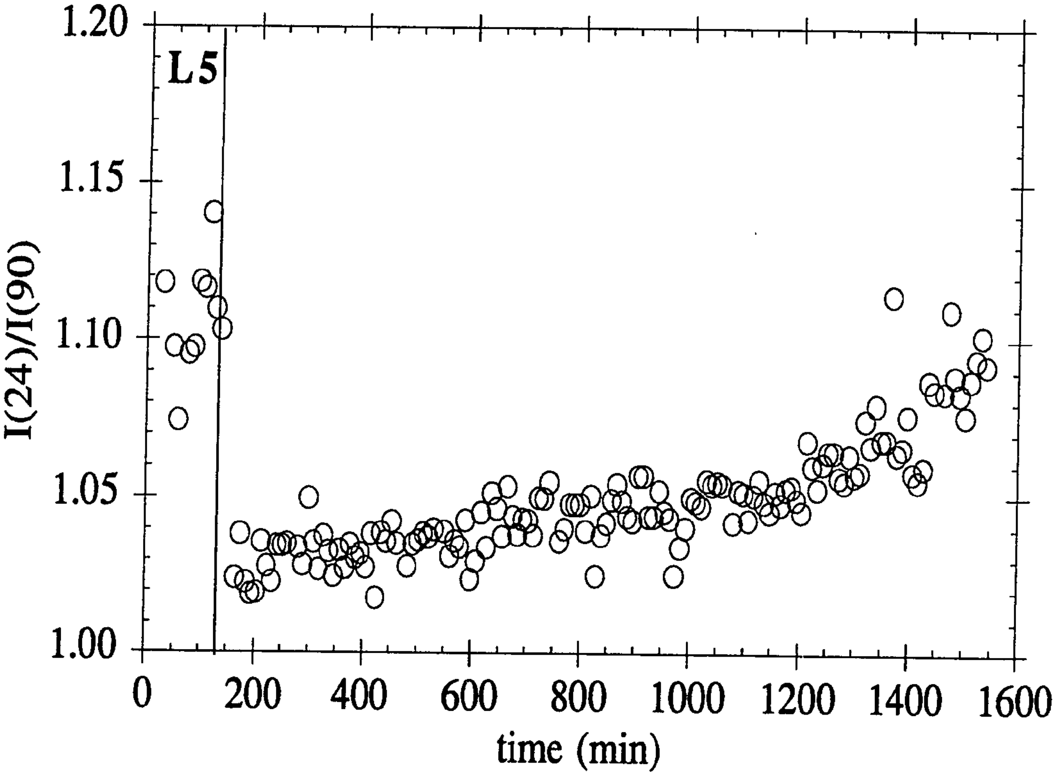

FIG. 23. I(24)/I(90) vs time is shown for L5. The discontinuity when crystals formed is likely due to an occlusion on the cuvette wall. Note the y axis scale; FS does not deviate significantly from one.

(a)

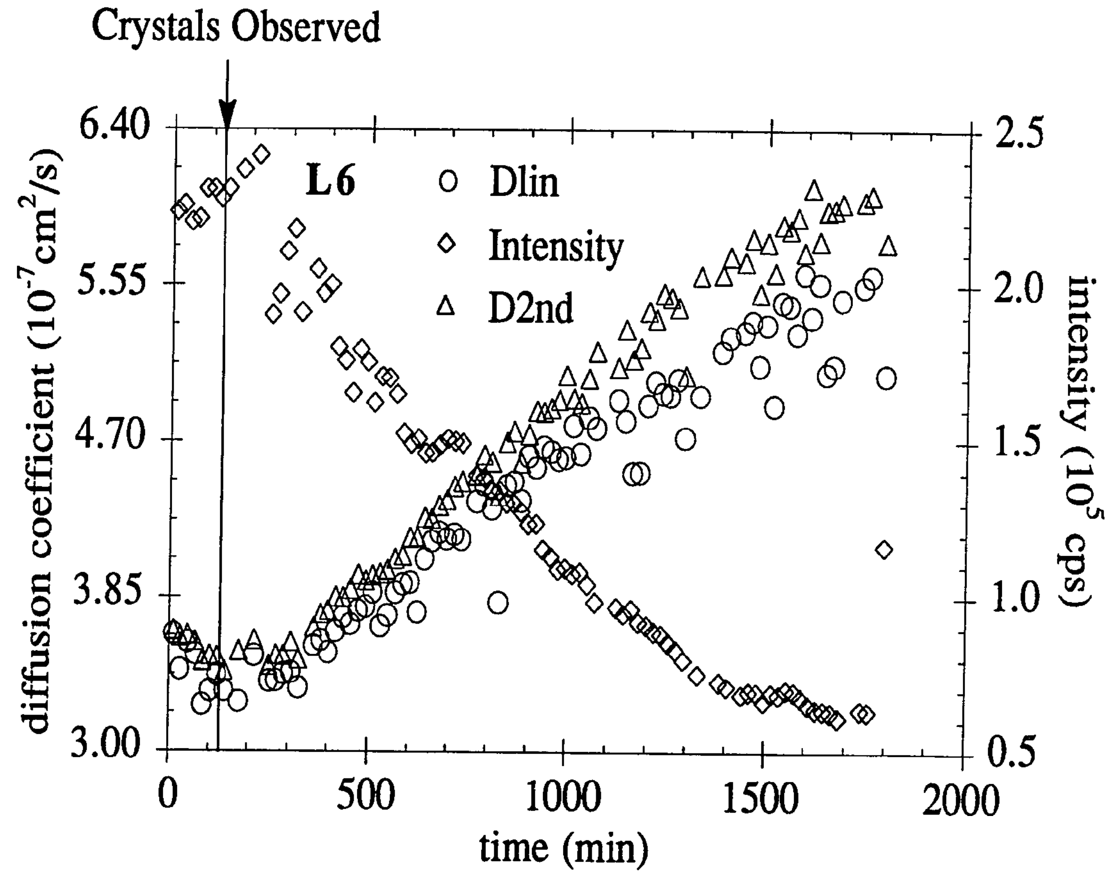

FIG. 24. Shown in (a) - (c) are the D_{lin}, D_{2nd}, and I results at three angles for the UAH lysozyme sample L6: 55.7 mg/ml lysozyme, pH 4.5, 3.0% NaCl, T = 11°C, and λ_0 = 647.1 nm. The solution was prepared undersaturated at room temperature and was placed directly into the scattering chamber, which was held at 11°C. The sample reached 11°C within four minutes. The vertical line denotes the time at which crystals were observed on the cuvette walls. RMS counting errors (for D_{lin} most are less than 1%, for D_{2nd} most are less than 3%) are available for these data but are omitted for easier viewing due to the number of data points. The discontinuity in intensity at all angles after crystals formed is likely due to a slight occlusion of the incident beam.

(a) $\theta = 30°$.

(b) $\theta = 60°$.

(c) $\theta = 90°$.

(b)

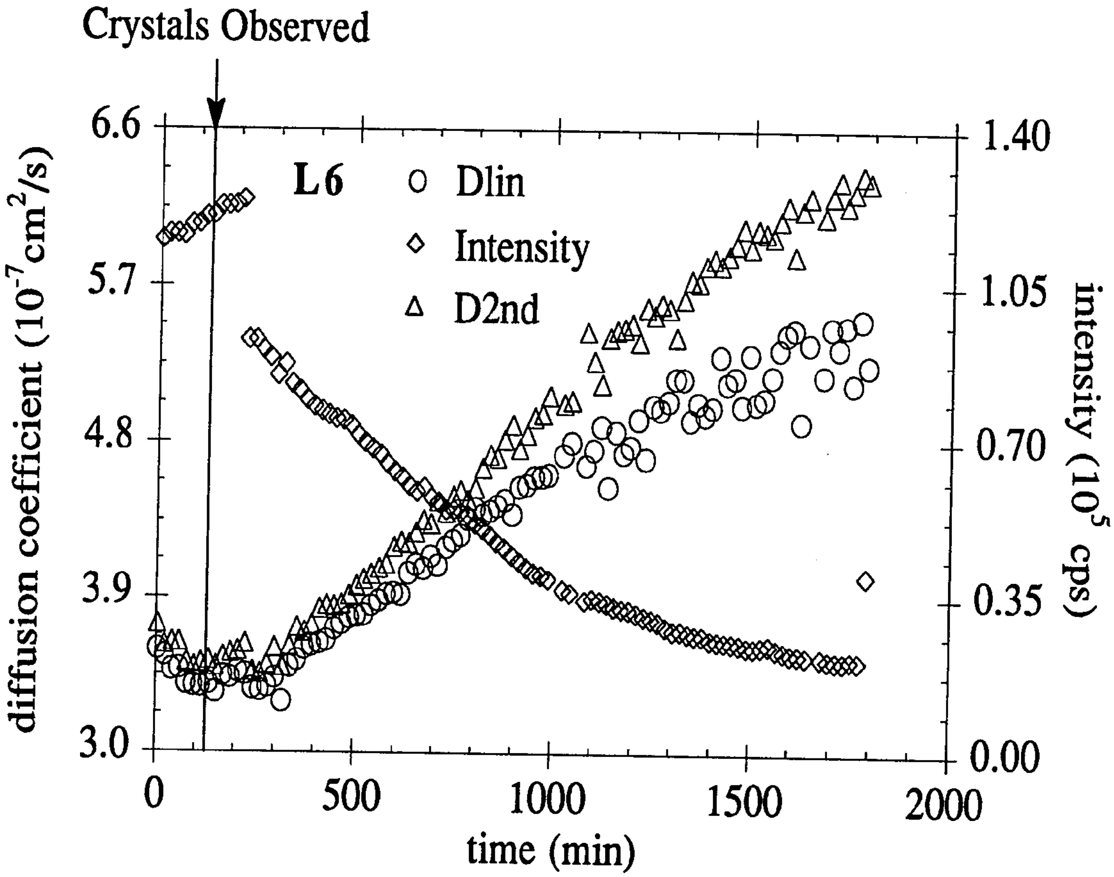
Crystals Observed
L6
Dlin
Intensity
D2nd
diffusion coefficient (10^{-7}cm^2/s)
6.6
5.7
4.8
3.9
3.0
intensity (10^5 cps)
1.40
1.05
0.70
0.35
0.00
0
500
1000
1500
2000
time (min)

(c)

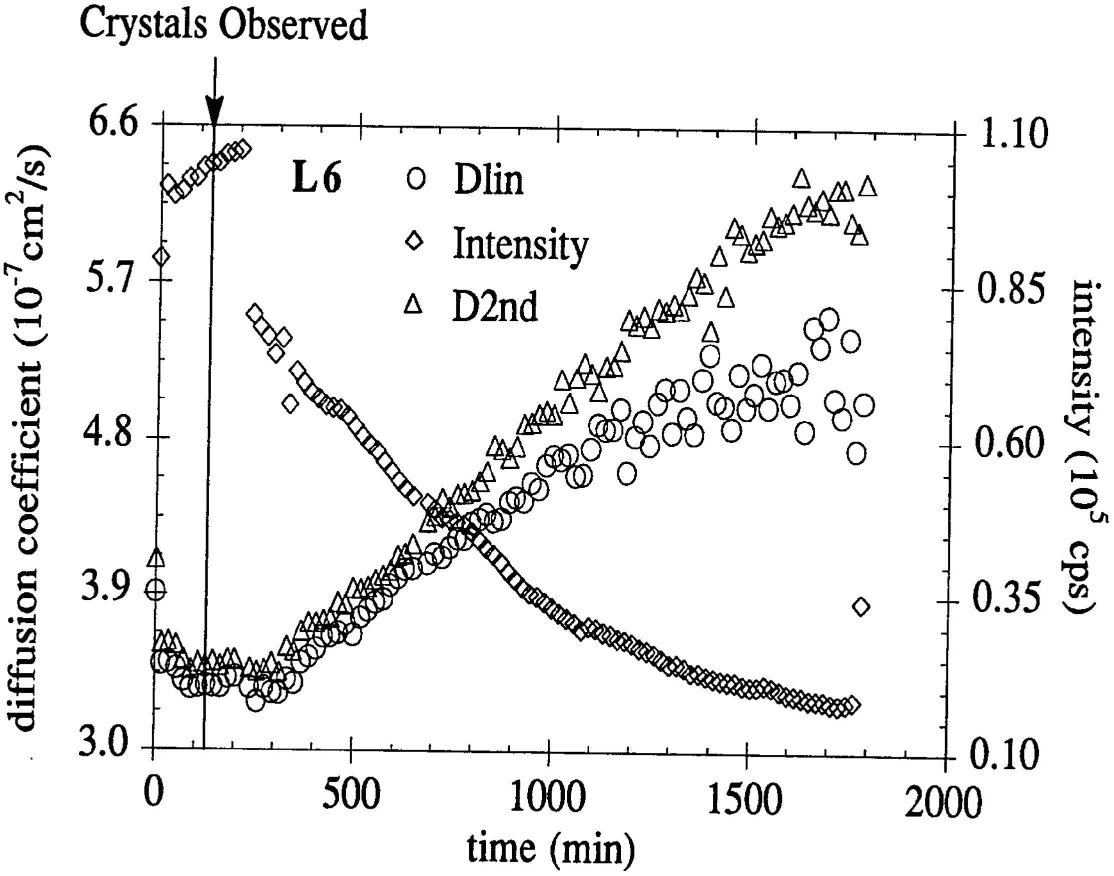
Crystals Observed
L6
Dlin
Intensity
D2nd
diffusion coefficient (10^{-7}cm^2/s)
6.6
5.7
4.8
3.9
3.0
intensity (10^5 cps)
1.10
0.85
0.60
0.35
0.10
0
500
1000
1500
2000
time (min)

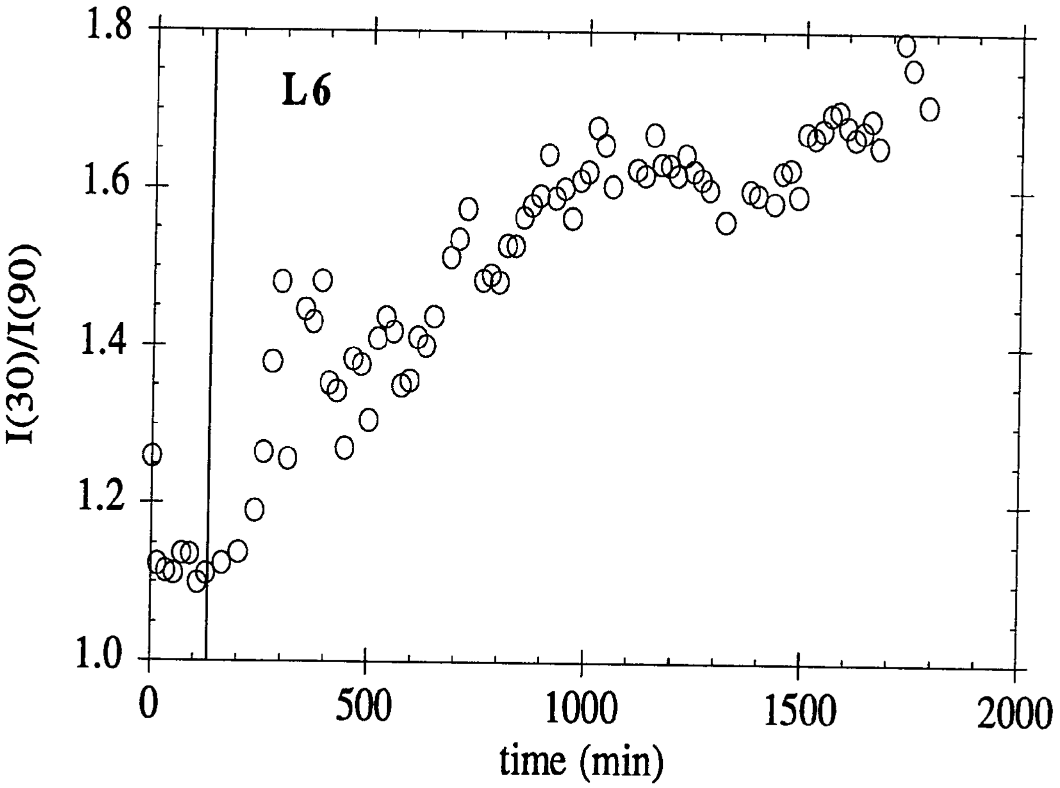

FIG. 25. FS vs time is shown for L6. Note the y axis scale; the behavior is similar to that of L4.

interpret the slight incipient decrease in diffusion that had been observed. According to sedimentation studies at 20°C by Sophianopolus and Van Holde,[91] lysozyme is in a monomeric state at low ionic strength (0.15M KCl) and at pH below 5.5. The dialysis experiments of Wilson[97] using NaCl also show lysozyme to be in a monomeric state at similar conditions.

Multi-q measurements were made at pH 4.5 and at 0.15M NaCl (0.8% w/v). The temperatures were usually 35, 25, 18, and 11°C, but 14, 16, 20, and 22°C were later added. An example of the q dependence, or lack thereof, for two representative conditions is shown as Fig. 26. The average of D_{lin} over q is called D_{eff}. The peak in S(q) has not been observed during this work. At the wavelengths available, all measurements are low q and D_{eff} is on the collective side of q_{max}. The concentration dependence of D_{eff} at the four common temperatures is shown as Fig. 27.

Calculation of D_0 and k_D at these temperatures follows from Eq. (36). The free particle hydrodynamic diameter d_0 is calculated from D_0 and is shown vs T in Fig. 28. Figure 29 shows k_D vs T with an arbitrary parabolic fit. Using $(\partial\pi/\partial c_n)_T = k_B T$ and the viscosity of water, d_{eff} at each concentration was computed from Eq. (33) and is shown vs T in Fig. 30. The deviation from d_0 as T decreases and as concentration increases is demonstrated. This behavior will be explored in the final chapter.

To conclude this chapter, a summary of the sample conditions for the supersaturated lysozyme solutions is presented as Table I. The conditions for the investigation of monomeric lysozyme solutions are summarized in Table II. Except for the temperature steps, which have already been described, each insulin sample was identical and prepared as described in section A.4 of Chapter III.

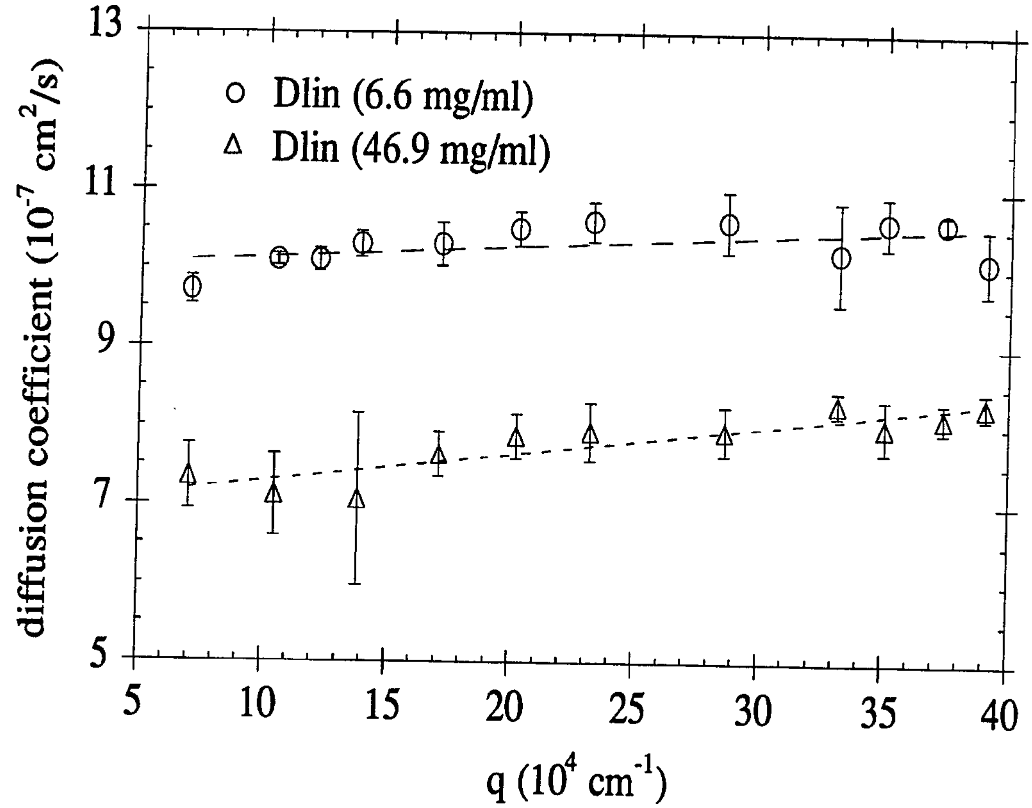

FIG. 26. The figure shows typical results for the monomer studies. The conditions shown are: (upper set) 6.6 mg/ml lysozyme, pH 4.5, 0.8% NaCl, T = 18°C; (lower set) same except 46.9 mg/ml lysozyme. The data were collected at 11 or 12 angles ($20° \leq \theta \leq 150°$) at $\lambda_0 = 413.6$ nm. Each data point is the average of five measurements and is shown with the 95% confidence limit. There is some q dependence evident at the higher concentration but nothing to indicate that q approaches q_{max}. The average over q is termed D_{eff} in the analysis.

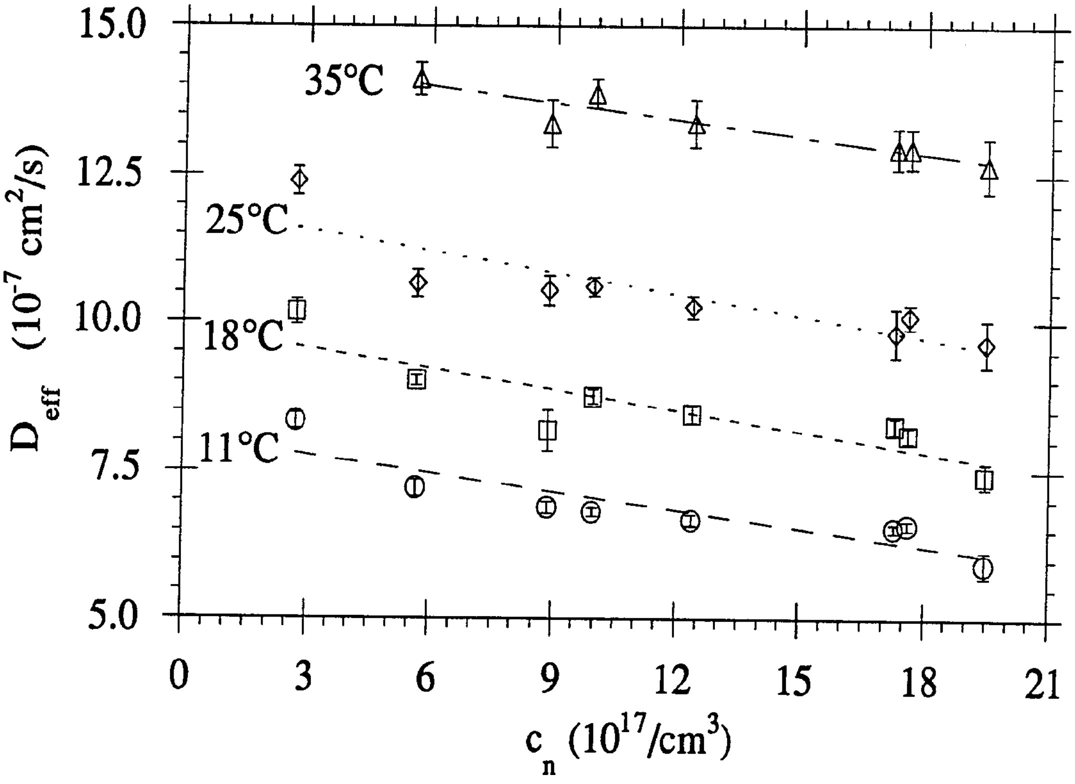

FIG. 27. The concentration dependence of D_{eff} with 95% confidence limits is shown at the four common temperatures. The linear regressions are analyzed via Eq. (36).

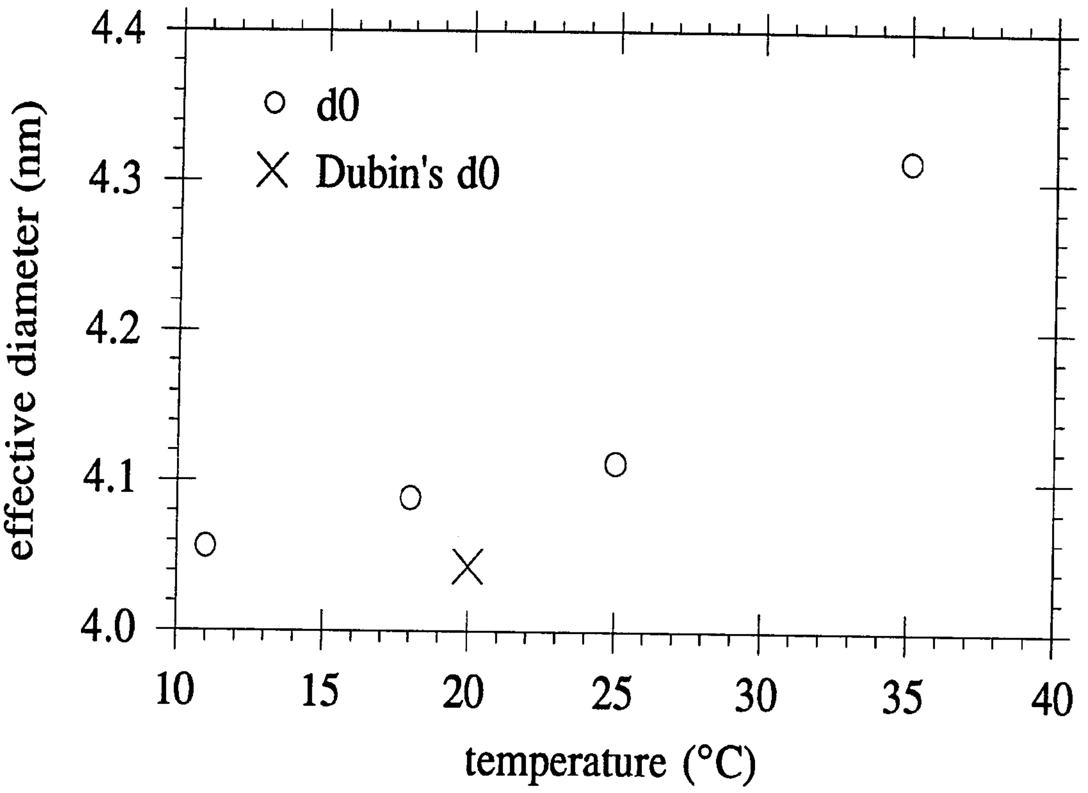

FIG. 28. The free particle hydrodynamic diameter d_0 at the four common temperatures is compared to the value published by Dubin et al.[29]

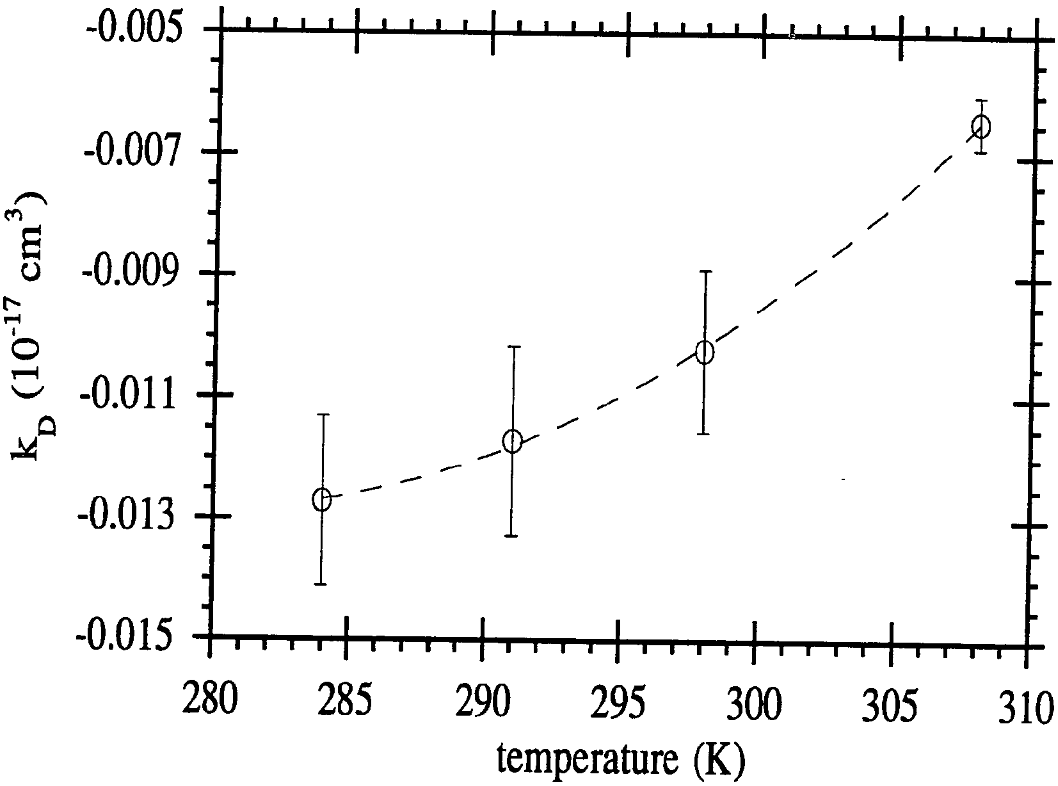

FIG. 29. k_D vs T is shown with an arbitrary parabolic fit.

(a)

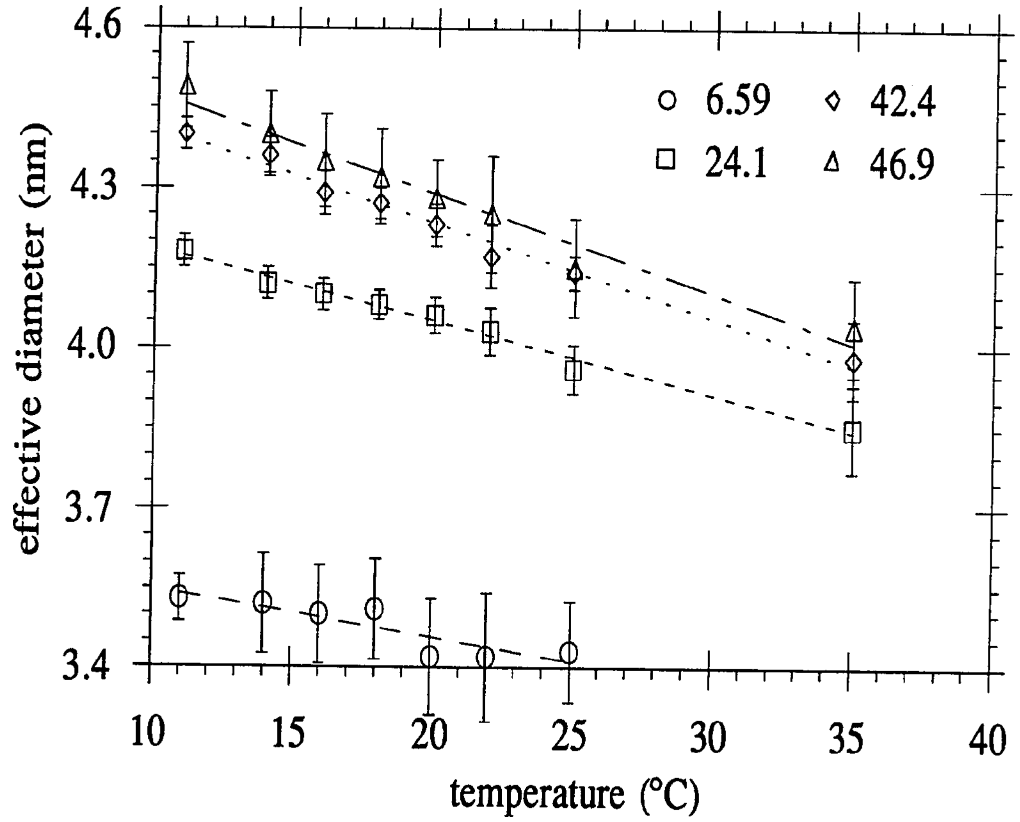

FIG. 30. Concentration and temperature effects on d_{eff} are illustrated. The legends show concentration in mg/ml.

(a) The four complete temperature sets are shown with 95% confidence limits.

(b) All data are shown with error bars removed for clarity. The tendency is clear.

(b)

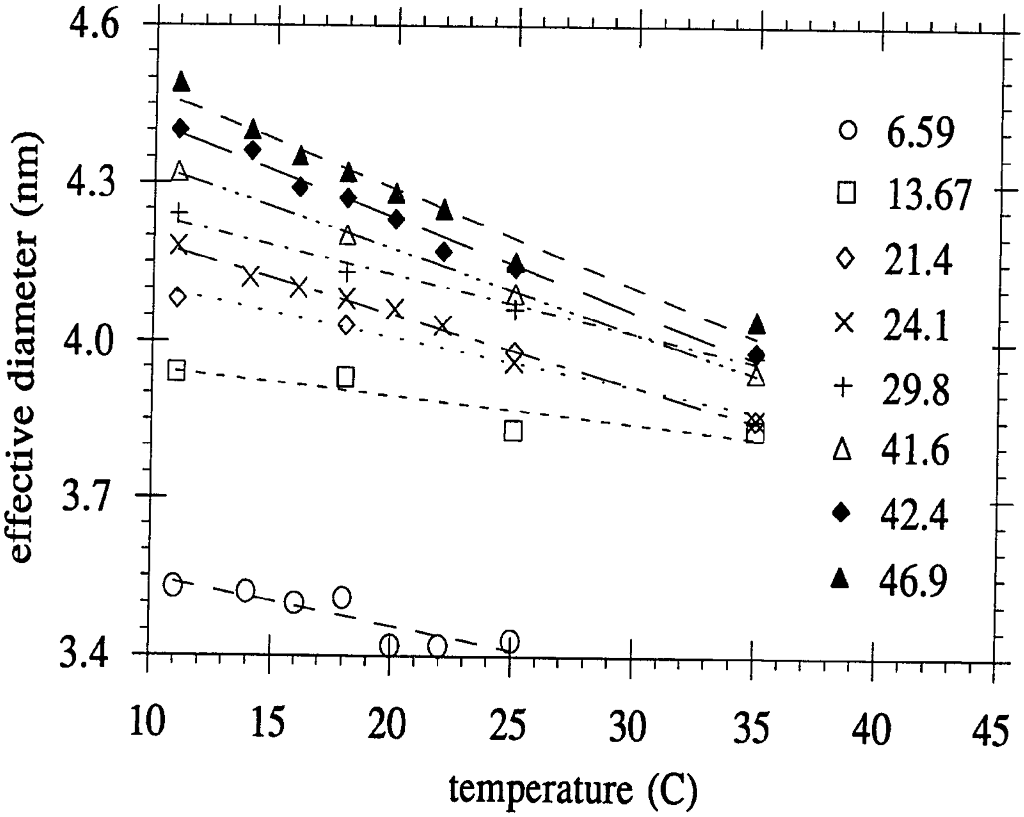
effective diameter (nm)
4.6
4.3
4.0
3.7
3.4
10
15
20
25
30
35
40
45
temperature (C)
○ 6.59
□ 13.67
◇ 21.4
× 24.1
+ 29.8
△ 41.6
◆ 42.4
▲ 46.9

Table I. The conditions of the supersaturated lysozyme solutions are shown with λ_0.

Sample ID (result)	Concentration (mg/ml)	pH	NaCl (%w/v)	Temperature (°C)	λ_0 (nm)
L1 (PRAGG)	6.75	4.4	6.5	30	488
L2 (PRAGG)	6.75	4.4	6.5	30	488
L3 (CRAGG)	16.0	4.4	3.0	35 → 15	488
L4 (CRAGG)	21.0	4.4	3.0	35 → 25 → 20 → 15	488
L5 (CRAGG)	46.9	4.5	2.5	RT → 11 (quenched)	647.1
L6 (CRAGG)	55.7	4.5	3.0	RT → 11 (quenched)	647.1

Table II. The concentrations and temperatures for the investigation of lysozyme at 0.8% (0.15M) NaCl and pH 4.5 are shown. For these measurements $\lambda_0 = 413.6$ nm.

Concentration (mg/ml)	Temperature (°C)							
	11	14	16	18	20	22	25	35
6.59	√	√	√	√	√	√	√	
13.7	√			√			√	√
21.4	√			√			√	√
24.1	√	√	√	√	√	√	√	√
29.8	√			√			√	√
41.6	√			√			√	√
42.4	√	√	√	√	√	√	√	√
46.9	√	√	√	√	√	√	√	√

CHAPTER V

DISCUSSION AND CONCLUSIONS

A. Interparticle interactions within monomeric lysozyme

Before supersaturated solutions are considered, the work with monomeric lysozyme is discussed to give adequate background for the effects of interactions. The presence of interactions in aqueous lysozyme solutions has been shown to influence the long-τ tail of $g_2(\tau)$.[10,39] Interactions have also been considered in other protein systems.[74] The q domain of this work dictates that in the presence of interactions D_{eff} represents the collective diffusion, so d_{eff} represents the collective friction without the known temperature effect of viscosity and does not totally represent a particle size. Consequently, an increase in d_{eff} means that excess friction is being experienced by the scatterers beyond that caused by viscosity changes and not necessarily that the solute particles have increased in size.

The study of D_{eff} vs c vs T of monomeric lysozyme solutions at 0.8% NaCl reveals hydrodynamic interactions to be the dominant interactions. The free particle hydrodynamic diameter d_0 is determined at 35, 25, 18, and 11°C and compared with reasonable agreement to the value calculated from the D_0 published by Dubin, Clark, and Benedek.[29] At this low ionic strength, interactions cause d_{eff} to increase to more than 10% of d_0 as the concentration and temperature approach those of crystallization.

1. The friction as represented by d_{eff}

In crystallizing solutions, interparticle interactions are a surety and must be considered when analyzing crystal growth systems by PCS. This preliminary investigation of interactions was done with lysozyme at pH 4.5 and 0.8% NaCl. It is here assumed that these low ionic strength solutions are monomeric[91,97] at this pH and that particle size is removed from consideration; therefore, a change in d_{eff} reflects a change in friction as effected by interparticle interactions.

The lysozyme monomer exists in solution as a highly charged molecular ion.[83] The net charge is governed by the pH of the solution and is about 10 protons.[83] In solution with a precipitant, NaCl for example, the Coulombic interactions are screened by the small ions of the precipitant.

At zero ionic strength in water Dubin et al.[29] found $D_0 = 10.6 \times 10^{-7}$ cm^2/s to be independent of concentration at 20°C at pH 4.2. This gives $d_0 \approx 4.0$ nm, where d_0 is the free particle hydrodynamic diameter as calculated from D_0. This work measured $D_{eff} = 10.9 \times 10^{-7}$ cm^2/s ($d_{eff} \approx 3.5$ nm) at 20°C and 6.59 mg/ml and demonstrated a distinct concentration dependence in D_{eff} (see Fig. 27). This work differs from Dubin's mainly in ionic strength. Figure 30 shows the concentration dependence of d_{eff} vs T. The lines are linear regressions to the data. It can be seen that at the higher temperatures d_{eff} approaches the value measured by Dubin. The decrease in diffusion as concentration increases (i.e., $k_D < 0$) is evident by the increase in d_{eff} with concentration at each T, but Fig. 30 also shows that as concentration increases so does the temperature dependence of d_{eff}. This is illustrated by Fig. 31 which shows the slope of the regressions versus concentration. The slope of the regression, $\Delta d_{eff}/\Delta T$, represents the prominence of the interactions at that

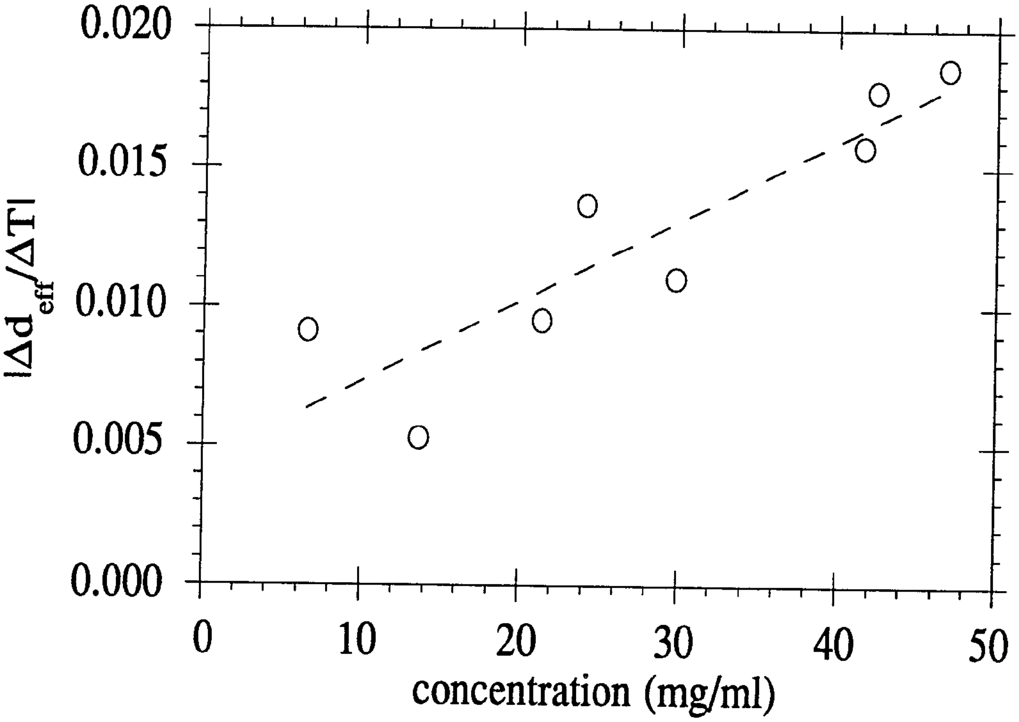

FIG. 31. The magnitude of the slopes of the regressions of Fig. 30 is plotted vs c. As concentration increases, $U_i(R)$ becomes comparable to KE and has a greater influence on d_{eff} as T is decreased. Note: the four data points lying above the regression are from the complete temperature sets of Fig. 30(a).

concentration, whereas k_D reflects the prominence of interactions at a particular T. The overall interaction potential energy $U_i(R)$ is not comparable to the kinetic energy in the dilute solutions, so $\Delta d_{eff}/\Delta T$ is small. As the nearest neighbor intermolecular distance R decreases with increasing concentration, $U_i(R)$ increases. When R is such that $U_i(R)$ is comparable to k_BT, $\Delta d_{eff}/\Delta T$ increases. Therefore, at high concentrations $U_i(R)$ detectably influences the friction. Table III summarizes these effects. At the lower concentrations the deviation in d_{eff} is less than 3% over the measured T range. The deviation increases to more than 10% as the concentration is increased to that of crystallization.

2. Discussion of D_0 and k_D

Mikol[64] concluded that there was no concentration dependence to the lysozyme diffusion coefficient in undersaturated solutions. In contrast, this work yielded a readily reproducible $k_D < 0$. The linear regressions of D_{eff} vs c_n in Fig. 27 yield the k_D values illustrated in Fig. 29 and shown in Table IV. Table IV also shows D_0 as calculated from the regression at each T and d_0 as calculated from D_0. Figure 28 shows d_0 vs T. At 11, 18, and 25°C there is reasonable agreement with Dubin's value for the monomer. As should be the case, these three values do not vary greatly with T, but d_0 at 35°C is an exception. The considerable disagreement at 35°C is caused by the lack of the 6.59 mg/ml data point in D_{eff} vs $<c>$. This data point was high at each T as clearly seen by low d_{eff} values at this concentration in Fig. 30. If such a high data point were included in the regression calculation at 35°C, then the slope and intercept would increase giving a larger value for D_0 and a smaller value for d_0. This would also decrease the value of k_D to below the parabola of Fig. 29. Nonetheless,

Table III. The variation in d_{eff} due to temperature and concentration is summarized.

Concentration (mg/ml)	d_{eff} (35°C) (nm)	d_{eff} (11°C) (nm)	% difference
6.59	3.43*	3.53	2.8
13.7	3.83	3.94	2.9
21.4	3.85	4.08	6.0
24.1	3.85	4.18	8.6
29.8	3.97	4.24	6.8
41.6	3.94	4.32	9.6
42.4	3.98	4.4	10.6
46.9	4.04	4.49	11.1

* T = 25°C

Table IV. The linear regressions of Fig. 27 coupled with Eq. (36) yield these values of D_0 and k_D. Use of Eqs. (28) and (29) yield d_0 from D_0.

Temperature (°C)	D_0 (10^{-7} cm^2/s)	d_0 (nm)	k_D (10^{-20} cm^3)
35	14.5	4.31	-6.44
25	11.9	4.11	-10.22
*20	*10.6	4.04	
18	9.9	4.09	-11.71
11	8.1	4.06	-12.70

* Dubin et al.[29]

when d_0 is averaged over the measured temperatures, the 95% confidence limits encompass the Dubin value as illustrated in Fig. 32.

These measurements of monomeric lysozyme show that U_i influences PCS measurements at high concentrations and at low T, where $U_i(R) \sim k_BT$. These conditions at higher ionic strength support nucleation. The nature of U_i may be addressed from k_D as measured here and from the theory of Anderson and Reed.[3] It is evident from $k_D < 0$ that the shorter ranged hydrodynamic interactions, which cause diffusion to decrease with increasing c_n, are dominant over the longer ranged Coulombic repulsive interactions, which increase diffusion with increasing c_n. Although the data are insufficient to quantify the two and define U_i, it is clear that even with little ionic screening the hydrodynamic property is more prominent. If the Coulombic potential is further screened as is the case at nucleation, then the hydrodynamic interactions may have a critical influence on the nucleation event.

B. Supersaturated lysozyme solutions

The supersaturated lysozyme samples L1 - L6 show that there is a distinct difference between the light scattering profile during the formation of PRAGG's (L1 and L2) and the profile during the formation of CRAGG's (L3 - L6). The data from CRAGG samples show that the nucleation event can be detected and monitored by single-τ d_{eff} in clean, tetragonal systems. During isothermal nucleation an increase in d_{eff} of 7% is discernable as is an increase in absolute intensity. Based on available information cartoons depicting the aggregate size distributions are offered in the following discussions. The scatterer is considered to be an aggregate j-mer characterized by j. The distributions are meant only for illustration

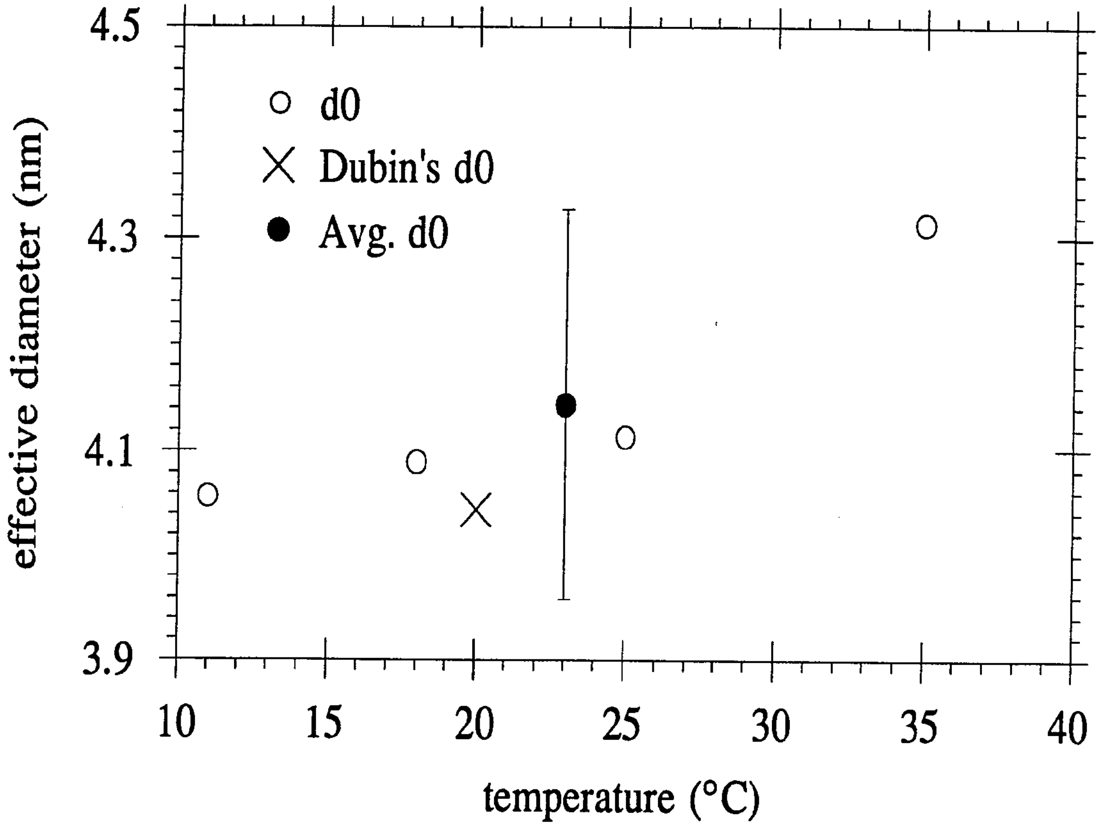

FIG. 32. The 95% confidence limit of the measures of d_0 are seen to encompass the Dubin[29] value.

to provide an idea of the order of magnitude of the sizes involved in the processes.

1. PRAGG's

The appearance of PRAGG's is demonstrated by samples L1 and L2 (and the sample of Fig. 13). PRAGG formation is marked by a large increase in d_{eff} and in FS. The initial values of d_{eff} were near d_0 and those of FS were near one. Maximum values, which were two or three times the initial values, were reached as shown in Figs. 15 and 16 and as presented in Table V. They remain near this maximum. In some cases, a slight decrease in d_{eff} from the maximum was observed over a long period of time [see Figs. 15(b) and 16(a)], but d_0 was never again approached. Here, d_{eff} was calculated from D_{2nd}.

Recall that cases (2) and (3) of Kam and Feher predict the formation of PRAGG's. In these solutions there is no quasiequilibrium, and $t_d = 0$. As presented in Chapter IV there were solutions that precipitated so quickly that scattering measurements were impossible. The resulting amorphous precipitate confirmed that these were case (2) solutions. The solutions that were measurable (e.g., L1 and L2) did not result in a visual precipitate of any kind and were probably case (3). After the scattering measurements, microscopic examination of L1 and L2 at 10x magnification showed no discernable particles, so case (3) PRAGG's are submicroscopic yet are detectable by light scattering. Both FS and d_{eff} continuously increase to a maximum value of more than twice the initial value. Case (2) solutions also yield PRAGG's, but these become visible and aggregate too quickly to be measurable by light scattering.

PRAGG's are favored when supersaturation is achieved by high ionic strength at low lysozyme concentration and when samples at higher

Table V(a). The behavior of d_{eff} during PRAGG formation is summarized.

Sample (mode)	d_{init} (nm)	d_{max} (nm)	d_{final} (nm)	d_{max}/d_{init}	t_{max} (min)
L1 (single-τ)	4.6	12.5	9.4	2.7	3500
L1 (multi-τ)	no data	35.3	31.0	no data	3500
L2 (single-τ)	4.4	24.8	19.0	5.6	700
L2 (multi-τ)	5.9	100	100	16.9	700

Table V(b). The forward scattering behavior during PRAGG formation is summarized.

Sample	FS_{init}	FS_{max}	FS_{final}	FS_{max}/FS_{init}	t_{max} (min)
L1	1.05	3.00	2.51	2.8	3500
L2	1.05	5.91	5.06	5.6	700

lysozyme concentration and lower ionic strength (which would otherwise yield CRAGG's) are improperly mixed during preparation. The linear nature (see Fig. 3) of the PRAGG's as asserted by Kam and Feher allows for many possible conformations in solution; most of which are probably present in these amorphous systems. Therefore, this work does not attempt to quantitatively relate *j* to the size and shape of an aggregate, but the following is offered as a qualitative explanation of the results.

Figure 14 shows that Mie particles appeared and increased in size. If one were to assume that the linear aggregates coil up into spherical shapes, then an aggregate would begin to exhibit forward scattering for j $O(10^5)$. Linear chains would also exhibit forward scattering for these *j*. Figures 15(b) and 16(a) show that FS and d_{eff} continuously increased from initial values FS_{init} and d_{init} to maximum values FS_{max} and d_{max} in the approximate time t_{max} and then decreased to final values FS_{final} and d_{final}. In these PRAGG systems, $FS_{final} < FS_{max}$ and $d_{final} < d_{max}$, but the final values did not approach the initial values. Figures 15(c) and 16(b) show that d_{eff} for both single-τ and multi-τ measurements behaved in this manner. However, over time these two values increasingly disagree, and the multi-τ value is always the larger. Table V is presented as a summary of these characteristics for the PRAGG samples.

As discussed in Chapter II, the domain of $g_2(\tau)$ governs the fluctuation time scale observed. For a broad, size polydisperse distribution, a single-τ measurement will only be sensitive to a certain region of the distribution as demonstrated in Fig. 33(a). The multi-τ correlation function broadens this region or "window" as demonstrated in Fig. 33(b), so d_{eff} computed from multi-τ measurements is influenced by a broader window encompassing larger sizes. This yields larger values for

FIG. 33. The range of fluctuations that a PCS measurement is sensitive to depends on the domain of $g_2(\tau)$. The regions of sensitivity or "windows" for the single-τ and multi-τ measurements are contrasted.

(a) The single-τ is sensitive to the smaller sizes of a continuous size distribution.

(b) The multi-τ extends the domain of $g_2(\tau)$ without great sacrifice in sensitivity to the smaller sizes.

(a)

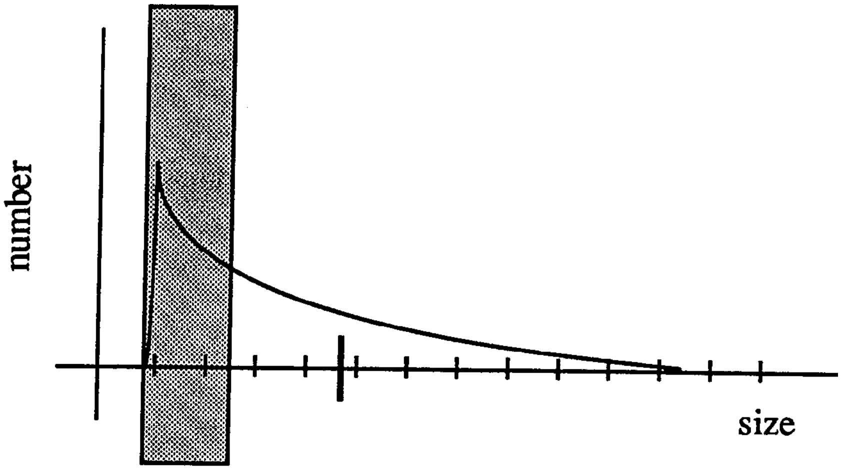

(b)

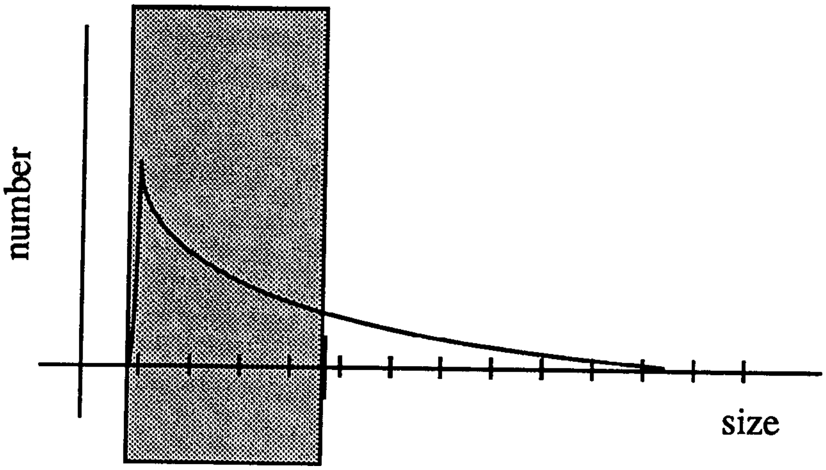

multi-τ d_{eff}. The decrease in single-τ d_{eff} that is evident at long times in Figs. 15(b) and 16(a) is probably due to the size distribution moving beyond the window of those correlation functions as demonstrated in Fig. 34.

The cartoon in Fig. 35 is proposed to depict the evolution of the normalized size distribution over time as evident from the data. At first, the distribution is narrowly distributed, peaked at the value of the monomer, and probably slightly skewed to larger sizes due to the presence of aggregates with *j* O(10^1). As aggregation proceeds, the distribution becomes more and more skewed to the larger sizes, and the Mie size regime is approached. Finally, the aggregates enter the Mie regime and slowly redistribute themselves about a second average, which is greater than the first and probably near the Mie regime (at $\lambda_0 = 488$ nm).

The data for L1 and L2 are consistent with this continuously broadening size distribution, but a visually observable precipitate did not form. Consistent with case (3) Kam and Feher solutions, this suggests that microscopic PRAGG's were not favored. The maximum value of the multi-τ d_{eff} shown in Fig. 16(b) is about $0.1\mu m$, which is well below the capabilities of ordinary white light microscopy. Even though these case (3) aggregates are submicroscopic, they are considered large aggregates by this work. A criteria for the terms small, medium, and large as used in this qualitative discussion is set in Fig. 36. Large aggregates were not evident in CRAGG systems.

2. CRAGG's

The light scattering profile of CRAGG's is demonstrated by samples L3, L4, L5, and L6. Nucleation was marked by a sharp increase in d_{eff} in all cases. After crystals became visible, a maximum was reached and

FIG. 34. A normalized size distribution is seen moving past a single-τ window.

(a)

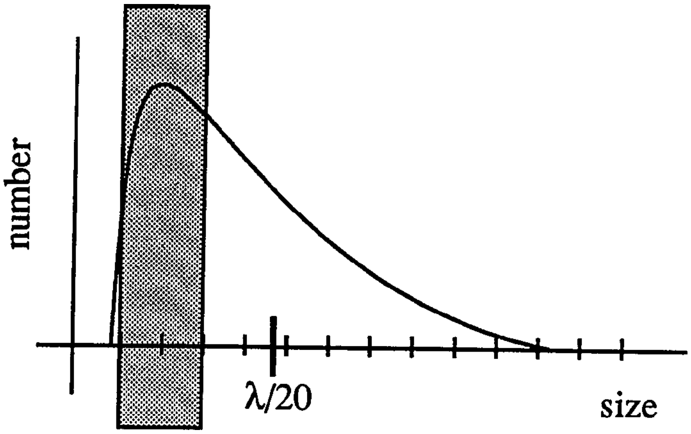

(b)

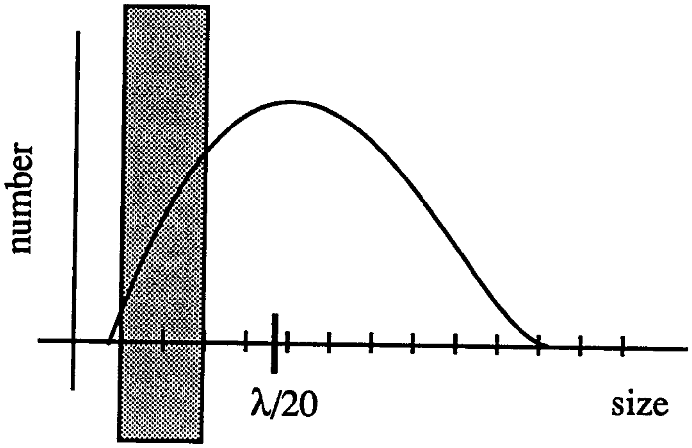

(c)

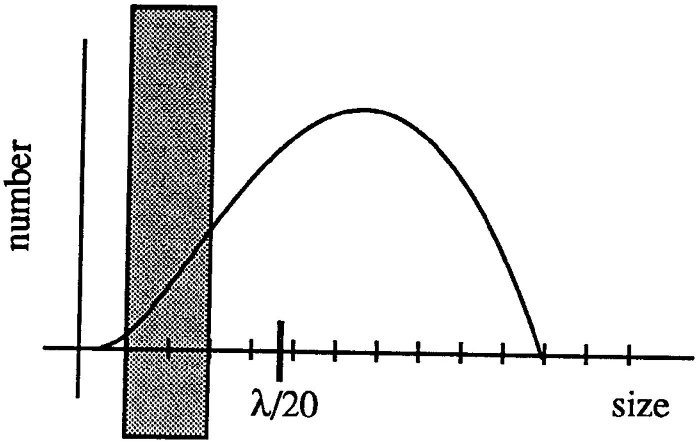

FIG. 35. The evolution of the PRAGG distribution is depicted.

(a) The system begins with monomers and some small j-mers. The aggregate sizes increase at the expense of the monomers and small PRAGG's. The Mie regime is reached by the larger aggregates.

(b) Aggregation continues until the distribution is skewed to the Mie regime. The particles are still invisible through an ordinary desk top microscope at 10x.

(a)

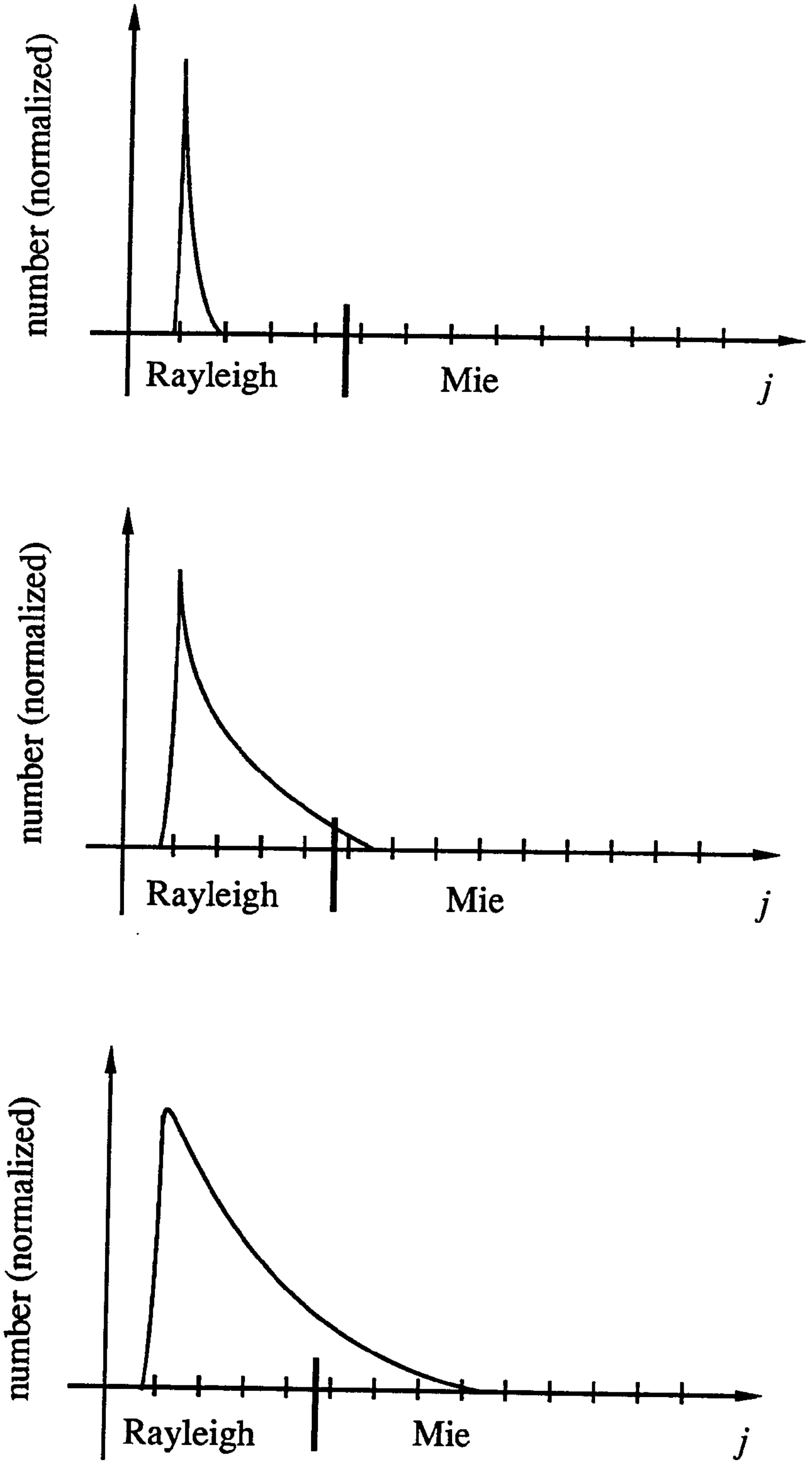
number (normalized)
Rayleigh
Mie
j
number (normalized)
Rayleigh
Mie
j
number (normalized)
Rayleigh
Mie
j

(b)

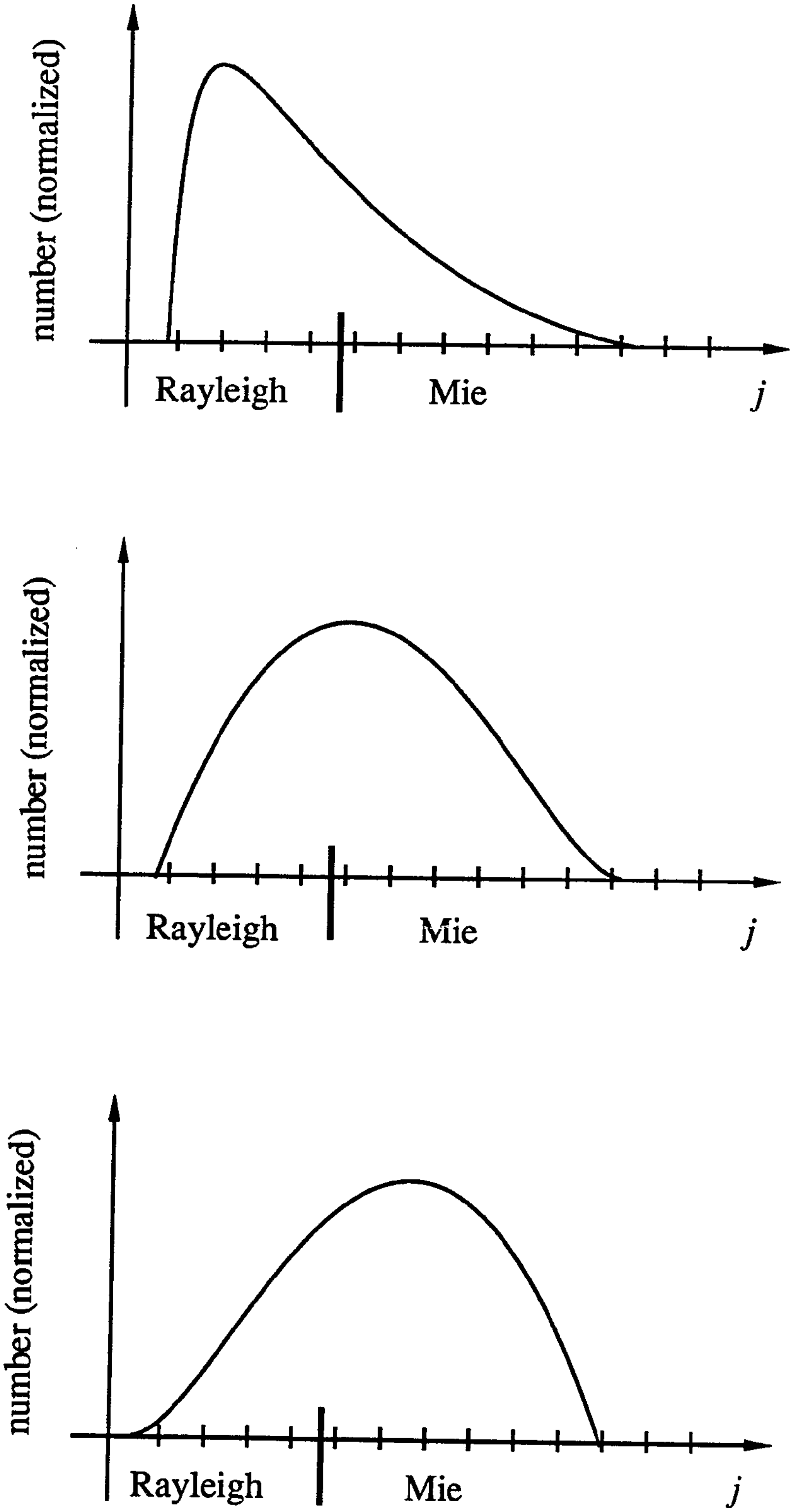
number (normalized)
Rayleigh
Mie
j
number (normalized)
Rayleigh
Mie
j
number (normalized)
Rayleigh
Mie
j

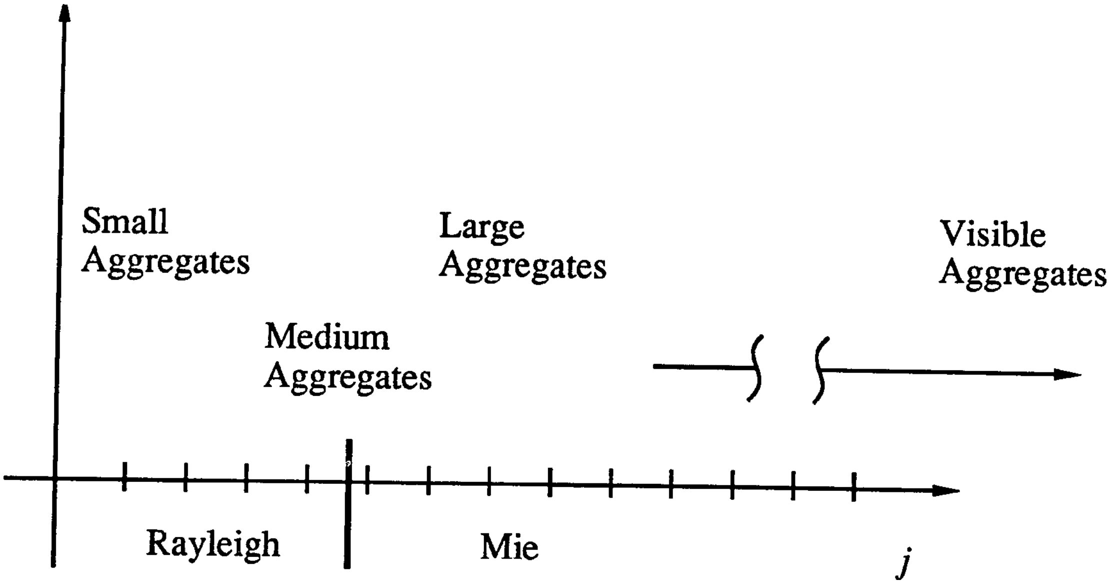

FIG. 36. The criteria are set for the meaning of the terms small, medium, and large as used in the discussion.

maintained for a time. In L3 and L4, d_{eff} then decreased to near the original value. In L5 and L6, d_{eff} decreased below the initial value and approached an asymptotic value. A discussion of L3 through L6 follows.

Sample L3 (Fig. 17) was inserted undersaturated at $T_{init} = 35°C$. The first measurement session was completed, and the sample was held at T_{init} overnight. The next morning a measurement session was done, and T was dropped to 15°C. About 20 min were allowed for the temperature to equilibrate before the next session. Crystals appeared as tiny scintillations on the cuvette walls approximately 70 min after ΔT. Sessions continued throughout the day. The sample was held at 15°C overnight, and measurements were made again the following morning.

Figure 17(c) shows that there is disagreement between the single-τ d_{eff} and the multi-τ d_{eff} during the initial measurement and that during later measurements the two values roughly coincide. The initial value in Fig. 17(a) shows some forward scattering, but during the temperature drop, FS does not deviate significantly from one. During nucleation there is an 18% increase in both single-τ d_{eff} and multi-τ d_{eff}. After a period of time, both d_{eff} return to their original values near d_0.

The initial forward scattering and initial disagreement between single-τ d_{eff} and multi-τ d_{eff} may have been due to small bubbles induced during filtration. These bubbles could influence the long time tail of the multi-τ correlation function and leave the single-τ unaffected. Another possibility is that aggregates are present initially and break up while being held at 35°C. The former is more likely.

The increase in d_{eff} during nucleation and the subsequent decrease is of interest. The crystallization occurred so rapidly in sample L3 that L4 (Fig. 18) was stepped down in temperature. Figure 18(d) shows the data of

L4 on a smaller scale. The difference in solution parameters was that L3 had 16 mg/ml lysozyme, whereas L4 had 21 mg/ml. A sharp increase in d_{eff} is again apparent during nucleation.

For L4, Single-τ d_{eff} and multi-τ d_{eff} [Fig. 18(c)] showed good agreement during the initial scattering session. During the next morning's session, both showed an increase from the evening before but deviated from one another. Single-τ d_{eff} increased 30% while being held at 35°C, and multi-τ d_{eff} increased by 80%. There was some change in both single-τ d_{eff} and multi-τ d_{eff} as T was decreased to 25°C and then to 20°C but nucleation was seen to occur as 15°C was reached. Single-τ d_{eff} behaved similarly to that of L3, but the multi-τ d_{eff} did not decrease after crystals formed, and the increase in d_{eff} during nucleation was of greater magnitude, 32% for single-τ d_{eff} and 62% for multi-τ d_{eff}. Sample L4 also showed FS increasing during nucleation [Fig. 18(a)] but to a much lesser extent than the PRAGG samples L1 and L2. More crystals formed in L4 than in L3 but they appeared 130 min after 15°C was reached.

The initial agreement between single-τ d_{eff} and multi-τ d_{eff} for L4 was likely due to allowing 120 min after filtration for microbubbles to dissipate before the first measurement session. The subsequent increase at constant T indicates a time dependence to the quasiequilibrium state. However, the increase in FS [Fig. 18(a)] and the failure of multi-τ d_{eff} [Fig. 18(c)] to return to its initial value support the possibility of PRAGG formation. Nonetheless, nucleation was detectable. The changes in single-τ d_{eff} and multi-τ d_{eff} as T was decreased to 25°C and then to 20°C occurred as the preCRAGG's (with or without PRAGG's) achieved a new quasiequilibrium at the new T. The presence of PRAGG's, which deplete the nutrient, could have caused the delay in the appearance of crystals.

Data from the next two samples to be discussed, L5 and L6, were collected at UAH. The purpose of these experiments was not to evaluate changes in quasiequilibrium, but rather to investigate isothermal changes in diffusion for $t > t_d$.

Samples L5 and L6 were prepared undersaturated at room temperature. At $t = 0$ they were dropped to 11°C at which point they were supersaturated to an extent that $t_d \rightarrow 0$. Measurements began at $t = 0$ and the sample equilibrated to 11°C in less than 4 min as determined in duplicate experiments. Sample L6 was measured at a greater degree of supersaturation than was L5 (see Table I). The behavior of the diffusion within these samples is shown in Figs. 22 and 24. Note that the intensity is included in these figures. Intensity is not shown for the UAB samples because the laser power was not kept constant as was done at UAH. Multi-τ measurements were not made at UAH.

The profile of the isothermal diffusion in CRAGG systems is evident from these two examples. Figures 22 and 24 show that D_{2nd} and D_{lin} decreased to a minimum during nucleation. This decrease in diffusion was accompanied by an increase in I. The values of D_{2nd} and D_{lin} paralleled each other and maintained nearly identical values throughout the experiments. Shortly before the minimum was reached, crystals became visible. The diffusion then increased to an asymptotic value. Once again the solution with the higher degree of supersaturation showed some increase in forward scattering, but as shown in Figs. 37 and 38, there was no angular dependence to the diffusion coefficient. A polydisperse system containing Mie aggregates is expected to yield a decreasing diffusion coefficient for decreasing q since Mie particles scatter more effectively into the forward angles and give a greater contribution to $g_2(\tau)$.

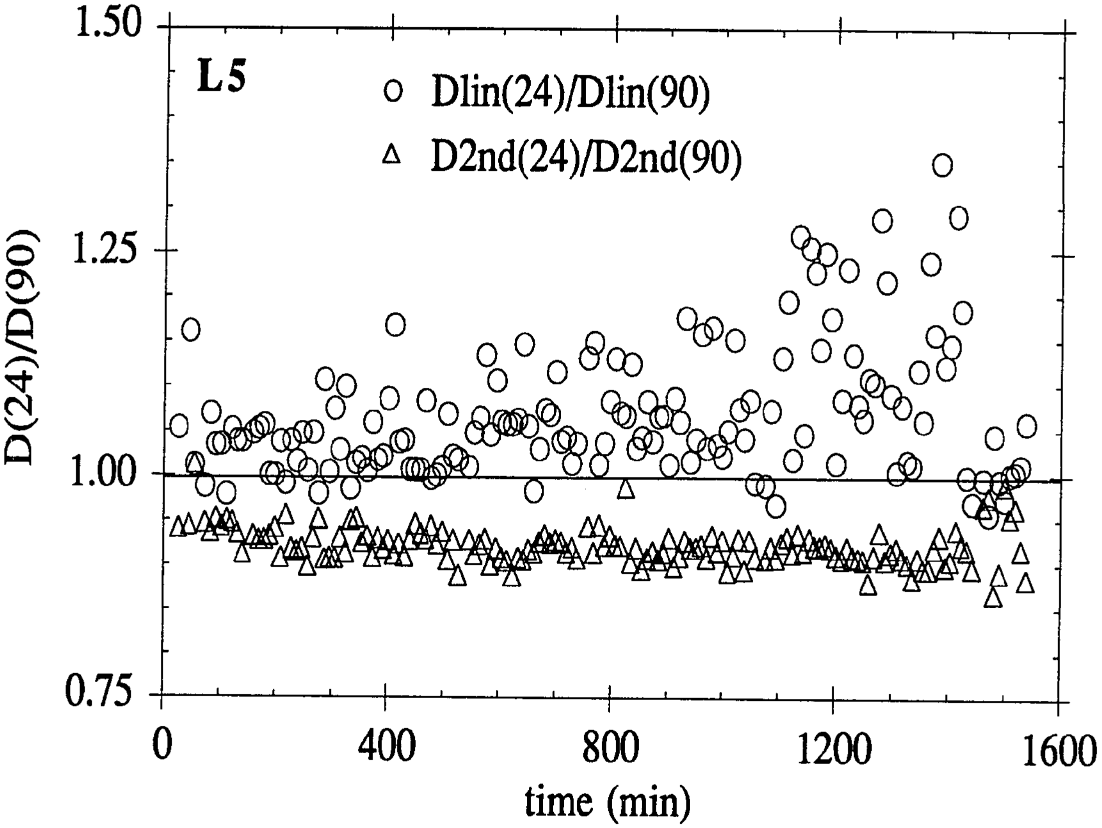

FIG. 37. The ratio of the diffusion coefficients measured at the forward angle to those of the rearward angle is plotted for L5. This illustrates a lack of q dependence.

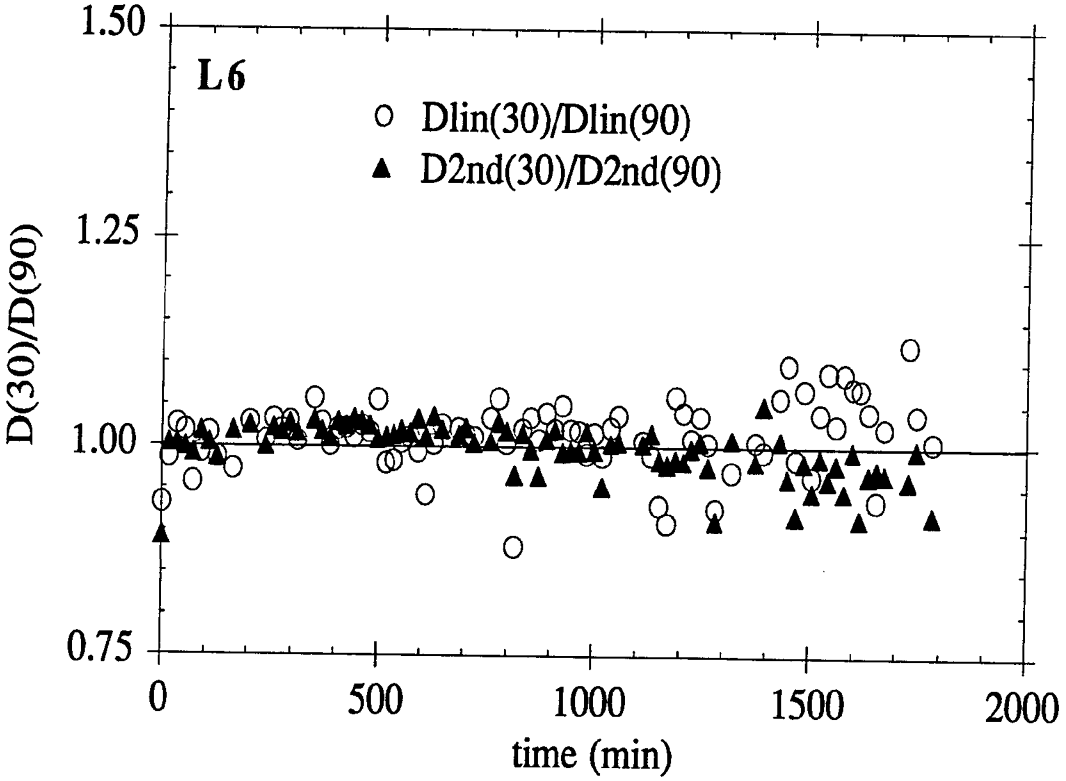

FIG. 38. The ratio of the diffusion coefficients measured at the forward angle to those of the rearward angle is plotted for L6. This illustrates a lack of q dependence.

Tables VI and VII present a summary of the CRAGG behavior. The data of Figs. 17, 18, 22, and 24 provide the general CRAGG profile. The results of L5 and L6 are in general agreement with those of L3 and L4, so with the exception of multi-τ d_{eff} for L4, all CRAGG profiles were consistent. To see the profile consider only the single-τ results of L3 and L4, and see D_{2nd} converted to d_{eff} for L5 and L6 in Figs. 39 and 40. In each case d_{eff} is at an initial value d_{init} and begins to increase as nucleation commences. (Note: for L3 and L4, d_{init} is the first value at T = 15°C.) As d_{eff} increases, crystals become visible at time t_{cryst}. The maximum d_{max} is reached at time t_{max}, and a decrease to d_{final} such that $d_{final} \leq d_{init}$ is then evident. Figure 40 illustrates these quantities for L5. The single-τ measure of d_{eff} shows consistent behavior in each CRAGG sample because the window [Fig. 33(a)] of this measure is open to the preCRAGG's.

The formation of CRAGG's was not necessarily marked by an increase in FS. Samples L4 and L6 did show FS increase from one, but the behavior did not parallel that of d_{eff} as it had with the PRAGG solutions. However, L4 did show similar behavior between FS and multi-τ d_{eff}.

3. PRAGG's vs CRAGG's

Comparison of Table V with Tables VI and VII shows the distinction between the light scattering profile for PRAGG's and that for CRAGG's. The magnitude of the initial increase in d_{eff} is two or three times greater for PRAGG's than for CRAGG's. Forward scattering marks the formation of PRAGG's but is not necessarily detectable during the formation of CRAGG's. For PRAGG's $d_{final} \approx d_{max}$, but for CRAGG's $d_{final} \leq d_{init}$.

The work with lysozyme indicates that CRAGG solutions do not necessarily contain a significant number of Mie scatterers although medium size aggregates may appear. The low ratio d_{max}/d_{init} also indicates that

Table VI. Results from the PCS measurements during crystallization are summarized by these monitoring parameters. These parameters are illustrated in Fig. 39.

Sample (mode)	d_{init} (nm)	d_{max} (nm)	d_{final} (nm)	d_{max}/d_{init}	t_{cryst} (min)	t_{max} (min)	Δt_{max} (min)
L3 (single-τ)	4.3	5.1	4.3	1.19	1110 70 at 15°C	1150 110 at 15°C	60
L3 (multi-τ)	4.4	5.2	4.3	1.18	same as single-τ	same as single-τ	same as single-τ
L4 (single-τ)	6.3	7.5	5.5	1.19	1800 130 at 15°C	2030 360 at 15°C	150
L4 (multi-τ)	7.4	14.7	14.7	1.99	same as single-τ	did not peak	did not peak
L5 (single-τ)	6.9	7.4	6.2	1.07	130	215	415
L6 (single-τ)	8.5	9.1	5.2	1.07	140	135	200

Table VII. The forward scattering behavior of L3 - L6 during crystallization is summarized.

Sample	FS_{init}	FS_{max}	FS_{final}	FS_{max}/FS_{init}	t_{max} (min)
L3	1.08	1.11[a]	1.09	1.02	did not peak
L4	1.10	1.77	1.66	1.61	2320
L5[b]	1.12	1.14[a]	1.09	1.02	did not peak
L6	1.12	1.70	1.70	1.52	increased to final value

[a] maximum values only; FS vs t did not show a maxima.

[b] FS = I(24)/I(90)

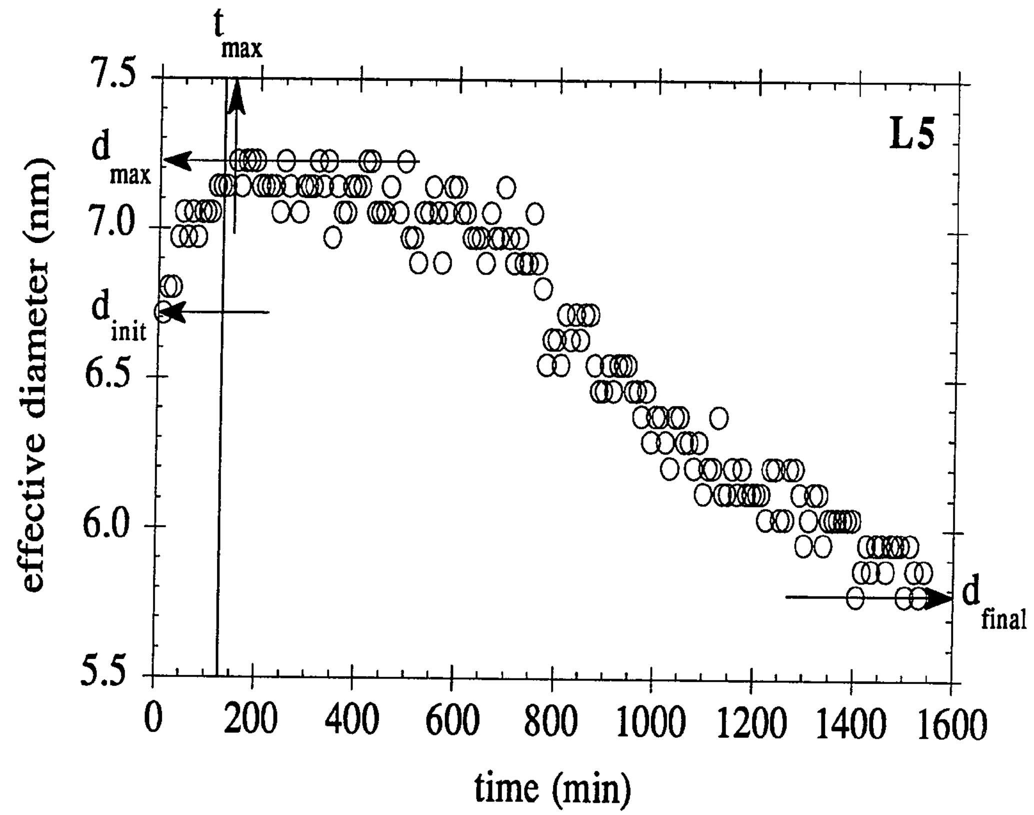

FIG. 39. Shown for L5 is d_{eff} at $\theta = 45°$ as computed from D_{2nd}. As shown in the previous figures there was little angular dependence, so these data are representative of L5.

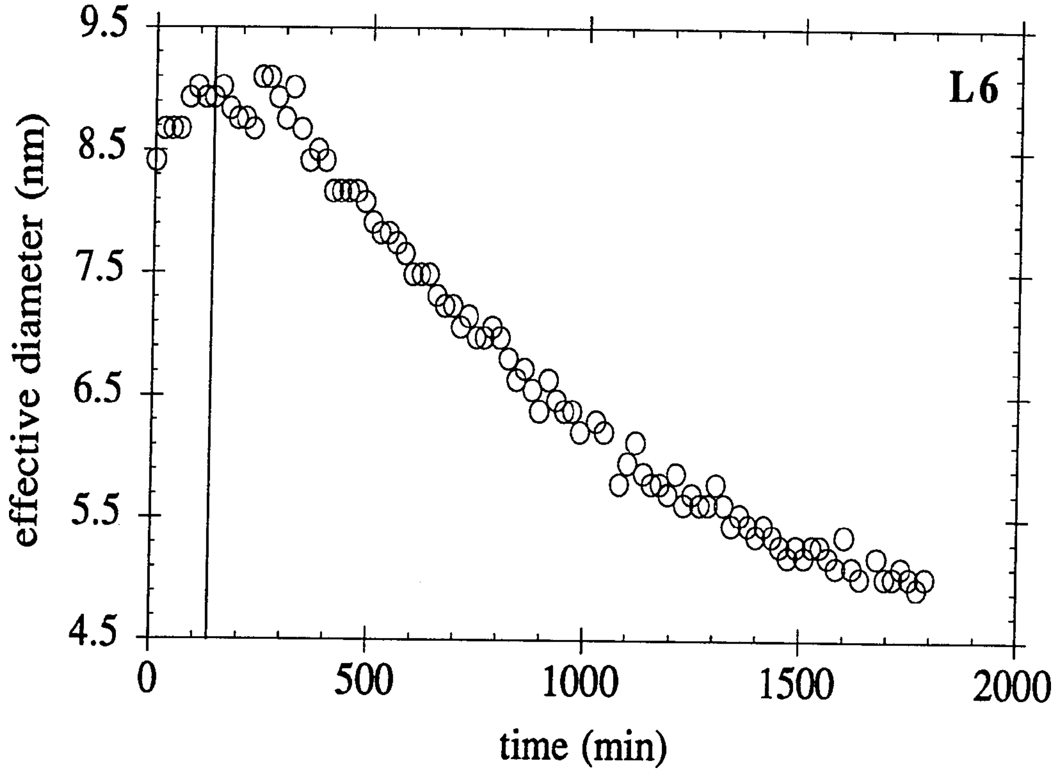

FIG. 40. Shown for L6 is d_{eff} at $\theta = 60°$ as computed from D_{2nd}. As shown in the previous figures there was little angular dependence, so these data are representative of L6.

large scatterers do not form homogeneously throughout the solution during nucleation. Although crystals form and grow to visible sizes, they do not necessarily do so in the scattering volume (see Fig. 41) or on a time scale accessible by these PCS measurements. Inconsistent polydispersity values and the absence of an angular dependence to the diffusion coefficient indicate that CRAGG distributions are narrow about a small mean. These distributions are discussed in section D.1 below.

To summarize, the work with supersaturated lysozyme solutions demonstrated the difference between PRAGG and CRAGG distributions and has given valuable insight into the nature of the CRAGG system which will be discussed as conclusions. The work with insulin was not as productive.

C. Discussion of results from protamine insulin

Results from supersaturated protamine insulin solutions demonstrate that nucleation can be detected, but not monitored by PCS in a system that has such a high density of nucleation sites that they appear as flashes within the scattering volume. During this active period baselines for the correlation functions were rarely obtainable; however, it was often possible to measure FS. Before the active period ended the cuvette walls became cloudy, and posterior microscopic observation revealed many small (< 0.1 mm) crystals attached along with precipitate. The appearance of this cloudiness is noted in the figures as the appearance of crystals, but amorphous precipitate formed in equal or greater proportions in every case. From this point on the detector was somewhat obscured, and results from further measurements are questionable. However, they are reported when baseline agreement and low dust rejection were achieved. The available data indicate that d_{eff} and FS increased to more than twice the

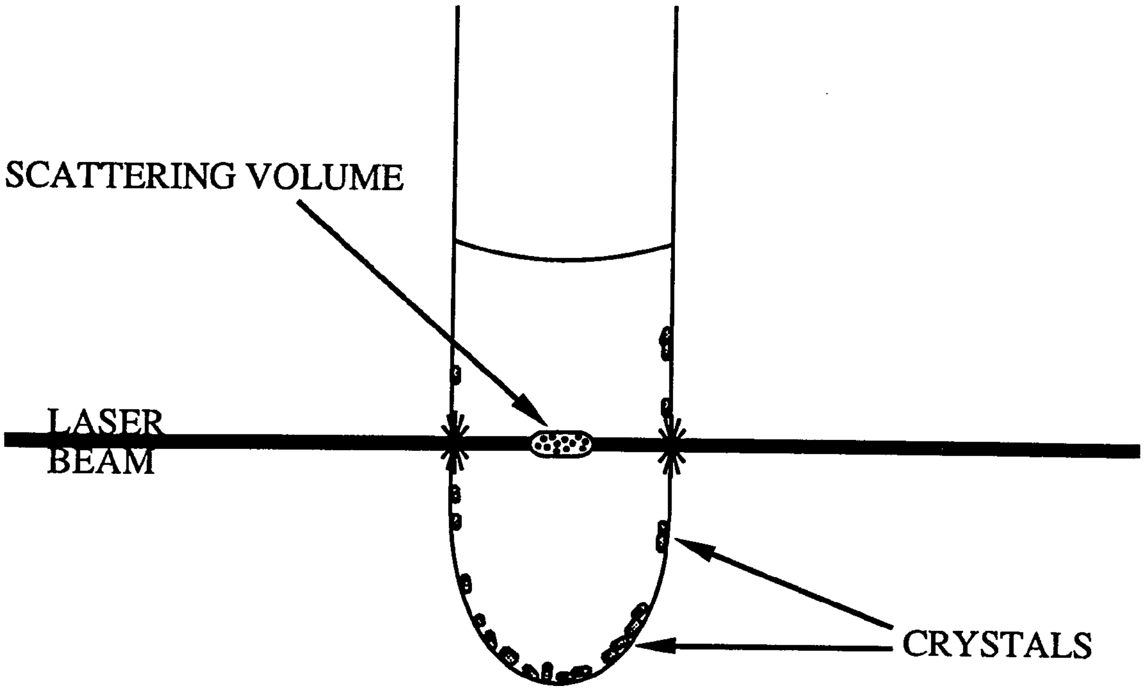

FIG. 41. The scattering volume is shown in relation to the growing crystals. The scattering measurement does not actually include information on the growing crystals. Only the behavior within the bulk solution is observed.

initial value after the appearance of crystals. The increase is consistent with the PRAGG profile of lysozyme, but the more subtle CRAGG profile has not been observed in insulin samples.

In each case, the active period signaled nucleation, and large aggregates became increasingly present after nucleation. The onset of the active period and its duration were totally unpredictable even though each sample was prepared identically. Samples I1, I2, and I3 demonstrate this. The active period for I1 began at 30°C and continued for more than two days (see Fig. 19). Sample I2 became active immediately upon reaching 26°C, but remained active for less than four hours (see Fig. 20). For I2 the active period was mild and FS could be measured. Figure 20(a) shows that FS increased only after crystals appeared. Sample I3 (Fig. 21) became active for about 90 min at 40°C, and the temperature was not reduced.

The data show that large aggregates appeared after crystals were visible suggesting that PRAGG's formed after the CRAGG's. The formation of CRAGG's, which went unmonitored during the active period, may have reduced the state of supersaturation to a point favorable for insulin PRAGG formation. The PRAGG's continued to grow after the crystals stopped. This growth situation is detrimental to the final product. After crystals form, the PRAGG's deplete the nutrient causing premature cessation of growth. The crystal face may also be etched as the crystal tries to replenish the nutrient.

The active period indicates that in these insulin samples, critical nuclei formed throughout the solution, even in the scattering volume, due to their sheer number. The scintillations from the scattering volume, although verifying nucleation, denied any quantification of the event. Also, the nuclei formed so quickly that measurements, as they were performed at that time, could not quantify the events preceding the active period. Although automated data collection as used for L5 and L6 could adequately monitor the events preceding the active period, the utility of light scattering for fundamental investigation of nucleation is limited with this type of sample. However, simple verification of nucleation is of importance to DCPCG.

To summarize, the inconsistency of protamine insulin samples caused much frustration, but there has been some gain. Measurement of CRAGG formation was obscured by an active period which suggests that nuclei formed throughout the solution. The formation of PRAGG's was detected after crystals became visible suggesting that after nucleation the depleted solution favored PRAGG formation. Finally, and most importantly for DCPCG, the work shows that nucleation was detected even if it was not quantitatively monitored and that PRAGG formation was detected prior to microscopic analysis.

D. Conclusions

1. Nucleation

At a particular temperature, particles with lower kinetic energy (KE), assuming a Maxwell-Boltzmann type distribution, are more easily influenced by the as yet unknown interactions which ultimately cause CRAGG formation. If there is a critical value KE_c, below which bonding to form a preCRAGG j-mer is favored, then as T is decreased, more particles have $KE < KE_c$ and the probability of achieving j_c is increased. As j_c is reached, nucleation is spontaneous and the CRAGG falls out of solution if it did not form on the side of the cuvette. Flashes encountered during nucleation are these sites forming in the scattering volume or crystals falling through the scattering volume.

If pH, concentration, and ionic strength are appropriate for crystallization but the temperature is kept too high for nucleation then the solute particles achieve a quasiequilibrium[36] size distribution which is qualitatively demonstrated by Fig. 42(a). As T is reduced and KE is taken away from the particles [monomers and possibly j-mers with j $O(10^1)$], a new quasiequilibrium distribution is established. This distribution includes those j-mers ($j < j_c$) formed by the low KE particles. This is demonstrated by the distributions proposed in Fig. 42. As the number of particles with $KE < KE_c$ increases then the probability of $j = j_c$ increases. The j_c-mer achieves nucleation, and its growth is too rapid for these PCS measurements. It is the status of the preCRAGG distribution that is actually measured in the CRAGG solutions.

To demonstrate that $j > j_c$ is not the major contributor to the CRAGG light scattering profile, contrast the isothermal CRAGG behavior of L5 and L6 to that of the PRAGG samples L1 and L2. The linear chain growth of PRAGG's allows nutrient particles access to only two binding sites per PRAGG and for case (3), proceeds slowly enough to monitor. The FS and d_{eff} measurements verify that the distribution evolves to large j. In L5 and L6 the increase towards large j was not seen, but visible crystals did form. There was no forward scattering at nucleation, there was no q dependence to D_{lin} or D_{2nd}, and only moderate intensity increases were recorded. It is then concluded that once j_c is reached, the growth is rapid and becomes more rapid as the number of binding sites increases with surface area. The CRAGG nucleates, grows, and falls out of solution in a time period comparable to the measurement duration (1 to 5 min) and is seen as a "dust like" flash by the instrument. A flash occurs when the nucleus forms in the scattering volume or when a crystallite falls through

FIG. 42. An illustration of the evolution of the preCRAGG distribution during CRAGG formation.

(a) The quasiequilibrium distribution is peaked at the monomer and probably contains some preCRAGG's ($j < 10$). The critical nucleus is not reached.

(b) At supersaturation the size distribution at quasiequilibrium is not static, and the preCRAGG's approach j_c.

(c) The preCRAGG's continue to approach j_c. If protein nucleation follows smaller, inorganic molecule nucleation principles the value of j_c depends on the degree of supersaturation.[80]

(d) The critical nucleus is reached. The CRAGG's grow to large sizes quickly and fall out of solution. Crystals become visible.

(e) The preCRAGG's and CRAGG's continue to form.

(f) As particles are removed from solution to the solid phase, the distribution relaxes.

(g) The distribution continues to relax.

(h) A new, relaxed quasiequilibrium is established among the preCRAGG's.

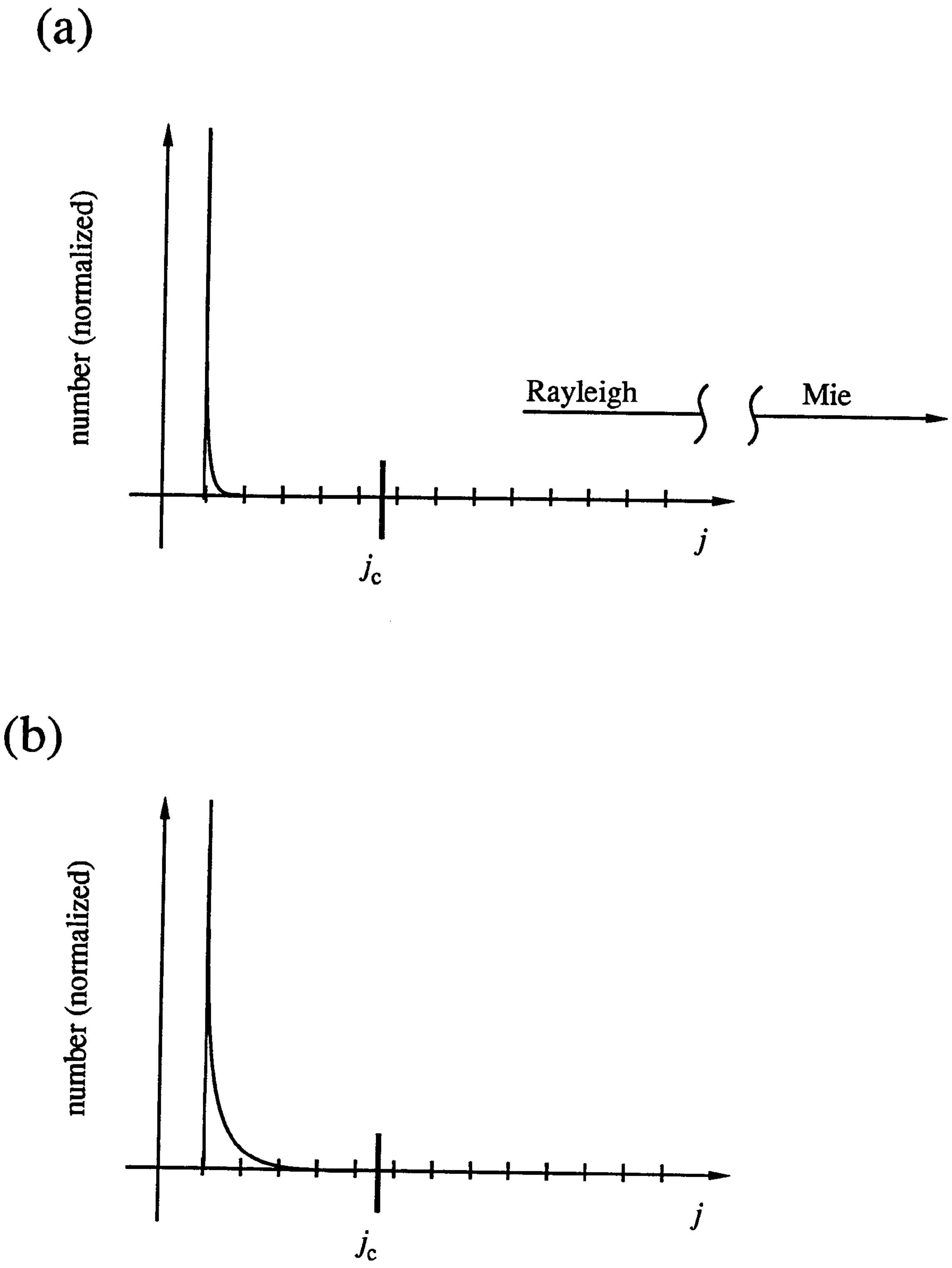
(a)
number (normalized)
Rayleigh
Mie
j_c
j
(b)
number (normalized)
j_c
j

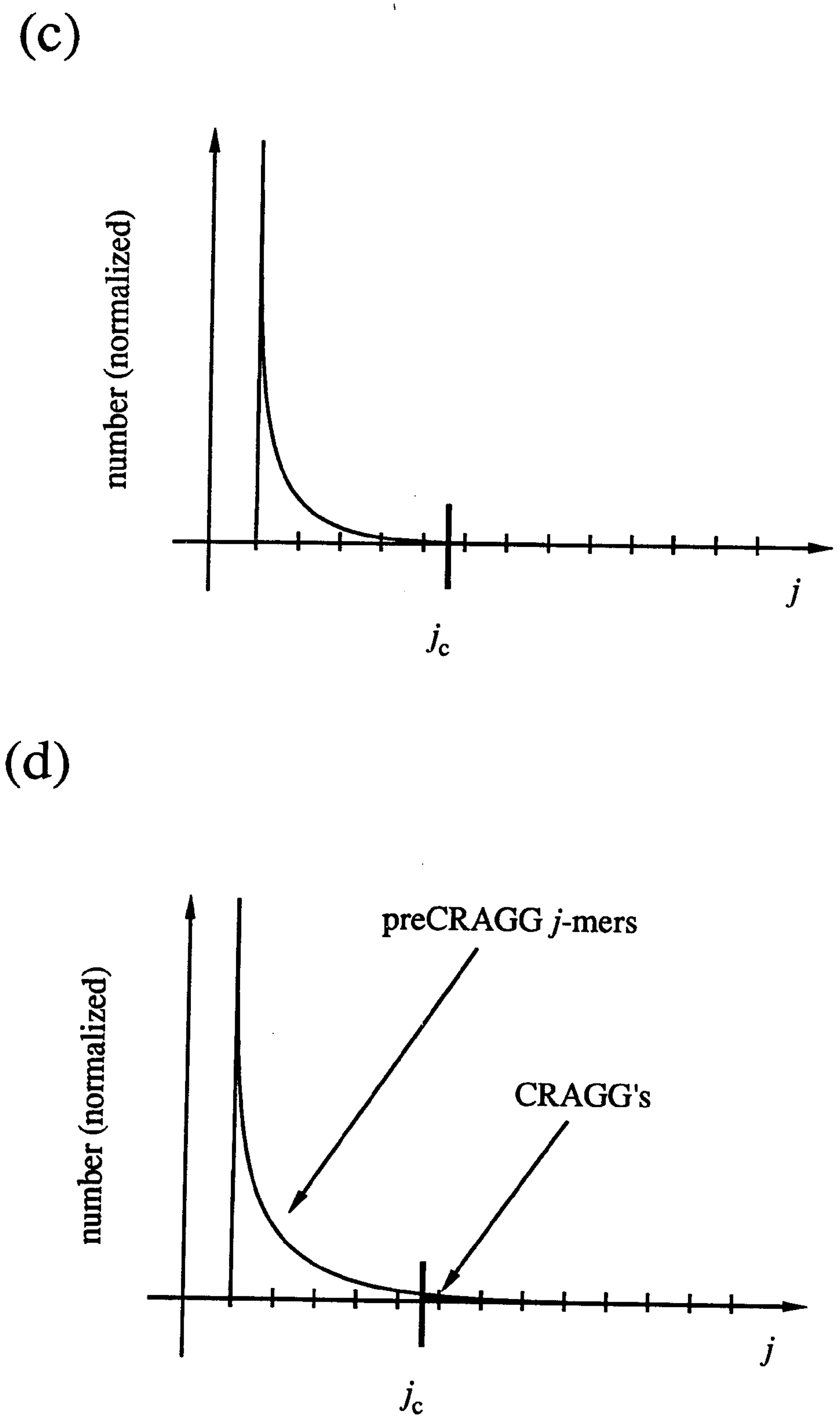
(c)
number (normalized)
j
j_c
(d)
preCRAGG j-mers
CRAGG's
number (normalized)
j
j_c

(e)

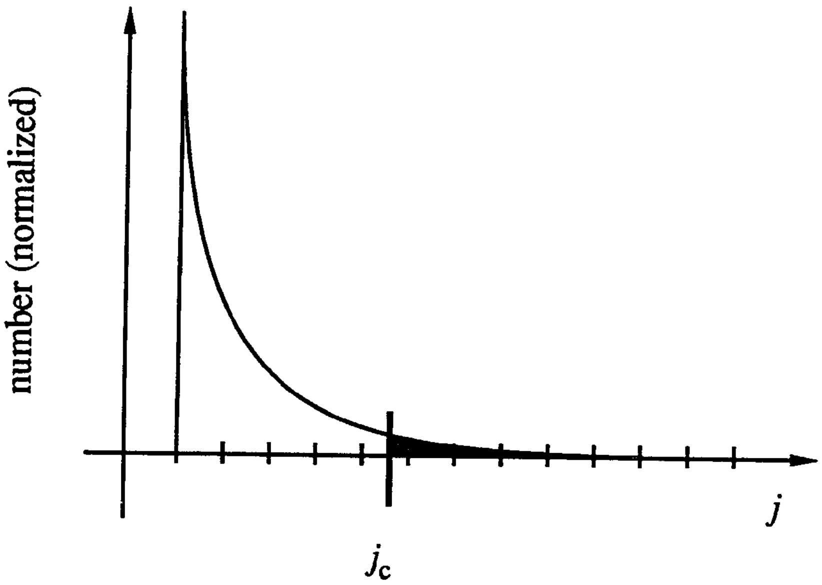

(f)

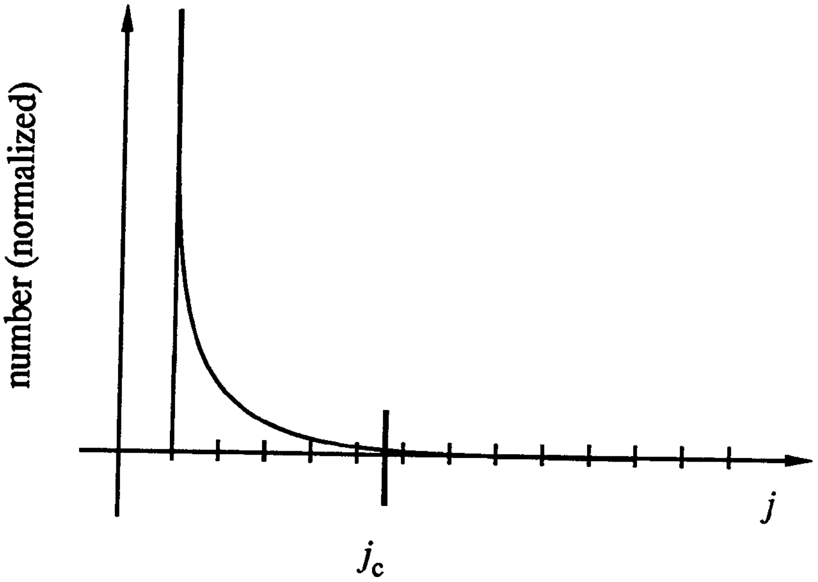

(g)

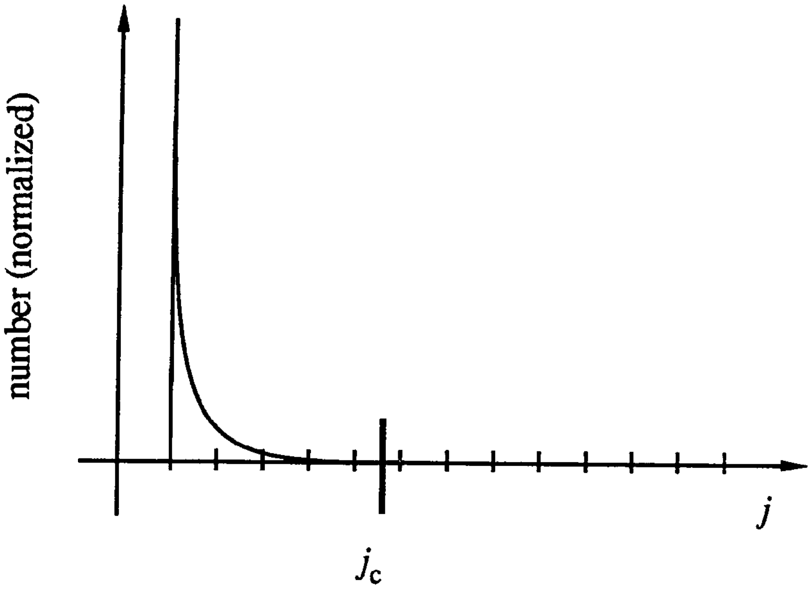

(h)

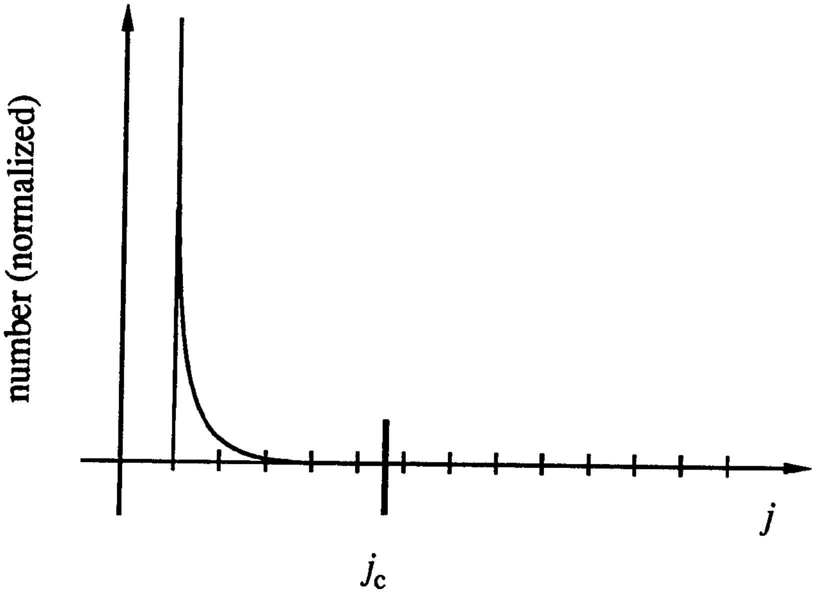

the scattering volume. A baseline is not attainable in this situation and the intensity measurement is rejected as dust, so no information on the actual CRAGG's is recorded. Therefore, the measurements that are available represent the contribution by the preCRAGG distribution and their interactions not the contribution of the CRAGG's themselves. These preCRAGG's are still virtually in the quasiequilibrium state, perhaps better stated as an accelerated quasiequilibrium state. If the particles are associating it is because $KE < KE_c$ and not because the volume term, as discussed by Kam and Feher, has overcome the surface term.

It will be difficult to unfold this distribution until more is known about lysozyme association and the consequences with regards to PCS measurements. For example, it has not yet been shown that in the presence of interactions the monomer with its hydration sphere is distinguishable by PCS from a dimer or even from a quadramer or that a quadramer is distinguishable from an octamer. Actually, it is not known if these *j*-mers are even stable, much less what their conformation, and hence physical size, in solution may be. Lack of this knowledge prevents detailed modeling of the distribution based on the data. However, if the overall frictional state of the system is taken to be the preCRAGG distribution and the interaction influence, then the best representation of the state is d_{eff} as calculated from single-τ D_{2nd}. The single-τ should be such that $0 < q^2\tau \leq 1 \times 10^7$ s/cm^2. Given the assumption that j_c is small, this d_{eff} represents the friction of the *j*-mers of interest. It is seen to give a consistent profile for all of the crystallization samples.

The frictional state of the system at quasiequilibrium depends on the degree of supersaturation and is demonstrated by the measurements as follows. Take d_{QE} to be the lowest value obtained for d_{eff} at each quasiequilibrium condition, and take $(c - c_{sol})/c_{sol}$ to be the measure of supersaturation. The solubility c_{sol} is given by the polynomials of Cacioppo.[18] The available data yield Fig. 43. A value near d_0 is obtained while undersaturated, but after saturation d_{QE} increases to more than twice d_0. This plot suggests that crystals would have formed in L4 at 25 or 20°C (points 3 and 4) if time had been allowed. However, when T was reduced to 15°C, $t_d \rightarrow 0$, and j_c was reached quickly by many aggregates.

For $t_d < t < t_{max}$ the state of the system changes in a way as to increase d_{eff}. An increase in intensity during this interval (see Figs. 22 and 24) strongly suggests an increase in particle size, but interactions were shown to influence the friction to a degree comparable to this increase. During nucleation at c = 47.0 mg/ml and T = 11°C, d_{max} was 7% greater than d_{init}. At low ionic strength, interactions were shown to cause a deviation of 10% from d_0 at c = 46.9 mg/ml and T = 11°C. Based on the interaction model of Anderson and Reed[3] hydrodynamic interactions were dominant even at this low ionic strength. Crystallization occurs at higher ionic strengths which further screen the Coulombic interactions. This suggests that hydrodynamic interactions are the critical interactions during nucleation, but the available data are not sufficient to separate the interaction effects from size distribution effects. An increase in intensity at nucleation as observed here has also been reported by Wilson.[99] This supports a conclusion that d_{eff} is primarily influenced by an actual association of molecules. However, the interactions that effect the association certainly affect the measure of d_{eff}.

Having concluded that the single-τ measurement of a crystallizing system detects the state of the preCRAGG distribution, it may be said that during nucleation the *j*-mers of this distribution steadily increase in size

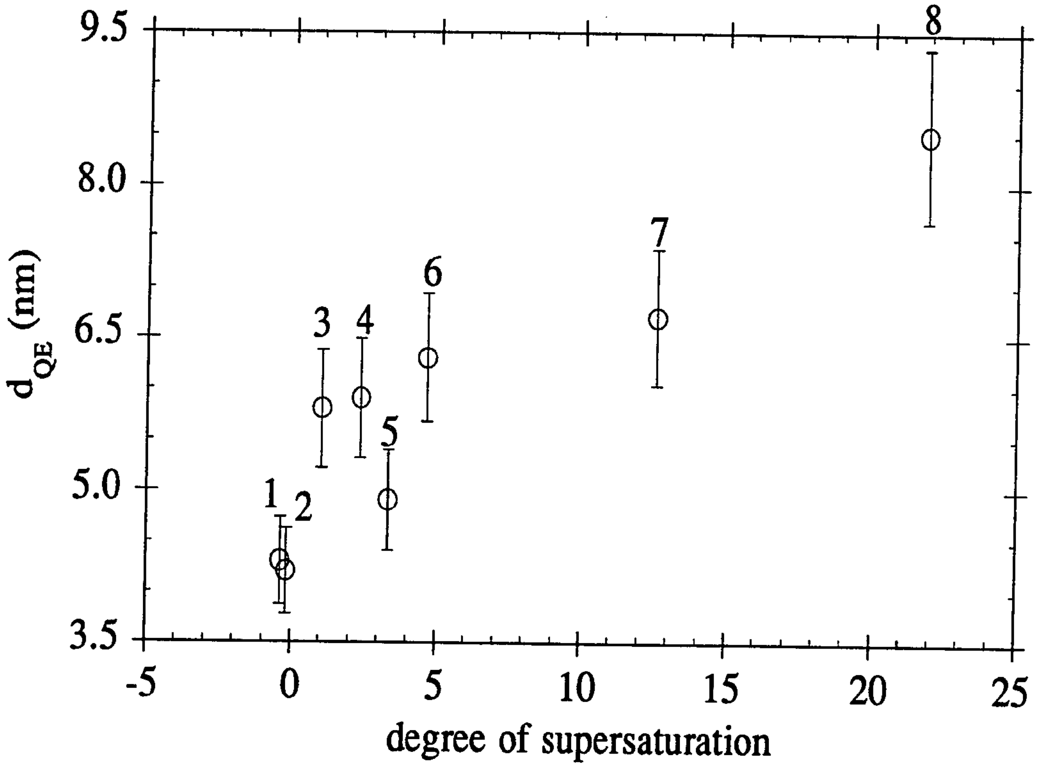

FIG. 43. The quasiequilibrium state is shown to be dependent on the degree of supersaturation, $(c - c_{sol})/c_{sol}$. Here, d_{QE} is the lowest value of d_{eff} at each quasiequilibrium condition: (1) L3(35°C), (2) L4(35°C), (3) L4(25°C), (4) L4(20°C), (5) L3(15°C), (6) L4(15°C), (7) L5(11°C), (8) L6(11°C). All errors were within the 10% limits shown.

and or number. This is the primary cause of the increase in d_{eff}. Critical nuclei form from the j_c-mers at the upper end of the distribution and grow quickly into visible crystals. For $t > t_{max}$ the decrease in d_{eff} was caused by a reduction in number and or size of the preCRAGG's as the nutrient is removed from the solution to the solid phase. The j-mer that is the actual nutrient or growth unit is still unknown. This reduction does not imply that a j-mer such as the unit cell is the growth unit. It is possible that monomers are the growth unit, and as the monomer concentration is reduced the quasiequilibrium state relaxes and larger preCRAGG's are no longer energetically favored. Hence, they break up into monomers to replenish the nutrient.

The asymptotic behavior represented by d_{final} is seen to be consistently higher than d_0. The concentration was measured in L5 and L6 after the sample was removed from the scattering chamber, and both were found to be supersaturated. Fig. 44 shows the values of d_{final} for comparison to d_{QE}. These points fit close to a linear regression if the supersaturated points of L4 (points 3, 4, and 6 of Fig. 43) are not included. This is not unreasonable due to the possibility of PRAGG formation in L4 concurrent with nucleation. As growth cessation is approached, the bulk solution is still in a state of quasiequilibrium. This quasiequilibrium state, however, is a stable state, not the accelerated state observed during nucleation.

Although unfavorable, the coexistence of PRAGG's and CRAGG's cannot be discounted. This is demonstrated by L4 and L6. Sample L4 showed some forward scattering and an anomalous multi-τ d_{eff}. PRAGG's may have formed due to impurities or to ineffective mixing. In L6, FS increased from 1 after crystals formed. Samples measured with the Wyatt

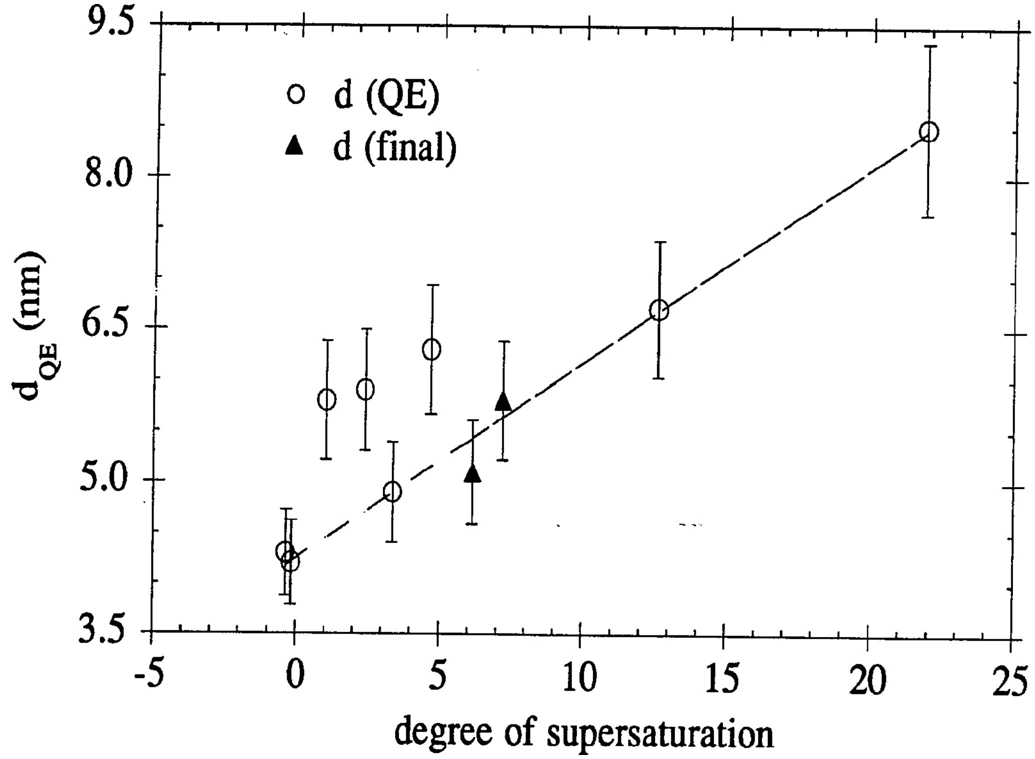

FIG. 44. The values of d_{final} for L5 and L6 are included for the data of Fig. 43. The linear regression shown does not include the three supersaturated points of L4. PRAGG's may have influenced those measurements. There is excellent agreement with the remaining data points.

device showed that PRAGG's were favored at low c and high ionic strength, so as c decreases during crystal growth, PRAGG's may have formed.

It is concluded that since interactions must play a part in nucleation they have some affect on d_{eff}. However, intensity measurements show that aggregation is a primary contributor and the Kam and Feher model cannot be disputed by this work. The j_c of the Kam and Feher model is small, probably $O(10^1)$; the size of the j_c-mer is well below the Mie regime at $\lambda_0 = 488$ nm. A CRAGG does not strongly influence the single-τ d_{eff} because when in the scattering volume it is seen as a flash which invalidates the measurement. These flashes were so numerous during insulin nucleation that it could not be followed with PCS, but with lysozyme the nucleation sites were fewer and were rarely observed in the scattering volume.

2. Monitoring

The most concrete conclusion that can be drawn from this work is that nucleation can be detected by light scattering before it would be possible by microscopy. Also, PRAGG's may be distinguished from CRAGG's at an early stage of the experiment. As shown by Thibault[94] and confirmed here, the presence of large (see Fig. 36) aggregates is not necessary for crystal formation. Although crystallization can occur in their presence, large aggregate formation is detrimental to the final product. Large aggregates are characterized by an increase in d_{eff} to more than twice d_{init} and by FS > 1.

As mentioned above, single-τ d_{eff} is the best indicator of the frictional state of the distribution of interest. The distribution is narrow about a small mean, so single-τ d_{eff} ($0 < q^2\tau \leq 1 \times 10^7$ s/cm^2) probes the proper fluctuations. A proper monitor could be achieved by a single-τ measurement at 2 or 3 angles. With a stable laser source the intensity could be followed, and FS could be calculated. It might be difficult for the DCPCG investigator to distinguish *in situ* a PRAGG increase in d_{eff} from a CRAGG increase until d_{max} is found, so an initial goal of DCPCG should be to crystallize while FS = 1.

3. Summary

Sample preparation was the most important step of the experimentation.

The model of Kam and Feher cannot be disputed by this work. All three cases were observed and Fig. 45 summarizes the best candidates for the general size distributions for each case.

Case (2) solutions precipitated too quickly to measure.

PRAGG behavior was determined from case (3) solutions.

PRAGG's form homogeneously throughout the solution and thus exhibit Mie scattering as their size increases.

PRAGG formation is undesirable for crystal growth and may be detected at an early stage by a measure of FS. (FS > 1 is undesirable.)

PRAGG formation occurred at low protein concentration and at high precipitant concentration or when a solution was improperly prepared.

CRAGG behavior was determined from case (1) solutions.

CRAGG's form heterogeneously within the solution and are not necessarily within the scattering volume.

During crystallization, the preCRAGG j-mer ($j < j_c$) distribution and the interactions between these j-mers are collectively observed by a single-τ d_{eff} measurement.

FIG. 45. A summary of the qualitative size distributions for the three cases of Kam and Feher.[36]

(a) This demonstrates the distribution of preCRAGG's that influences PCS measurements of the crystallizing sample, case (1). The preCRAGG's remain well within the Rayleigh regime.

(b) Case (2) PRAGG's aggregate too quickly to measure by light scattering and reach visible sizes.

(c) The aggregation of case (3) PRAGG's may be followed by light scattering. These PRAGG's enter the Mie scattering regime but do not become visible to a tabletop microscope at 10x.

(a) Case (1)

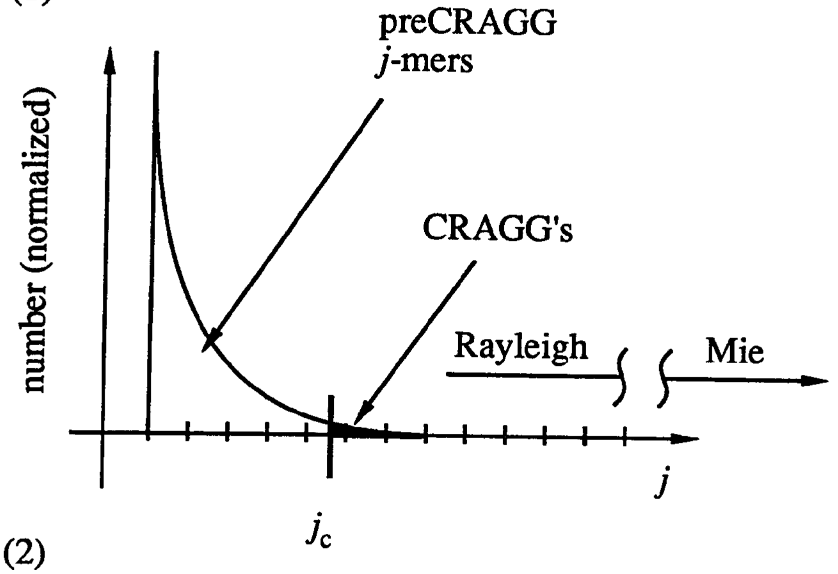

(b) Case (2)

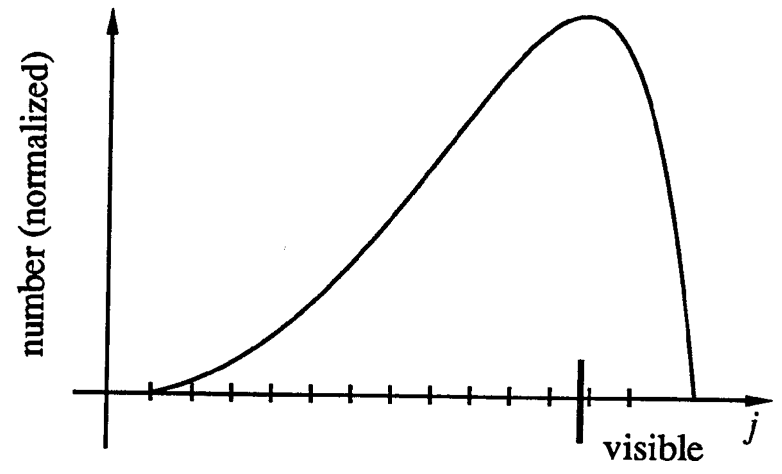

(c) Case (3)

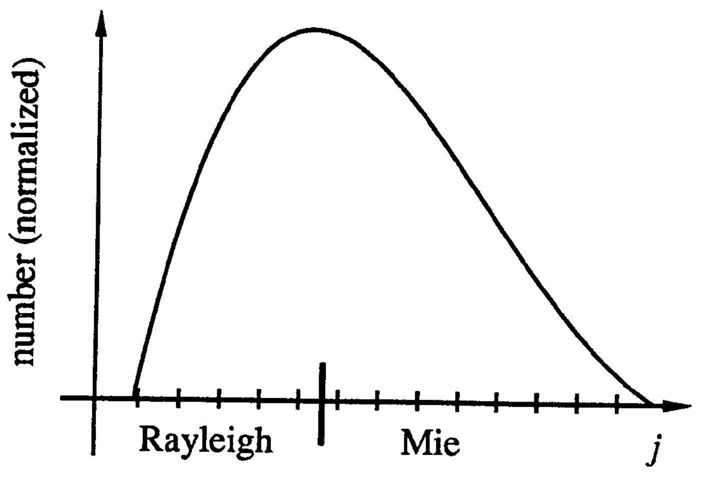

The distribution is narrow about a small mean (see Fig. 42) and the interactions with the greatest influence are hydrodynamic.

The quasiequilibrium state varies with the degree of supersaturation.

The insulin samples and L6 displayed PRAGG behavior after crystals appeared showing the necessity of controlling the growth conditions.

E. Recommendations and closing remarks

This research is of great benefit to DCPCG. It reveals what is actually being measured by PCS during crystallization and offers FS as a novel measurement for detecting the formation of undesirable PRAGG's. It offers little insight into the mechanisms of nucleation, however. Successful characterization of the nucleation of any protein is necessary to form a basis for the study of others. Such characterization will require a concerted effort on many fronts, so this first protein must be available in suitable quantities and easily crystallizable. Purity of the protein and consistency in sample preparation is of utmost importance for each branch of the research. The solubility of the protein must be known or determined for a wide range of pH and ionicity. Density and viscosity must also be determined over this range of parameters. Light scattering and chromatography should be performed on dilute solutions to determine free particle characteristics. Light scattering measurements should continue into the supersaturated regime to thoroughly investigate the quasiequilibrium state vs degree of supersaturation. Concentration measurements and light scattering measurements should be recorded during crystallization over a suitable range of conditions. Also, if DCPCG experiments proceed on all types of proteins, then data from monitoring during the growth should provide an excellent data base for comparison.

With the information available from all these branches of the effort, an analysis of the nucleation event might be possible.

Lysozyme is a good candidate for this study. The solubility is known over an acceptable range, and this work provides a suitable basis for light scattering studies. Results from density and viscosity studies will soon be published by UAH CMMR and data from DCPCG experiments at UAB CMC should also be available soon. The drawback with lysozyme is that the small size of the monomer puts it at the lower end of the resolution of PCS with conventional correlators. However, if light scattering studies should continue with lysozyme, Fig. 46 presents a suggestion for conditions which would allow use of the data within this thesis.

This thesis has confirmed that laser light scattering can be effectively used as a monitor of the nucleation of a relatively small protein. It has also shown that the presence of higher order aggregates in solution is not necessary for nucleation. Although the work utilizes the aggregation theory of Kam and Feher, it also shows that intermolecular interactions other than aggregation can effect a change in measured diffusion comparable to the changes observed during nucleation. Thus, it is not appropriate to assign changes in isothermal diffusion as being totally due to changes in the state of aggregation of the solute. However, intensity measurements show that aggregation is a primary contributor. These interactions surely effect the aggregation and should be of ultimate interest. They must be investigated carefully as outlined above before drawing conclusions on nucleation. This thesis provides a foundation on which to build such an investigation, and its limitations show the direction to take in the immediate future.

FIG. 46. Shown here are 42 conditions for each ionicity. The ionicity ranges from 0.8% to 2.0% NaCl in 0.2% steps for a total of seven ionicities. The 0.8% NaCl data of this thesis may be used. These conditions encompass varying degrees of both crystallizing and non-crystallizing solutions. The total number of samples is 294. Ionicity, lysozyme concentration, and temperature govern respectively, the Coulombic interaction potential, the intermolecular spacing, and the kinetic energy. Crystallization is expected at the higher lysozyme concentrations and lower temperatures at about 1.4% NaCl. Due to the long measurement periods needed to examine crystallizing solutions and the sheer number of measurements, some of the crystallization measurements may be eliminated, but investigation of the quasiequilibrium states preceding nucleation should be thoroughly investigated.

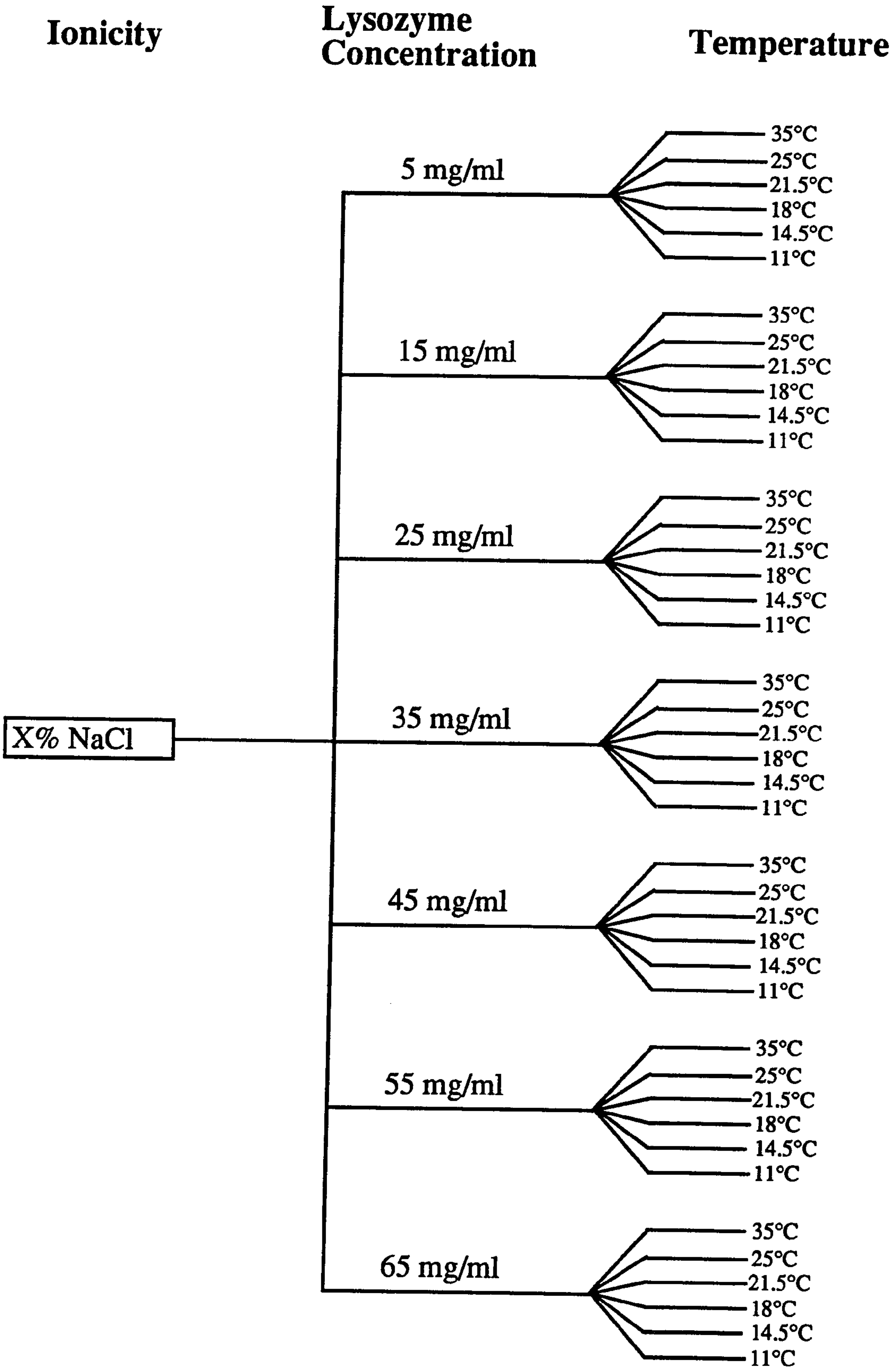
Ionicity
Lysozyme Concentration
Temperature
X% NaCl
5 mg/ml
15 mg/ml
25 mg/ml
35 mg/ml
45 mg/ml
55 mg/ml
65 mg/ml
35°C
25°C
21.5°C
18°C
14.5°C
11°C

REFERENCES

1. Adamson, A.W. (1967), Physical Chemistry of Surfaces 2nd ed. (Interscience Publishers, New York).
2. Altenberger, A.R. and Deutch, J.M. (1973), J. Chem. Phys. **59** (2), 894.
3. Anderson, J.L. and Reed, C.C. (1976), J. Chem. Phys. **64**, 3240.
4. Azuma, T., Tsukamoto, K., and Sunagawa, I. (1989), J. Cryst. Growth **98**, 371.
5. Baldwin, E.T., Crumbly, K.V., and Carter, C.W. (1986), Biophys. J. **49**, 47.
6. Bartunik, H.D., Clout, P.N., and Robrahn, B. (1981), J. Appl. Crystallogr. **14**, 134.
7. Bash, P.A., Pattabiraman, N., Huang, C., Ferrin, T.E., and Langridge, R. (1983), Science **222**, 1325.
8. Berne, B.J. and Pecora, R. (1976), Dynamic Light Scattering (Wiley-Interscience, New York).
9. Bernstein, F.C., Koetzle, T.F., Williams, G.J.B., Meyer, E.F. Jr., Brice, M.D., Rodgers, J.R., Kennard, O., Shimanouchi, T., and Tasumi, M. (1977), J. Mol. Biol. **112**, 535.
10. Bishop, J. B., Fredericks, W. J., Howard, S.B., and Sawada, T. (1991), The Fourth International Conference on the Crystallization of Biological Macromolecules, Aug. 18-24 Feiburg, Germany (Proceedings to be published, J. Cryst. Growth).
11. Bishop, J.B., Martin, J.C., and Rosenblum, W.M. (1991), J. Cryst. Growth **110**, 164.

12. Brice, J.C. (1985), Crystal Growth Processes (John Wiley and Sons, New York).

13. Brown, J.C., Pusey, P.N., Goodwin, J.W., and Ottewill, R.H. (1975), J. Phys. A **8** (5), 664.

14. Brown, R.G.W. (1987), Appl. Opt. **26** (22), 4846.

15. Bugg, C.E. (private communication).

16. Bugg, C.E. (1986), J. Cryst. Growth **76**, 535.

17. Burns, M.M., Fournier, J.M., and Golovchenko, J.A. (1990), Science **249**, 749.

18. Cacioppo, E. and Pusey, M.L.(1991), J. Cryst. Growth **114**, 286.

19. Chu, B. (1974), Laser Light Scattering, (Academic Press, New York).

20. Cook, W.J., Ealick, S.F., Bugg, C.E., Stoeckler, J.D., Parks, R.E. Jr. (1981), J. Biol. Chem. **256**, 4079.

21. Craik, C.S., Largman, C., Fletcher, T., Roczniak, S., Barr, P.J., Fletterick, R., and Rutter, W.J. (1985), Science **228**, 291.

22. Cummings, P.G. and Staples, E.J. (1987), Langmuir **3** (6), 1109.

23. Dalberg, P.S., Boe A., Strand, K.A., and Sikkeland, T. (1978), J. Chem. Phys. **69** (12), 5473.

24. DeLucas, L.J. (private communication).

25. DeLucas, L.J. and Bugg, C.E. (1987), TIBTECH **5**, 188.

26. DeLucas, L.J., Suddath, F.L., Snyder, R., Naumann, R., Broom, M.B., Pusey, M., Yost, V., Herren, B., Carter, D., Nelson, B., Meehan, E.J., Mcpherson, A., and Bugg, C.E. (1986), J. Cryst. Growth **76**, 681.

27. Dhadwal, H.S., Wu, C., and Chu, B. (1989), Appl. Opt. **28** (19), 4199.

28. Drake R.M. and Gordon, J.E. (1985), Am. J. Phys. **53** (10), 955.

29. Dubin, S.B., Clark, N.A., and Benedek, G.B. (1971), J. Chem. Phys. **54** (12), 5158.

30. Ealick, S.F., Greenhough, T.J., Babu, Y.S., Carter, D.C., Cook, W.J., Bugg, C.E., Rule, S.A., Habash, J., Helliwell, J.R., Stoeckler, J.D., Chen, S.-F., Parks, R.E. Jr. (1985), Ann. N.Y. Acad. Sci. **451**, 311.

31. Ealick, S.F., Rule, S.A., Carter, D.C., Greenhough, T.J., Babu, Y.S., Cook, W.J., Habash, J., Helliwell, J.R., Stoeckler, J.D., Parks, R.E. Jr., Bugg, C.E. (1990), J. Biol. Chem. **265**, 1812.

32. Einstein, A. (1905), Ann. Phys. **17**, 549.

33. Einstein, A. (1956), Investigations on the Theory of the Brownian Movement (Dover, New York).

34. Espenson, J.H. (1981), Chemical Kinetics and Reaction Mechanisms (McGraw Hill, New York).

35. Estell, D.A., Graycar, T.P., and Wells, J.A. (1985), J. Biol. Chem. **260**, 6518.

36. Feher, G. and Kam, Z. (1985), in Methods in Enzymology edited by Wycoff, H. W., Hirs, C. H. W., and Timisheff, S. N. (Academic Press, New York), **114**, 77.

37. Fersht, A.R., Shi, J.-P., Knill-Jones, J., Lowe, D.M., Wilkinson, A.J., Blow, D.M., Brick, P., Carter, P., Waye, M.M.Y., and Winter, G. (1985), Nature **314**, 235.

38. Galloway, J. (1985), Nature **314**, 228.

39. Giordano, R., Salleo, A., Salleo, S., Mallamace, F., and Wanderlingh, F. (1980), Opt. Acta **27** (10), 1465.

40. Goodman, C.H.L., editor (1974), Crystal Growth: Theory and Techniques Vol. 1 (Plenum Press, London and New York).

41. Goodman, C.H.L., editor (1978), Crystal Growth: Theory and Techniques Vol. 2 (Plenum Press, London and New York).

42. Greenhough, T.J. and Helliwell (1983), Prog. Biophys. Mol. Biol. **41**, 67.

43. Gruner, F. and Lehmann, W. (1979), J. Phys. A **12** (11), L303.

44. Gulari, E., Gulari, E., Tsunashima, Y., and Chu, B. (1978), J. Chem. Phys. **70** (8), 3965.

45. Hamlin, R., Cork, C., Howard, A., Nielson, C., Vernon, W., Matthews, D., Xuong, N.G.H., and Perez-Mendiz, V. (1981), J. Appl. Crystallogr. **14**, 85.

46. Harrison, S.C.(1984), Nature **309**, 408.

47. Herzberg, O. and Sussman, J.L. (1983), J. Appl. Crystallogr. **16**, 144.

48. Jones, A. (1978), J. Appl. Crystallogr. **11**, 268.

49. Kadima, W., McPherson, A., Dunn, M.F., Jurnak, F.A. (1990), Biophys. J. **57**, 125.

50. Kaiser, E.T. and Lawrence, D.S. (1984), Science **226**, 505.

51. Kam, Z., Shore, H.B., and Feher, G. (1978), J. Mol. Biol. **123**, 539.

52. Kerker, M. (1969), The Scattering of Light and Other Electromagnetic Radiation (Academic Press, New York).

53.. Kitagawa, Y., Hayashi, A., and Minami, S. (1988), Appl. Opt. **27** (15), 3068.

54. Konnert, J.H. and Hendrickson, W.A. (1980), Acta Crystallogr. Sec. A **36**, 344.

55. Koppel, D.E. (1972), J. Chem. Phys. **57** (11), 4814.

56. Krayenbuhl, C. and Rosenberg, T. (1946), Reports of the Steno Memorial Hospital and the Nordisk Insulinlaboratorium **1**, 60.

57. Laidler, K.J. (1987), Chemical Kinetics 3rd ed. (McGraw Hill, New York).

58. Leslie, A.G.W. (1984), Acta Crystallogr. Sec. A **40**, 451.

59. Littke, W. and John, C. (1984), Science **225**, 203.

60. Long, M. (private communication), Protein Crystallization Facility, patent pending.

61. McPherson, A. (1982), Preparation and Analysis of Protein Crystals (John Wiley and Sons, New York).

62. Mie, G. (1908), Ann. Physik **25**, 377.

63. Mikol, V., Hirsch, E., and Giege', R. (1989), FEBS Letters **258** (1), 63.

64. Mikol, V., Hirsch, E., and Giege', R. (1990), J. Mol. Biol. **213**, 187.

65. Moffat, K., Szebenyi, D., and Bilderback, D. (1984), Science **223**, 1423.

66. Morffew, A.J., Moss, D.S., (1983), Acta Crystallogr. Sec. A **39**, 196.

67. Morrison, I.D., Grabowski, E.F., and Herb, C.A. (1985), Langmuir **1** (4), 496.

68. Nambiar, K.P., Stackhouse, J., Stauffer, D.M., Kennedy, W.D., Eldredge, J.K., and Benner, S.A. (1984), Science **223**, 1299.

69. Ostrowsky, N., Sornette, D., Parker, P., and Pike, E.R. (1981), Opt. Acta **28** (8), 1059.

70. Ostwald, W. (1897), Z. Physik. Chem. **22**, 302.

71. Oxender, D.L. and Fox, C.F., editors (1987), Protein Engineering (Alan R, Liss Inc., New York)

72. Perry, L.J. and Wetzel, R. (1984), Science **226**, 555.

73. Phillies, G.D.J. (1975), J. Chem. Phys. **62** (10), 3925.

74. Phillies, G.D.J., Benedek, G.B., and Mazer, N.A. (1976), J. Chem. Phys. **65** (5), 1883.

75. Provencher, S.W. (1976), J. Chem. Phys. **64** (7), 2772.

76. Pusey, M.L. and Munson, S. (1991), J. Cryst. Growth **113**, 385.

77. Pusey, P.N. (1978), J. Phys. A **11** (1), 119.

78. Pusey, P.N. and Tough, R.J.A. (1985), in Dynamic Light Scattering Applications of Photon Correlation Spectroscopy edited by Peccora, R. (Plenum Press, New York) 85.

79. Rayleigh, Lord J.W.S. (1871), Philos. Mag. **41**, 107, 274, 477.

80. Rosenberger, F. (1979), Fundamentals of Crystal Growth I (Springer-Verlag, Berlin and New York).

81. Rosenberger, F., Howard, S., Nyce, T., and Sowers, J. (to be submitted to J. Cryst. Growth, 1992).

82. Rosenberger, F. and Meehan, E.J. (1988), J. Cryst. Growth **90**, 74.

83. Roxby, R. and Tanford, C. (1971), Biochemistry **10** (18), 3348.

84. Salemme, F.R. (1972), Arch. Biochem. Biophys. **151**, 533.

85. Salemme, F.R. (1985), in Methods in Enzymology edited by Wycoff, H. W., Hirs, C. H. W., and Timisheff, S. N. (Academic Press, New York), **114**, 140.

86. Schaefer, D.W. and Berne, B.J. (1974), Phys. Rev. Lett. **32** (20), 1110.

87. Schatzel, K. (1987), Appl. Phys. B **42**, 193.

88. Siegert, A.J.F. (1943), MIT Rad. Lab., Report No. 465.

89. Snyder, R., Bugg, C.E., DeLucas, L.J., Rosenberger, F., Suddath, F.L., and Ward, K., (1989), NASA working group: Advanced Protein Crystal Growth, Atlanta, Ga., Nov. 12-13.

90. Sophianopoulos, A.J., Rhodes, C.K., Holcomb, D.N., and Van Holde, K.E. (1962), J. Biol. Chem. **237** (4), 1107.

91. Sophianopoulos, A.J. and Van Holde, K.E. (1964), J. Biol. Chem. **239** (8), 2516.

92. Stock, R.S. and Ray, W.H. (1985), J. Polym. Sci., Polym. Phys. Ed. **23**, 1393.

93. Sussman, J.L. and Podjarny, A.D. (1983), Acta Crystallogr. Sec. B **39**, 495.

94. Thibault, F., Langowski, J., and Leberman, R. (1991), The Fourth International Conference on the Crystallization of Biological Macromolecules, Aug. 18-24 Feiburg, Germany (Proceedings to be published, J. Cryst. Growth).

95. Usha, R., Johnson, J.E., Moras, D., Thierry, J.C., Fourme, R., and Kahn, R. (1984), J. Appl. Crystallogr. **17**, 147.

96. Wharton, R.P. and Ptashne, M. (1985), Nature **316**, 601.

97. Wilson, L.J. (1991), The Fourth International Conference on the Crystallization of Biological Macromolecules, Aug. 18-24 Feiburg, Germany (Proceedings to be published, J. Cryst. Growth).

98. Wilson, L.J., Bray, T.L., and Suddath, F.L. (1991), J. Cryst. Growth **110**, 142.

99. Wilson, W. W. (1991), The Fourth International Conference on the Crystallization of Biological Macromolecules, Aug. 18-24 Feiburg, Germany (Proceedings to be published, J. Cryst. Growth).

100. Wilson, W.W. (1990), Methods: A Companion to Methods in Enzymology **1** (1), 110.

101. Zeppezauer, M., Eklund, H., and Zeppezauer, E. (1968) Arch. Biochem. Biophys. 126, 564.

102. Zimm, B.H. (1948), J. Chem. Phys. **16**, 1093.

GRADUATE SCHOOL
UNIVERSITY OF ALABAMA AT BIRMINGHAM
DISSERTATION APPROVAL FORM

Name of Candidate John Bradford Bishop

Major Subject Physics

Title of Dissertation An Investigation of Protein Crystal Growth by Laser Light Scattering

Dissertation Committee:

William Rosenblum	, Chairman	William M Rosenblum
Mike Lewis		Mike Lewis
Jim Martin		James L Martin
Jimmy Mays		
Thomas Nordlund		T M Nordlund

Director of Graduate Program

Dean, UAB Graduate School W. A. Sibley

Date 6/17/92